

**Porous Nanocrystalline Silicon Membranes as Sieves and
Pumps**

by

Jessica L. Snyder

Submitted in Partial Fulfillment
of the
Requirements for the Degree
Doctor of Philosophy

Supervised by

Professor James L. McGrath

Department of Biochemistry and Biophysics
School of Medicine and Dentistry

University of Rochester
Rochester, NY

2011

Curriculum Vitae

The author was born in Malone, NY on June 14th, 1984. She attended Clarkson University from 2001 to 2005, and graduated with a Bachelor of Science degree in Biology. She came to the University of Rochester in the Fall of 2005 and began graduate studies in Biophysics. She was awarded the Robert L. and Mary L. Sproull Fellowship and the Merritt and Marjorie Cleveland Fellowship upon acceptance to the program. She pursued research in membrane technology under the direction of Professor James L. McGrath and received a Master of Science degree from the University of Rochester in 2008. In 2010 she was awarded an Elon Huntington Hooker Fellowship and the William F. Neuman Award to support her predoctoral research.

List of Publications

- J.L. Snyder, D.Z. Fang, T.R. Gaborski, C.C. Striemer, P.M. Fauchet, J.L. McGrath, High performance, low voltage electroosmotic pumps with molecularly thin nanoporous membranes, *Proc. Natl. Acad. Sci.* Submitted.
- J.L. Snyder, A. Clark Jr., D.Z. Fang, T.R. Gaborski, C.C. Striemer, P.M. Fauchet, and J.L. McGrath, An experimental and theoretical analysis of molecular separations by diffusion through ultrathin nanoporous membranes, *J. Mem. Sci.* **369**, 119-129 (2011).
- T.R. Gaborski, J.L. Snyder, C.C. Striemer, D.Z. Fang, M. Hoffman, P.M. Fauchet, J.L. McGrath, High performance separation of nanoparticles with ultrathin porous nanocrystalline silicon membranes, *ACS Nano* **4**, 6973-6981 (2010).
- B.S. Tolbert, S.G. Tajc, H. Webb, J.L. Snyder, J.E. Nielsen, B.L. Miller, R. Basavappa, The active site cystein of ubiquitin-conjugating enzymes has a significantly elevated pKa: functional implications, *Biochemistry* **44**, 16385-16391 (2005).

Acknowledgments

As my research was not performed in a vacuum, any success can be attributed to an entire community of people. My advisor, Professor James McGrath, was instrumental in all aspects of this project, through provisions of guidance and troubleshooting problems associated with the course of this research. Our collaboration with Professor Philippe Fauchet's laboratory gave rise to the Nanomembrane Research Group (NRG, nanomembranes.org) and the startup SiMPore Inc. The numerous members of the NRG and SiMPore have all provided insightful discussions and unique ideas that have helped me with my work. In particular, without Dr. Thomas Gaborski, Dr. Christopher Striemer, and Dr. David Fang, this work would not have been possible. In several of the specific projects in this work, I had the fortune to receive assistance from Professor Alfred Clark Jr., Michael Hoffman, Paul Black, and Professor William Bernhard.

My thesis committee, Professors Philippe Fauchet, William Bernhard, David Mathews, and Benjamin Miller, have provided helpful and focusing discussions throughout the process. The staff from the Biochemistry and Biophysics Department and the Biomedical Engineering Department have all helped by smoothing out the small and large details of graduate research. Funding for this research came from the National Institutes of Health, the National Science Foundation, New York State, the Clinical and Translational Science Institute, and the Johnson & Johnson Discovery Grant. Finally, this work would not have been possible without the support of my family and Graham Marsh.

Abstract

Porous nanocrystalline silicon (pnc-Si) is a novel nanoporous material that is fabricated into 7-30 nm thick freestanding membranes. Pores self assemble during the fabrication process, and pore distributions can be tuned between 5 and 100 nm, which is within the size range of small molecules and proteins. Conventional polymeric membranes are 2-3 orders of magnitude thicker than pnc-Si membranes and lack well defined pores. Because of their nanoscale architecture, pnc-Si membranes display unique characteristics when used as sieves for molecular separations and porous media for electroosmosis. In this work, pnc-Si membranes have been investigated in these applications and compared to conventional membrane materials.

Experiments show that pnc-Si membranes enable sharp and rapid separations of molecules by diffusion. The tight pore distributions allow for precise fractionation of complex mixtures of small molecules and proteins. Diffusion across the membrane proceeds quickly, as the thickness of the membrane is on the same scale as the diameter of the molecules. Molecule diameters that are 30% or less of the maximum pore diameter encounter little hindrance and diffuse as if no membrane were present. Theoretical predictions using pore distribution data corroborate these results. Molecules close in size to the maximum pore size are hindered more than theory predicts, and this may be a result of molecular adsorption that shrinks the effective pore size. Additionally, theoretical simulations indicate that the hindrance imparted by the pores in thicker conventional membranes is magnified by the long diffusion times through the pores, thereby reducing

the resolution of separations and requiring longer times to reach equilibrium.

The innate negative charge of the pnc-Si membrane also plays a role in separations. Experimental separations performed at low salt concentrations (<100 mM) significantly differed from those at higher salt concentrations. At lower salt concentrations, the ionic shielding of the negative membrane surface potential is reduced and diffusion is influenced by charge interactions between the membrane and the species being tested. Electrostatic effects scale with the Debye length, a measure of the thickness of the diffuse layer of counterions near the pore walls. Results show that negatively charged double-stranded DNA is strongly hindered from diffusing through the pores at low salt concentrations. The diffusion of proteins at pH above their isoelectric point and negatively charged nanoparticles is also reduced at low salt concentrations.

Ultrathin pnc-Si membranes are expected to present less resistance to fluid flow as compared to micron thick conventional membranes. Experiments supported this hypothesis, and pnc-Si membranes displayed water flow rates that were 2-3 orders of magnitude higher than conventional thick membranes and at least 1 order of magnitude higher than other nanoengineered membranes found in the literature. Theoretical predictions of water flow were performed using pore distribution data. The theoretical and experimental flow rates were found to be in good agreement. The tight pore distributions enabled separation cutoffs between proteins with a difference of 2 nm in diameter and gold nanoparticles with a difference of 5 nm in diameter.

Finally, pnc-Si membranes were found to have normalized electroosmosis rates of $2.6 \times 10^2 \text{ mL min}^{-1} \text{ cm}^{-2} \text{ V}^{-1}$, which are 2-3 orders of magnitude higher than other DC electroosmotic pumps in the literature. The high flow rates are attributed to the fact that high electric fields form across the ultrathin membranes even with low applied voltages. Agreement is shown between electroosmotic flow rates and theory developed for long pores, indicating that there is minimal contribution to the fluid flow from entrance and exit effects in the ultrathin membrane. Pnc-Si membranes add little electrical resistance to the system and the transmembrane voltage drop is on the order

of 10 mV. With optimization, pnc-Si membranes could function as the first low voltage, on-chip electroosmotic pumps for microfluidic devices.

Contents

Foreword	1
1 Background	3
1.1 Current membrane technology	3
1.2 Porous nanocrystalline silicon	8
1.3 Benefits of ultrathin membranes	12
1.4 Diffusion-based separations	13
1.5 Hindrance theory	16
1.6 Charge-based separations	19
1.7 Pressurized separations and fluid flow	21
1.8 Electroosmosis	23
1.9 Thesis Organization	26
1.10 References	27
2 Diffusion Separations	35
2.1 Abstract	35
2.2 Introduction	36
2.3 Experimental	39
2.3.1 Pnc-Si Membrane Fabrication and Characterization	39
2.3.2 Protein and Small Molecule Separations	40
2.4 Theory	42

2.4.1	1-D Analytical Model	42
2.4.2	Defining Membrane Resistance	45
2.4.3	3-D Computational Model	47
2.5	Results and Discussion	48
2.5.1	Protein and Small Molecule Separations	48
2.5.2	Resistance Components	50
2.5.3	Visualizing Membrane Resistance	51
2.5.4	Sieving by Thin and Thick Membranes	53
2.5.5	Factors that Influence Membrane Separations	55
2.5.6	Comparison to Experiments	58
2.6	Conclusions	63
2.7	Appendix A	64
2.8	Appendix B	65
2.9	Supplement	66
2.9.1	Resistances	66
2.9.2	Concentration	67
2.9.3	Osmosis	70
2.9.4	Gravitational Flow	71
2.9.5	Molecule Sizes	71
2.10	References	72
3	Charge-Based Separations	78
3.1	Abstract	78
3.2	Introduction	79
3.3	Methods	82
3.3.1	Pnc-Si membranes	82
3.3.2	Protein Separations	82
3.3.3	DNA Separations	83

3.3.4	Nanoparticle Separations	84
3.4	Experimental Results	85
3.4.1	Protein Separations	85
3.4.2	DNA Separations	85
3.4.3	Dynamics of DNA Diffusion	87
3.4.4	Nanoparticle Separations	89
3.5	Theoretical Comparison	91
3.6	Conclusions and Future Direction	97
3.7	References	99
4	Pressurized Separations	103
4.1	Abstract	103
4.2	Introduction	104
4.3	Results and Discussion	106
4.4	Methods	115
4.4.1	Hydraulic Permeability of Pnc-Si.	115
4.4.2	Hydraulic Permeability of Track-Etched Membranes.	117
4.4.3	Membrane Production.	117
4.4.4	Electron Microscopy.	118
4.4.5	Pore Image Processing and UV/Ozone Treatments.	118
4.4.6	Gold Nanoparticle Filtration.	118
4.4.7	Protein Separations.	119
4.5	Supplemental Methods and Figures	121
4.5.1	Analysis of hydraulic permeability in the wet/wet configuration	121
4.5.2	Estimate of uncertainty in predicted hydraulic permeability	122
4.6	References	127
5	Electroosmosis	133
5.1	Abstract	133

5.2	Introduction	134
5.3	Results and Discussion	135
5.3.1	Electroosmosis Flow Rates	135
5.3.2	Theoretical Comparison	136
5.3.3	Surface modifications	141
5.3.4	Comparison to other EOPs	142
5.4	Conclusions	145
5.5	Methods	146
5.5.1	Pnc-Si Fabrication	146
5.5.2	Testing Devices	146
5.5.3	Plasma Oxidation and Aminosilanization	148
5.6	References	148
6	Concluding Remarks	153
6.1	Diffusion separations and sieving model	153
6.1.1	Summary of findings	153
6.1.2	Future direction	155
6.2	Charge-based separations and electrostatics model	155
6.2.1	Summary of findings	155
6.2.2	Future direction	156
6.3	Water permeability and pressurized separations	156
6.3.1	Summary of findings	156
6.3.2	Future direction	157
6.4	Pnc-Si membranes as electroosmotic pumps	158
6.4.1	Summary of findings	158
6.4.2	Future direction	158
6.5	References	160

List of Figures

1.1	Current membrane technology	6
1.2	Images and schematic of pnc-Si membranes	9
1.3	Comparison of molecular, particle, and cellular sizes to pnc-Si pores . .	10
1.4	Experimental and theoretical comparison of thin membrane permeability	16
1.5	Early electroosmosis experiment with pnc-Si	24
2.1	Pnc-Si membrane	39
2.2	Experimental setup and 3-D computational diffusion model.	41
2.3	Experimental results of protein and small molecule separations	49
2.4	Components of resistance for thin and thick membranes with 15 nm pores and comparison to fluid well resistance.	50
2.5	Concentration profiles in 1-D model.	52
2.6	Sieving profiles of 5 nm thick and 5 μ m thick membranes for 1, 6, and 24 hour time points.	54
2.7	Factors that influence separations by ultrathin membranes.	56
2.8	Slice through 3-D model after 10 hours of diffusion of a 5 nm radius molecule.	59
2.9	Experimental and 3-D model sieving profiles for pnc-Si separations. . . .	60
2.10	Membrane resistance to diffusion	68
3.1	Pnc-Si membranes for charge-based separations	81

3.2	Charge-based protein separations	86
3.3	Charge-based DNA diffusion through pnc-Si membranes	87
3.4	Relative times for DNA rotation and translation	90
3.5	3-D CAD model with mesh visualization	92
3.6	Experimental and theoretical separations with nanoparticles	96
4.1	Pnc-Si membranes and experimental setup	106
4.2	Experimental and theoretical water permeability	108
4.3	Pnc-Si membranes are impermeable in wet-dry configurations	110
4.4	UV ozone treatment increases membrane hydrophilicity	120
4.5	Pore processing of TEM images	123
4.6	UV ozone treatment increases membrane hydrophilicity	124
4.7	Flow sharpens the effective pore distribution	125
4.8	Pnc-Si membrane fabrication is highly scalable	126
4.9	Hydraulic permeability of pnc-Si is time-independent	127
5.1	Pnc-Si membranes and testing devices	137
5.2	Electroosmotic flow	140
5.3	Pnc-Si electrical resistance	142
5.4	Flow rate comparison between EOPs	144
5.5	Streaming potential measurements	147

List of Tables

1.1	Debye lengths of symmetric salt solutions	19
2.1	Total number of molecules in the separation mixture	68
2.2	Critical concentrations of proteins as predicted by Graessley equation	69
2.3	Hydrodynamic and crystallographic radii of molecules	72
3.1	Physical characteristics of proteins	85
3.2	Separations with nanoparticles	91
4.1	Physical dimensions of protein in the size ladder	111
4.2	Stock nanoparticle sizes as determined by DLS and TEM	112

Notation

A_a	cross sectional area of annulus	k_t	trapping rate
A_c	cross sectional area of capillary	L	pore length
A_{cup}	centrifuge tube cross section	L_p	hydraulic permeability
A_{Im}	processed image area	N	number density
A_m	active membrane area	N_A	Avogadro's number
a	fluid well length	P	permeability
c	concentration	ΔP	applied pressure
D	diffusion coefficient	P_d	pore discovery permeability
D_0	free diffusion coefficient	P_t	transmembrane permeability
D_m	membrane diffusion coefficient	Pe	Péclet number
D_{rot}	rotational diffusion	Q	volumetric flow rate
D_{trans}	translational diffusion	q	charge
d	membrane thickness	R	gas constant
\mathbb{E}	energy	R_b	bulk electrical resistance
E	electric field strength	R_c	silicon chip electrical resistance
F	Faraday's constant	R_g	radius of gyration
ΔG	normalized free energy	R_h	hydrodynamic radius
g	gravitational acceleration	R_m	membrane electrical resistance
h	height of water column	R_p	pore radius
I	current	R_s	radius of diffusing species
J	flux	r	radius
J_f	flux entering or leaving fluid wells	S	sieving coefficient
J_m	flux within the membrane	T	temperature
J_v	volume flux	t	time
K	enhanced drag	U	fluid velocity
K_d	hindrance factor	V_{app}	applied voltage
k	conductivity	V_{cup}	fluid volume in centrifuge tube
k_b	Boltzmann's constant	V_{TM}	transmembrane voltage
k_p	permeability	x	position

Greek Letters

β	resistance parameter
ϵ	dielectric permittivity
ζ	zeta potential
κ^{-1}	Debye length
λ	R_s/R_p ratio
λ_n	eigenvalue
μ	viscosity
$\Delta\Pi$	osmotic pressure
ρ	radial integration variable
ρ_w	density of water
σ_0	osmotic reflection coefficient
σ_p	surface charge density of pore
σ_s	surface charge density of species
τ	R_p/κ^{-1}
τ_{eq}	equilibrium time constant
Φ_s	streaming potential
ϕ	partition coefficient
χ_d	disk surface fraction
χ	porosity
ψ_n	eigenfunction
ψ_p	surface potential of pore
ψ_s	surface potential of species
Ω	resistance
Ω_m	membrane resistance
Ω_w	well resistance

Foreword

This work was a collaborative effort between the Nanomembrane Research Group (McGrath and Fauchet laboratories) and SiMPore, Inc. Dr. Christopher Striemer was the original inventor of porous nanocrystalline silicon, and was integral in the development of materials for this project. Dr. David Fang fabricated the wafers used in the experiments with the help of John Paul DesOrmeaux and Charles Chan. Carrie Trant, Dan Mendelson, and Nakul Nataraj provided some initial characterization of the finished wafers. Dr. Michael Bindschadler wrote the pore processor program in MATLAB, which was used to analyze pore distributions for comparison to the model. Dr. Thomas Gaborski trained the author of this thesis and helped with the early experiments.

Chapter 2 was originally published in the *Journal of Membrane Science* by J.L. Snyder, A. Clark, Jr., D.Z. Fang, T.R. Gaborski, C.C. Striemer, P.M. Fauchet, and J.L. McGrath (*J. Mem. Sci.* **369**, 119-129 (2011)). Professor Alfred Clark, Jr., aided in the development of the 1-D analytic solution of diffusion across an ultrathin membrane. Dr. Clark defined the system geometry and helped to solve the problem statement. The author incorporated hindrance theory into the 1-D model and developed the 3-D model. Besides providing materials, Dr. David Fang also took micrographs of membranes used in the study.

Chapter 3 is unpublished work that was performed with the help of Paul Black from Professor William Bernhard's laboratory. Paul ran all of the DNA diffusion experiments in this work. The author performed the separations with proteins and nanoparticles and provided the theoretical analysis.

Chapter 4 is an article written by Professor James McGrath and published in *ACS Nano* by T.R. Gaborski, J.L. Snyder, C.C. Striemer, D.Z. Fang, M. Hoffman, P.M. Fauchet, and J.L. McGrath (4, 6973-6981 (2010)). The author of this thesis and Dr. Thomas Gaborski design the equilibrating permeability experimental system. Michael Hoffman studied the permeability of conventional membranes. The author performed theoretical comparisons between experiment and theory based on pore distribution results collected with help from Dr. David Fang and Maryna Kavalenka. The pressurized protein separations were performed and analyzed by the author.

Chapter 5 was submitted to the *Proceedings of the National Academy of Sciences* by J.L. Snyder, D.Z. Fang, T.R. Gaborski, C.C. Striemer, P.M. Fauchet, and J.L. McGrath. D.Z. Fang provided materials and micrographs of the membranes used in this study. The author performed the experiments and analysis found in this manuscript.

Chapter 1

Background

Nanotechnology is the study and implementation of materials with at least one dimension between 1 and 100 nm. Various fields, including biology, chemistry, physics, and engineering, intersect in the study of nanotechnology, and nanomaterials have a extensive breadth of application. Nanomaterials often have unique properties due to their size, and such properties may enable the nanomaterial to perform better in specific applications than their macroscale counterparts. In this work, a novel nanoporous membrane material, porous nanocrystalline silicon (pnc-Si), is examined and compared to conventional membrane materials. Pnc-Si is uniquely thin compared to other nanoporous membranes, and this property enables faster mass transport and lower diffusive and electrical resistance. In addition, this material provides an excellent platform for experimentation and theoretical analysis.

1.1 Current membrane technology

Membranes are a tool for rapid and inexpensive size-based separations of molecules, viruses, and cells, and are frequently used in biological, medical, and materials research as well as the food, beverage, and pharmaceutical industries. Membranes are used to separate molecules by both passive diffusion and pressurized filtration. Dialy-

sis membranes make use of diffusion for laboratory separation techniques and for the medical application of hemodialysis. Ultrafiltration membranes, or membranes having sub-micron pores, have been used to perform molecular separations by pressurized flow in an industrial setting since the 1960's [1]. However, these conventional membranes have limitations, many of which can be attributed to their architecture [2]. These membranes are fabricated from various polymers, including regenerate cellulose, polyether-sulfone, and polyvinylchloride, which form a micron-scale mesh (Fig. 1.1a). The pores within the mesh are tortuous and have log normal pore size distributions [3], factors that prevent sharp separation cutoffs. These thick membranes have a large amount of surface area for adsorption and fouling, and low abundance species may be lost to the membrane. Finally, conventional membranes face a trade off between selectivity and permeability in pressurized flow separations [1]; by enlarging pores to achieve a higher permeability, the ability to selectively filter molecules is lost.

The intelligent alteration of separation parameters and membrane properties has enabled improved separations using conventional membranes; however, this process must be tuned to each specific separation. As mobile counterions within electrolyte solutions shield the electric potential of the membrane material, by lowering the ionic concentration electrostatic interactions can be increased. Adjustment of the ionic strength of buffer can allow for charge-based tuning of separations [2]. The pH of the buffer can also be used to influence a separation by changing the charge of zwitterionic molecules and membrane materials through protination or deprotination [2]. Adsorption can be reduced by lowering protein concentrations and feed pressure and by increasing the hydrophobicity of the membranes, although different species adsorb to different degrees [4]. Several processes have been developed to mimic chromatographic separations. Chromatography remains the gold standard of separation processes, but is costly for large scale separations due to the required volume of the stationary phase. Proteins and ionic polymers have been grafted to membranes to respectively enable affinity [5] and ion exchange [6, 7] membrane chromatography; however, no membrane analog exists for

size exclusion chromatography.

The development of nanoengineered membranes with well defined pores may enable precision size-based separations unachievable by conventional materials. Two main strategies exist in the development of nanomembranes: the utilization of previously discovered nanomaterials in membrane fabrication and the transformation of a macroscale material into a membrane using top-down or bottom-up nanofabrication approaches. Nanomembranes have been made using these two strategies from a variety of different materials.

Carbon nanotube (CNT) membranes have been prepared by filling the spaces between vertically aligned nanotubes with a polymer or sealant [8, 9, 10] or by shrinking the nanotubes together using an evaporating solvent [11]. In both cases, these methods created monodisperse pore distributions with pore sizes within the range of 1-7 nm, depending on whether the nanotubes were single- or multi-walled. While such pore sizes are at the lower end for molecular separations, these membranes could be useful for buffer exchanges, removing small molecules, and potentially ion exclusion [12]. CNT membranes exhibited fluid flow rates that were larger than expected, and it is thought that fluid may slip at the hydrophobic tube interface [8, 9]. The CNT membranes in these studies were hundreds of microns to millimeters thick, and while the fluid rates were indeed higher than expected for similar length non-CNT pores, flow rate improvements may be found for thinner CNT membranes.

Ultrathin membranes have been made using nanoparticles as template materials. In one example, silica colloids were suspended in a organic film that polymerizes around the particles. The particles were removed by selectively etching with hydrofluoric acid, leaving a 2-D or 3-D porous structure depending on the thickness of the film [13, 14]. Ultrathin (5-40 nm) metallic membranes were fabricated using the polymeric structure as a template [15]. The thinnest of these membranes were not mechanically robust as freestanding films and tended to fall apart; the thickest cracked or did not faithfully reproduce the template.

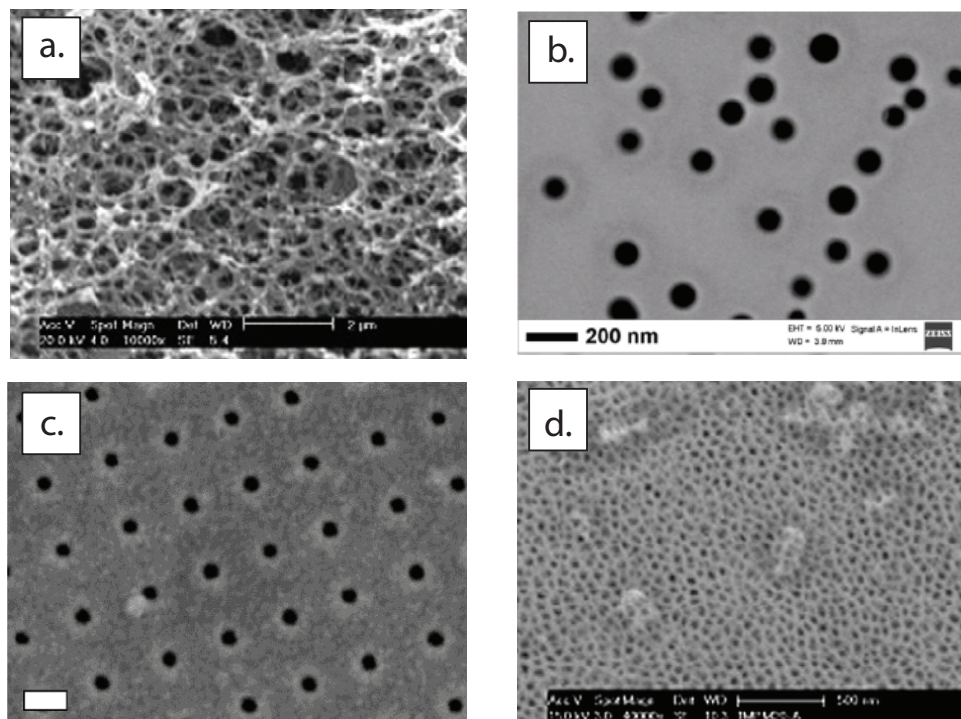


Figure 1.1: Current membrane technology. **a.** Polymer membranes appear as woven meshes and have tortuous pores. Adapted from “Enhanced permeation performance of cellulose acetate ultrafiltration membrane by incorporation of Pluonic F127,” by C. Lv *et al.*, 2007, *J. Mem. Sci.* 294:68-74. Copyright 2007 by Elsevier. Reprinted with permission. **b.** Silicon nitride track etched membranes require high energy sources to produce well defined conical pores. Adapted from “Versatile ultrathin nanoporous silicon nitride membranes,” by I. Vlassiuk *et al.*, 2009, *Proc. Natl. Acad. Sci.* 106:21039-21044. Copyright 2009 by National Academy of Sciences. Reprinted with permission. **c.** The perfectly arrayed pores in silicon nitride nanosieves are produced by individually drilling with a focused ion beam. Adapted from “Silicon nitride nanosieve membrane,” by H.D. Tong *et al.*, 2004, *Nano Lett.* 4:283-287. Copyright 2004 by American Chemical Society. Reprinted with permission. **d.** Pores in alumina membranes self assemble, although alumina membranes have not been fabricated with thicknesses below 700 nm. Adapted from “Thin alumina nanoporous membranes for similar size biomolecule separation,” by H.U. Osmanbeyoglu *et al.*, 2009, *J. Mem. Sci.* 343:1-6. Copyright 2009 by Elsevier. Reprinted with permission.

Metal hydroxide nanostrands have been used as scaffolds and coated with polymers or proteins in a series of ultrathin membranes [16, 17]. The coated nanostrands were formed into membranes by centrifugation against polycarbonate macroporous membranes. The protein membranes were cross-linked and immersed in HCl to remove the nanostrand scaffold. Filtration experiments were performed with the 40 nm thick polymer coated nanostrand and 30 nm thick protein membranes supported on a microporous polymer or alumina membrane. Pore distributions can only be inferred from separations for these membranes, and pores are likely tortuous. While membrane thickness and pore characteristics can be altered by reagent concentrations and time of centrifugation, it is unclear how reproducible these membranes are.

Several membranes have been made using a top-down nanofabrication approach, which generally involves the specific destruction or dissolution of an intact thin film in a manner that creates pores. The most common membrane in this category is the track etched membrane, which was conceived in 1963 with the irradiation of mica with U^{235} and subsequent etching of particle tracks within the material [18]. Since then, polymer films have been used in place of mica and commercialized polycarbonate track etched membranes are sold for laboratory scale separations. The polycarbonate films used to produce these membranes were 1-15 μm thick and porosities were kept low to avoid particle track overlap. Recently, 300 nm silicon nitride films were irradiated with high energy Bi or Xe ions [19]. The films were etched with H_3PO_4 and HF from one side to create conical pores or from both sides to create double conical pores (Fig. 1.1b). The constriction at the tip of the cone was over a much shorter distance than the thickness of the membranes, meaning the selective component of the membrane was on the order of 10 nm. Pore size were tuned by etching time while pore density was controlled by the irradiated ion density. Experiments showed rapid size- and charge-based separations were possible with these membranes. One drawback to this process is that high energy sources are required for the ion bombardment, which may make large scale production of these track etched membranes difficult.

A top-down approach was also used to produce a membrane described as a nanosieve, which was 10 nm thick and had an evenly spaced array of monodisperse pores [20] (Fig. 1.1c). This particular membrane was formed by suspending a 10 nm silicon nitride film over a silicon nitride microsieve perforated with 5 μm pores. Pores were individually drilled into the 10 nm film using a 30 KV gallium focused ion beam. Each perfectly positioned pore was 25 nm in diameter, and the pores were further reduced to 10 nm with the application of vapor deposited SiN. Though this membrane represents an ideal ultrathin membrane, the fabrication process is obviously very expensive and time consuming.

Bottom-up or self-assembly techniques allow for inexpensive fabrication with a high potential for scale up. Nanoporous alumina membranes are produced by anodization of thin films of aluminum in an acid electrolyte, traditionally no thinner than 20 μm to maintain strength [21]. The pores self assemble during the anodization step, and pore size can be controlled by the applied voltage. More recently, mechanically supported membranes have been fabricated through different techniques to achieve thicknesses as low as 700 nm [21, 22] (Fig. 1.1d). While ease of fabrication and high porosity make alumina an attractive material for nanomembranes, further thinning is required to obtain the benefits afforded to an ultrathin membrane.

1.2 Porous nanocrystalline silicon

Porous nanocrystalline silicon (pnc-Si) membranes are ultrathin membranes that are fabricated using bottom-up techniques (Fig. 1.2). Standard techniques in the microelectronics industry are used to produce freestanding, nanoporous, pnc-Si membranes on silicon wafers. Pnc-Si membranes are made between 7 and 30 nm thick and are freestanding with dimensions in the millimeter range. In this research, pnc-Si membranes were predominantly 15 nm thick, which has been shown to withstand applied pressures as high as an atmosphere [23]. The pores that self assemble in the material

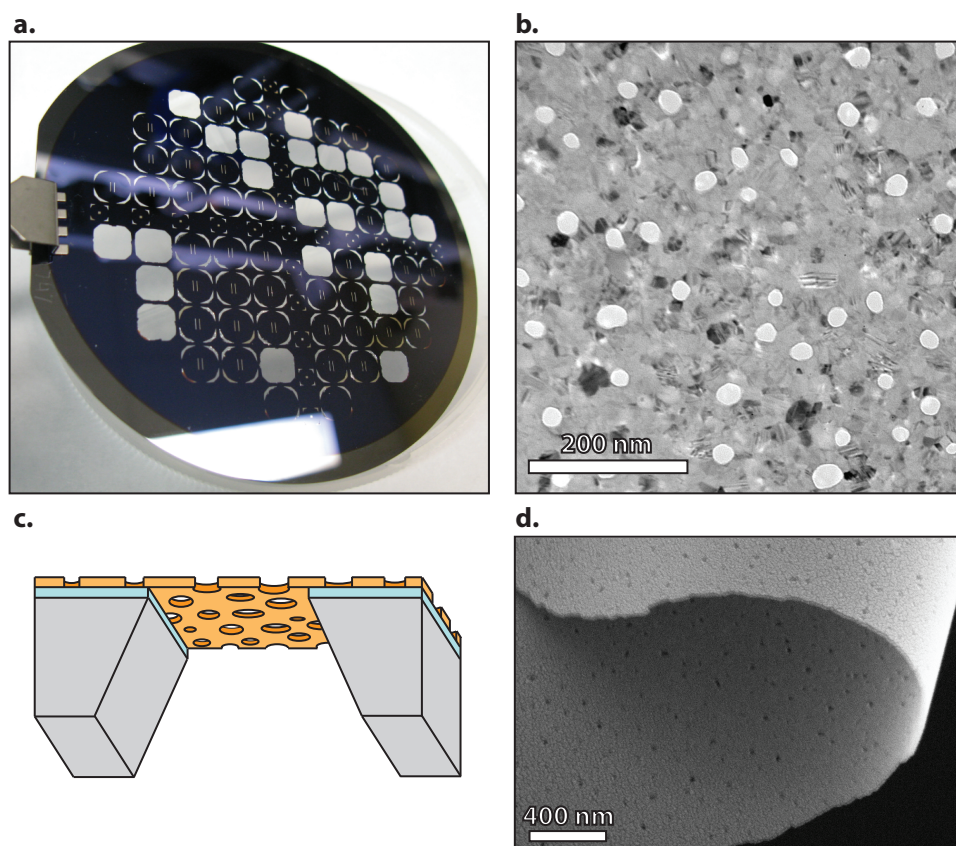


Figure 1.2: Images and schematic of pnc-Si membranes. **a.** Pnc-Si membrane material spans 2 slits on each circular chip in displayed wafer. Some chips are missing from this wafer as they have been removed for experiments. **b.** TEM micrograph of pnc-Si material. Pores are white spots, while the more electron dense nanocrystalline material appears grey. Diffracting nanocrystals appear as black spots. **c.** 3-D schematic of pnc-Si membrane. The membrane material spans the entire wafer and is freestanding over the etched bulk silicon. **d.** An SEM image at the rolled up edge of a detached membrane allows appreciation of the ultrathin quality of the material (image courtesy of Dr. Barrett Nehilla).

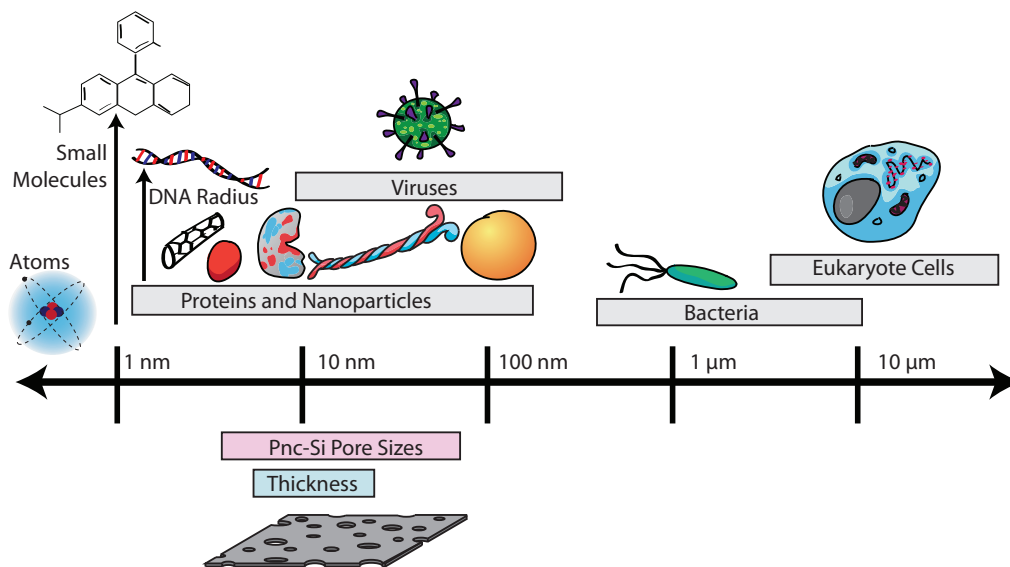


Figure 1.3: Comparison of molecular, particle, and cellular sizes to pnc-Si pores. The pore sizes of pnc-Si membranes fall within the same range as proteins, nanoparticles, and viruses and can enable separations with these species. The thickness of pnc-Si can also be tuned within this range, and proteins, nanoparticles, and viruses need only to travel a distance similar to their own dimensions to pass through the membrane.

can be tuned between 5 and 80 nm, and pore distributions have a distinct cutoff [23, 24]. The pores in pnc-Si membranes fall within the same size range as small molecules, proteins, viruses, and nanoparticles, making pnc-Si an ideal material for separations at the nanoscale (Fig 1.3). Additional applications beyond separations are possible and derive from the unique nanoscale architecture of this material. Applications reviewed in this thesis include molecular and nanoparticle separations, fluid flow, and electroosmosis, while additional work with pnc-Si has involved gas separations [25], sensors [26], and cell culture [27].

The fabrication of pnc-Si membranes is highly scalable and controllable membrane geometries are achieved through the use of photolithography techniques (details of the process are described in [23, 24]). Pnc-Si membranes are produced on small removable silicon chips, and a 4 inch wafer can contain >80 chips. Silicon dioxide is thermally

grown at 100 nm on both sides of a $\langle 100 \rangle$ silicon wafer. The backside oxide is patterned using photolithography techniques to form a mask that defines the geometry of the freestanding membranes and the boundaries of each silicon chip. The frontside oxide is replaced with a three-layer stack of 20 nm silicon dioxide/ x nm amorphous silicon/20 nm silicon dioxide via rf magnetron sputtering, where x is the desired membrane thickness. The oxide layers form a protective barrier that prevents the amorphous silicon layer from being etched in subsequent processing steps. The amorphous silicon is annealed in a rapid thermal processor, which causes voids to open between the nanocrystals that grow in the film. These voids become the pores of the membranes once the nanocrystalline film is exposed via the etching steps. Ethylene diamine pyrocatechol (EDP) is used to preferentially etch the bulk silicon according to the pattern defined by the photolithographic mask. The protective oxide layers are removed using buffered oxide etchant (BOE).

Tunable pore distributions allow membranes to be customized for applications, i.e. achieving a specific molecular weight cutoff in a protein separation. Larger pores are obtained with higher absolute annealing temperatures, sharper distributions with higher annealing ramp rates, and higher porosity with longer annealing times [24]. The thickness of the membrane also plays a role, with thicker membranes being able to support larger pores while maintaining a similar aspect ratio [24]. Since pnc-Si membranes are molecularly thin, they can be readily viewed with transmission electron microscopy. Therefore, pore distributions can be acquired by analyzing the micrographs with image processing software. Not only does the ability to directly view the pores allow membranes to be chosen for applications, but it also enables analysis of transport through pnc-Si membranes using theory.

1.3 Benefits of ultrathin membranes

The ultrathin characteristic of pnc-Si enables certain benefits over conventional membrane materials. In this thesis, the performance of pnc-Si membranes was studied in small molecule, protein, and nanoparticle separations using both diffusion and pressurized flow modalities. The permeability in pressurized flow and electroosmotically driven flow were also characterized.

Pnc-Si membranes can act as a barrier to diffusion, and molecules can be separated in a size selective manner. In diffusion separations, molecules have a reduced diffusion coefficient within the membrane due to the steric and frictional hindrance imposed by the pores. However, with ultrathin membranes, these hindrances occur over a short distance and separations progress quickly. Sharp pore distributions and well defined pores aid in the resolution of a diffusion-based separation. While many conventional membranes have log normal pore size distributions [3], the largest pores in pnc-Si membrane are constrained by the thickness and tight pore distributions are obtained through the annealing process [24]. The aspect ratio of pore diameter to thickness is greater than or equal to 1 for the majority of the pores in the distributions, and therefore the pores can be thought of as holes in a thin film. Well defined pores such as these can allow for higher resolution separations.

Faster transport of fluid can be obtained with thinner membranes. The Hagen-Poiseuille law, which holds for the laminar flow of a viscous fluid through a pipe, indicates that flow rate, Q , is inversely proportional to pipe length, L , or

$$Q = \frac{\pi R_p^4 \Delta P}{8\mu L}, \quad (1.3.1)$$

where R_p is the pipe radius, ΔP the applied pressure, and μ the viscosity of the fluid. Shorter pipes allow for faster flow rates, which remains true for the nanoscale although the standard Hagen-Poiseuille law must be modified to take into account entrance and exit effects in low aspect ratio pores (see Section 1.7). The faster fluid flow rate can

enable rapid separations by pressurized flow. The hindrance imposed by the pores also affects pressurized separations, and not all molecules smaller than the pore sizes pass easily into the filtrate with conventional membranes [28]. This results in a broad cutoff and a lower resolution separation. Once again, ultrathin membranes reduce the distance over which the hindrance occurs and enhances molecular transport. Additionally, diffusion can occur across an ultrathin membrane during pressurized separations and can increase the passage of molecules below the cutoff [3]. The presence of diffusion enhancement in a separation can be determined using the Péclet number, which is the ratio of convective to diffusive transport,

$$Pe = \frac{UL}{D}, \quad (1.3.2)$$

where U is the fluid velocity, L the length of the pore, and D the diffusion coefficient. The Péclet number is lower for ultrathin membranes where diffusion raises the resolution of the separation.

Ultrathin membranes also enable high flow rates per applied voltage when used as electroosmotic pumps (EOPs). Electroosmosis generates fluid flow through charged capillaries or pores that are placed in an electric field. The flow rate is proportional to the electric field across the EOP, and since electric field strength is related to the distance over which the field occurs, ultrathin EOPs can obtain higher fields for a given voltage [29]. By using lower applied voltages, EOPs can be efficiently run with small batteries and be integrated directly on-chip, enabling portable microfluidic devices.

1.4 Diffusion-based separations

Dialysis membranes act as a barrier to diffusion; a molecule can be purified from smaller contaminating molecules if it alone is unable to diffuse through the membrane. Dialysis is frequently used in laboratories for protein purification and buffer exchange, but it is also the leading method for treating patients with end stage renal failure (ESRD).

Kidney failure results in the inability of a patient's body to clear toxins from the blood, and to prolong life the blood must be run through an external hemodialysis system. However, both laboratory dialysis and hemodialysis are unable to separate molecules close in size, leaving unwanted contaminants in protein preparations and middle weight toxins in a patients blood. Polymeric dialysis membranes have tortuous pores and broad pore distributions. These materials are also macroscopically thick, and diffusion across the membrane is slow. The introduction of new membrane materials to both laboratory and clinical arenas can revolutionize these processes [30, 31]. Nanoengineered membranes may enable the use of dialysis within microfluidic devices, and such membranes may lead to the realization of wearable hemodialysis devices [32] or artificial organs [33].

High resolution separations by diffusion alone have not been achieved using conventional membranes, and this is most obvious when considering the inability of dialysis membranes to prevent the passage of proteins smaller than albumin [4]. Diffusion is a slow process, and long times are required to achieve equilibrium, although by reducing the system dimensions and the distance over which diffusion must occur, equilibrium can be reached more quickly. Ultrathin membranes allow for smaller systems and the distance over which membrane hindrance occurs is reduced. Diffusion separations with both pnc-Si membranes [23] and ultrathin silicon nitride track etched membranes [19] have indicated good separation characteristics over short times.

Diffusion of small species through pores is a fundamental question in both materials and biological research, as many pores, including the nuclear pore complex (NPC), aquaporins, and α -hemolysin, exist in biological membranes. A membrane with the dimensions of pnc-Si best approximates the thickness of a biological membrane, and the ability to directly visualize the pore distributions enables the development of theoretical comparisons. Previously, Kim *et al.* studied diffusion through pnc-Si using scanning electrochemical microscopy (SECM) to aid in the understanding of the NPC [34]. The NPC is constructed from 30 or more nucleoporins and is estimated to be greater than 15 nm in diameter [35]. Pnc-Si membranes with an average diameter of 11.6 nm were

chosen to compare to the NPC [34]. The SECM measurements allowed molecular flux to be immediately detected by a redox-capable probe at the membrane surface.

Kim *et al.* developed a theoretical statement for the permeability of the pnc-Si membrane by utilizing theory previously developed for molecules diffusing to adsorbing disks. Trapping rates for perfectly adsorbing disks were initially developed to compare to receptor patches on bacteria [36], although the theory could be applied to other nonhomogeneous surfaces including electrode arrays, adsorbing gold islands, or stomata in plant leaves [37]. In the case of a low surface fraction of adsorbing disks (which correlates to a low porosity), the trapping rate, k_t , was found to be

$$k_t(\chi_d) = \frac{4D_0}{\pi r} \chi_d \quad (1.4.1)$$

where σ is the disk surface fraction, D_0 the diffusion coefficient of the diffusing species in free solution, and r the radius of the disk [38]. The disk surface fraction is represented by $\chi_d = N\pi r^2$, where N is the density of disks. Kim *et al.* modified Eq. (1.4.1) to describe molecular diffusion through an ultrathin membrane by recognizing that molecules could enter and also exit the pore, giving

$$k_p(\chi) = \frac{2D}{\pi R_p} \chi = 2D_0 N R_p \quad (1.4.2)$$

where D_0 is the diffusion coefficient of the diffusing species in free solution, R_p the pore radius, and $\chi = N\pi R_p^2$ the porosity [34]. The theoretical results obtained from Eq. (1.4.2) and pnc-Si pore distributions agreed with experimental SECM measurements. These results were further used to compare to SECM data from *Xenopus* NPC, allowing for the conclusion that the NPC is larger than the pores in the pnc-Si membrane.

The permeability, k_p , in Eq. (1.4.2) compares well with experimental results for a variety of small molecules as shown in Fig. 1.4. However, for larger molecules and charged species, the experimental permeabilities were lower than expected by theory [34, 39]. This is due to the fact that the permeability, k_p , does not account for the

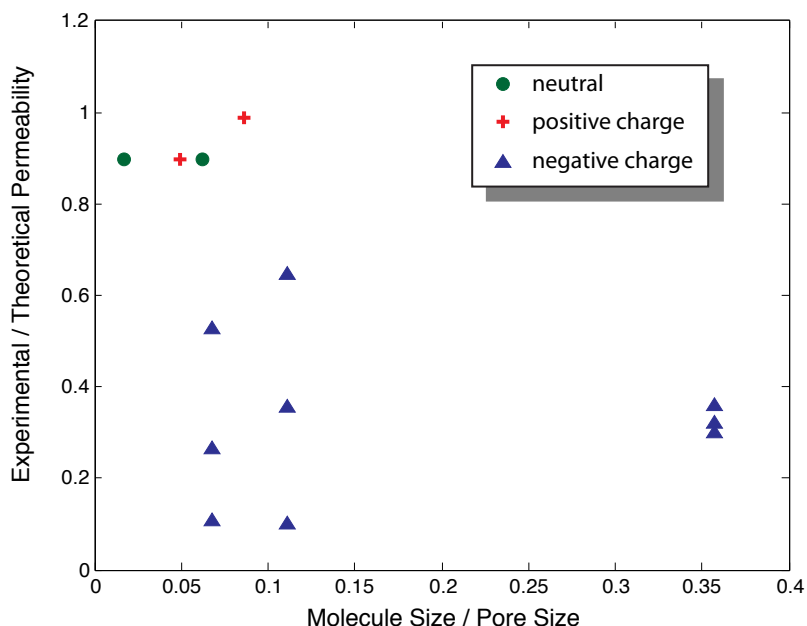


Figure 1.4: Experimental and theoretical comparison of thin membrane permeability. Experimental results from separations with pnc-Si membranes by the Amemiya group are compared to the theoretical thin membrane permeability, Eq. (1.4.2) [34, 39]. The experiment agrees with theory for small molecules that are uncharged or positively charged. Larger, negatively charged molecules deviate from theoretical predictions. The deviation is due to both the steric and frictional hindrance a large molecule experiences in a pore and the electrostatic repulsion between the negatively charged membrane and molecules. (Experiments were performed at three salt concentrations for each negatively charged molecule - 0.1, 0.03, and 0.01 M KCl)

hindrance to molecular diffusion by the pore. The closer in size the molecule is to the pore size, the greater extent to which the membrane slows the diffusion of the molecule. Long standing theories attempt to describe the hindrance imparted by a membrane.

1.5 Hindrance theory

In 1954, Renkin developed a statement for membrane hindrance by combining a steric condition at the opening (first term on the right hand side) of the pore and the frictional

resistance imparted by the pore (second term):

$$\frac{D_m}{D_0} = \left(1 - \frac{R_s}{R_p}\right)^2 \left[1 - 2.104\left(\frac{R_s}{R_p}\right) + 2.09\left(\frac{R_s}{R_p}\right)^3 - 0.95\left(\frac{R_s}{R_p}\right)^5\right] \quad (1.5.1)$$

where D_m is the effective membrane diffusion coefficient of a molecule, D_0 is the free diffusion coefficient, R_s the molecule radius, and R_p the pore radius [40]. Experimental results compared well with the Renkin equation to an R_s/R_p ratio of 0.4 [40, 41, 42]. This original treatment considers that the molecule travels along the central axis of the pore as it passes through the membrane, a so called centerline approximation. Subsequent treatments have developed both centerline and radially averaged versions of Eq. (1.5.1) that are applicable up to an R_s/R_p ratio of 0.95. The best centerline approximations deviate only slightly from the radially averaged versions of the equation [43].

The steric condition of entrance into a pore, can be represented by a partition coefficient, ϕ ,

$$\phi = 2 \int_0^{1-\lambda} e^{-\mathbb{E}/k_b T} \rho \, d\rho \quad (1.5.2)$$

where λ is the R_s/R_p ratio and ρ a radial parameter. In essence, the partition coefficient describes the ratio of solubility within the pore to that directly outside the pore [44]. The Boltzmann factor $e^{-\mathbb{E}/k_b T}$ accounts for energies, \mathbb{E} , that force a molecule into a specific position in the pore and change the inner pore solubility (k_b is the Boltzmann constant and T the temperature), an electric potential at the pore wall being the most common effect. In the absence of electrostatic effects, $\mathbb{E} = 0$, and Eq. (1.5.2) reduces to the first term on the right hand side of Eq (1.5.1) for the case of a circular pore.

The frictional resistance can be found by determining what is called a hindrance factor or reduced diffusivity, K_d ,

$$K_d = \frac{\int_0^{1-\lambda} K^{-1} e^{-\mathbb{E}/kT} \rho \, d\rho}{\int_0^{1-\lambda} e^{-\mathbb{E}/kT} \rho \, d\rho} \quad (1.5.3)$$

where K is the enhanced drag, or the ratio of drag on a sphere within a pore to that of a free sphere [43, 45]. Again, $\mathbb{E} = 0$ can be used to neglect electrostatic effects. Centerline approximations are taken for $\rho = 0$, the most accurate of which was developed by Bungay and Brenner in 1973 and is comprised of 14 terms found by asymptotic matching [43, 46]. Dechadilok and Deen combined two radially averaged solutions, one accurate over $0 \leq \lambda \leq 0.9$ [47] and one developed for $\lambda = 0.95$ [48], to achieve accuracy over the range $0 \leq \lambda \leq 0.95$ by a least squares fit. When the partition coefficient is added to the radially averaged hindrance factor, the following hindrance equation is obtained [43],

$$\begin{aligned} \frac{D_m}{D_0} = & \\ & 1 + \frac{9}{8}\lambda \ln \lambda - 1.56034\lambda + 0.528155\lambda^2 + 1.91521\lambda^3 - 2.81903\lambda^4 + \\ & 0.270788\lambda^5 + 1.1015\lambda^6 - 0.435933\lambda^7. \end{aligned} \quad (1.5.4)$$

In Chapter 2, a model to describe diffusion through an ultrathin membrane is developed using Eq. (1.4.2) for diffusion to the pores of an ultrathin material and Eq. (1.5.4) for the hindrance the pores impart to the molecules as they pass through the material. These two statements of diffusion are combined by once again looking back to the adsorbing disks theory. In the case that the disks only partially adsorb molecules, an additional trapping rate that relates to the partial rejection is added to the permeability as conductances in series [37]. For a porous membrane, the permeability due to the diffusion to pores is added to the permeability related to the hindered diffusion as conductances in series. Notably, the diffusion to the pores is only relevant for the case of a thin membrane; the resistance imparted by diffusion through a thick membrane greatly outweighs this effect.

Table 1.1: Debye lengths of symmetric salt solutions.

Salt concentration (M)	Debye length (nm)
0.1	0.97
0.05	1.37
0.01	3.07
0.001	9.71

1.6 Charge-based separations

Besides using a membrane as a size selective barrier, electrostatic effects between membranes and the species being separated can be exploited for charge-based separations. Charged species can be slowed or prevented from passing through a like charged membrane. However, such effects are only present in solutions of low ionic strength because of ionic shielding. As a charged material comes into contact with an electrolyte, ions of opposite charge associate with the surface forming an electrical double layer (EDL) [49, 50]. Some of the ions within the EDL adsorb to the surface while the rest are loosely associated in a diffuse layer. Because of the shielding by the counterions, the electric potential exponentially decays away from the surface. The Debye length, κ^{-1} , is the distance from the surface at which the electrical potential is equal to $1/e$ times the surface potential and is related to the thickness of the EDL,

$$\kappa^{-1} = \sqrt{\frac{\epsilon k_b T}{2q^2 c}}. \quad (1.6.1)$$

where q and c are respectively the ionic charge and concentration [50]. Debye lengths for common salt concentrations are displayed in Table 1.1. At long Debye lengths, the electric potential extends a greater distance into the pore and can effectively reduce pore sizes to like charged species due to repulsive interactions.

Charge-based separations at low ionic concentrations have been of interest for membrane research and are relevant to both conventional and nanoengineered membranes.

Menon and Zydney developed a charge ladder by progressively acetylating lysines on the proteins myoglobin and carbonic anhydrase [51]. These ladders were used to test the charge discrimination of polymeric membranes under forced flow conditions. The results showed that at high ionic strength there was little difference in separations between the protein and the similarly sized acetylated derivatives, but that distinct differences in separation characteristics occurred for lower ionic concentration solutions. Nanoporous alumina membranes have been used to separate the similarly sized bovine serum albumin (BSA, 67 kDa) and bovine hemoglobin (BHb, 65 kDa) at 10 mM phosphate buffered saline [22]. Early experiments with pnc-Si membranes indicated that the innate negative charge of pnc-Si could reduce the diffusion of negatively charged small molecules [23, 34, 39].

Hindrance theory has been used to model charge-based interactions. The simplest treatment subtracts the Debye length from the pore radius and adds it to the molecular radius [52]. While this consideration of charge effects does result in better comparison to experiments at low ionic concentrations, it remains a rough treatment of the problem as the Debye length is a mathematical construct and not the length of a distinct boundary. Smith and Deen present a radial solution of the partition coefficient, Eq. (1.5.2), taking into account electrostatic effects in the Boltzmann factor [53]. Comparisons were made to experimental results using spherical Ficoll polymers and nanoporous track etched membranes and, while the experiments follow the separation trends the model proposes for different salt concentrations, the findings deviate from the model [54]. Dechadilok and Deen combined the partition coefficients from the analysis by Smith and Deen with centerline hindrance factors and the relaxation effect [45]. Centerline hindrance factors were used for simplicity and because electrostatic effects should bias the molecules toward the center of the pore. The relaxation effect is a retarding force on diffusion due to the shifting of the diffuse layer of ions around a molecule as it diffuses. While this treatment was not compared with experimental results, it was found that the contribution of electrostatic hindrance from the partition coefficient far outweighed any contribution

from the relaxation effect.

In Chapter 3, the effects of charge on separations with pnc-Si membranes are further studied. DNA, which has a negatively charged phosphate backbone, proteins, and nanoparticles are separated using negatively charged pnc-Si membranes at various salt concentrations. Concepts from the theoretical models described above are used to investigate the effects of charge on the separations.

1.7 Pressurized separations and fluid flow

Conventional polymeric membranes are used for a variety of research and industrial separations, though tradeoffs between selectivity and permeability reduce the applicability of these membranes [1, 2]. Nanoengineered membranes with tighter pore distributions and thinner, less fluid resistant architecture may create new opportunities for membrane filtration.

As mentioned in Section 1.3, the flow rate through a long pipe or capillary is inversely proportional to the length of the pipe. Ultrathin membranes have an extremely small pore length, and therefore are expected to provide little resistance to fluid flow. In such short pores, the Hagen-Poiseuille formula must be corrected to take into account entrance and exit effects. In 1983, Dagan, Weinbaum, and Pfeiffer theoretically investigated fluid flow in short apertures, and found that the fluid profile nearly approaches a typical Hagen-Poiseuille parabolic profile when $L \approx R_p/2$ [55]. This work led to the following simple algebraic relationship for fluid flow through a low aspect ratio pore

$$Q = \frac{R_p^3 \Delta P}{\mu \left[3 + \frac{8}{\pi} \left(\frac{L}{R_p} \right) \right]}. \quad (1.7.1)$$

This equation reduces to Eq. (1.3.2) when L/R_p is large. Tong *et al.* added terms to Eq. (1.7.1) to account for influence of neighboring pores and an additional pressure drop at the pore entrance for cases of high flow rates [20]; however, the influence of these additional effects appears to be minimal for the low porosity pnc-Si membranes used

in this research. Thus, using knowledge of pore distributions, theory can be compared with pressurized experiments.

Membranes are used for separations of molecules and nanoparticles; however, a 10x size difference is often required for complete separations with conventional membranes. Frequently used polymeric membranes have tortuous pores with log normal pore size distributions [51]. To improve selectivity, well defined pores with tight distributions are required. However, improving the selectivity by reducing the breadth of the pore distributions generally leads to a loss in permeability [1]. Therefore conventional membranes must be chosen as high flux and low selectivity or low flux and high selectivity for a given separation.

Recent development of techniques and membranes has improved the selectivity in protein and nanoparticle separations. Proteins that are as low as 2x different in size were separated with polymer by carefully optimizing membrane pore size, chemistry, buffer chemistry, and fluid flow rates through the membrane [2]. Separations between gold nanoparticles 2x different in size were performed using a diafiltration process and a hollow fiber polymer membrane, though the samples were diluted 15x and required concentration steps after the filtration [56]. Carbon nanotube membranes with 3.6 nm pores were used to completely remove 3.2 nm gold from water, though the pores may be too small to separate closely sized particles. The results of these separations were highly variable, which indicates that the fabrication of CNT membranes is a highly variable process. Gold coated track etched membranes were able to separate two proteins with 2x size difference through pores 4x larger than the largest protein, although lower concentrations of the large protein was used in the protein mixtures [57]. Long slit pores have been shown to offer high permeability but also selectivity provided by the short axis of the pore [31]. Hemofiltration with slit pore membranes has allowed for a difference in transport of molecules with a ~ 5 nm size difference, but not complete separation [58].

In Chapter 4, the fluid flow rates of pnc-Si membranes are compared to other

nanoporous membranes and theory. Pnc-Si pore distributions as determined by TEM allow for direct comparison to fluid flow theory. Separations with both nanoparticles and proteins are performed to illustrate the selectivity of pnc-Si.

1.8 Electroosmosis

The fabrication of electroosmotic pumps, or EOPs, has been of recent interest to microfluidics research. Compared to mechanical pumps, EOPs have no moving parts and are able to generate pulse free flows [59]. They have been proposed to pressurize microfluidic diagnostic chips [60, 61] or cooling circuits for computers [62]. The use of electrodes for pump actuation would enable better control of pumping, and the development of small on-chip EOPs would allow for higher portability and ease of use for integrated devices. However, many of the current EOPs require high voltages (>1 kV) to achieve the electric fields necessary for sufficient flow rates [63, 64]. Thinning of EOPs has been proposed to reduce voltages required for the needed flow rates [29], though the thickness of current “thin” EOPs is still on the micron scale [65, 66].

EOPs are produced from various negatively charged materials, and while porosity is a benefit, not all EOPs are designed using membranes. Silica particles have been packed between glass frits in a capillary to produce a porous, electroosmosis capable plug [63]. Packed silica EOPs are simple and inexpensive to produce; however, there exists a minimum thickness based on the micron scale particle dimensions. Aluminum oxide membranes have been designed into EOPs, although pumps below $60\text{ }\mu\text{m}$ thick have not yet been demonstrated [65]. EOPs that are $350\text{ }\mu\text{m}$ thick have been produced using anodically etched porous silicon, which is more similar in structure to alumina than pnc-Si [66]. Both alumina and porous silicon membranes have produced high flow rates for low voltage, but thinner pumps are expected to have better voltage specific performance characteristics [29]. Pnc-Si is the thinnest material capable of electroosmosis, and may be an ideal material for a low voltage EOP.

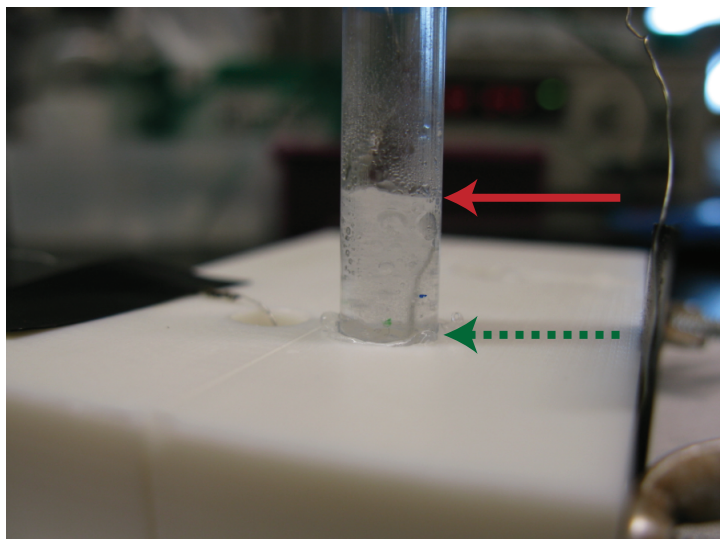


Figure 1.5: Early electroosmosis experiment with pnc-Si. The fluid is pumped through the membrane and up a vertical column. The green dotted arrow represents the starting fluid level and the red solid arrow the final. The flow rate was calculated to be roughly $\sim 10 \mu\text{L}/\text{min}$; bubbles generated via electrolysis make an accurate measurement in this system difficult.

After testing pnc-Si membranes in both diffusion and pressurized flow separations, experiments were performed using pnc-Si membranes as a selective medium for electrophoretic separations. While small molecules appeared to pass through the membrane when an electric field was applied to the system, a large amount of water flow toward the negative electrode was observed. Early estimates put this flow at $\sim 10 \mu\text{L}/\text{min}$ up a column against gravity (Fig. 1.5). The water flow was determined to be a result of electroosmosis. Subsequent characterization of the flow rates confirmed that electroosmosis through pnc-Si membranes was higher than polymeric and track etched membranes.

Electroosmosis is one of four electrokinetic phenomena, a group which also includes electrophoresis, streaming potential, and sedimentation potential [49, 50]. All electrokinetic phenomena exist due to the electrical double layer (EDL) that forms at the surface of the material as described in Section 1.6. In the presence of a force, the diffuse layer moves against the surface at the edge of the adsorbed layer, a boundary called the surface of shear. It is at this point that a potential, the zeta potential, can be measured

using the electrokinetic phenomena. The zeta potential is not of the same magnitude as the surface potential due to the adsorbed ions, but it is a useful metric to characterize a surface. The magnitude of the zeta potential is proportional to the strength of the electrokinetic phenomena.

The four electrokinetic phenomena are related, although they differ by whether fluid or material is stationary and the force applied to the system. In the case of electroosmosis the material is stationary and the applied force is an electric field. The electric field causes the ions within the diffuse layer to migrate toward the electrode of opposite sign. In the case of a capillary or pore, the ions form an annulus of moving charges. For small diameter capillaries or pores ($<1 \mu\text{m}$), the bulk electrolyte will migrate as well due to viscous drag. Theory for electroosmotic flow, which was developed for long capillaries, states that the velocity of fluid, U , is proportional to the zeta potential, ζ , and electric field, E ,

$$U = -\frac{\epsilon\zeta E}{\mu} \quad (1.8.1)$$

where ϵ and μ are the permittivity and viscosity of the fluid [49, 50]. The sign of the equation denotes the direction of electroosmotic flow. To maximize electroosmotic flow, the material must have a high zeta potential and the field applied across the material must also be large.

Streaming potential, another electrokinetic phenomenon and the opposite of electroosmosis, is commonly used to characterize the zeta potential of membranes [67]. For streaming potential, while the surface again remains stationary, the applied force is pressure. As the electrolyte fluid is pressurized through the membrane, the moving diffuse layer of ions develop what is called a streaming current. Because of the current, there is a small amount of generated electroosmosis but also ionic back flow. At steady state, the streaming potential can be measured between two electrodes. To obtain zeta

potential measurements, Eq. (1.8.1) is first rewritten to express volumetric flow,

$$Q = -\frac{\epsilon\zeta I}{\mu k} \quad (1.8.2)$$

where I is the measured current and k is the conductivity of the solution. Using Onsager's reciprocity rules, $Q/I = \Phi_s/\Delta P$, the streaming potential, Φ_s , can be expressed as

$$\frac{\Phi_s}{\Delta P} = -\frac{\epsilon\zeta}{\mu k} \quad (1.8.3)$$

where ΔP is the applied pressure [68]. Streaming potential measurements can be carried out for a series of pressures, and the zeta potential can be determined from the slope of a linear Φ_s vs. ΔP curve.

In Chapter 5, electroosmotic flow rates of pnc-Si membranes are thoroughly characterized. Surface modifications of the material are performed to change the zeta potential of the material and thereby alter the flow rates. Comparisons to other materials indicate that pnc-Si has the highest innate electroosmotic flow rate, which is a function of the high electric fields capable of forming across the 15 nm membrane.

1.9 Thesis Organization

To summarize, the internal chapters of this thesis discuss four main research projects with pnc-Si membranes. Chapter 2, **Diffusion Separations**, features pnc-Si membranes as a size selective barrier for the separation of small molecules and proteins by diffusion. This work was originally featured in an article written for the *Journal of Membrane Science*. Chapter 3, **Charge-Based Separations**, contains an unpublished account of the diffusion of molecules and nanoparticles at low ionic concentrations, and the effects of electrostatic interactions between the membrane and diffusing species. Chapter 4, **Pressurized Separations**, was originally published in *ACS Nano* and discusses the use of pnc-Si membranes in pressurized systems. Chapter 5, **Electroos-**

mosis, has been submitted to the *Proceedings of the National Academy of Sciences* and contains experimental and theoretical analysis of pnc-Si as an electroosmotic material. Finally, Chapter 6, **Concluding Remarks**, is a discussion of the results presented in the previous chapters and the future direction of this work.

1.10 References

- [1] A. Mehta, A.L. Zydney, Permeability and selectivity analysis for ultrafiltration membranes. *J. Mem. Sci* **249**, 245-249 (2005).
- [2] R. van Reis, S. Gadam, L.N. Frautschy, S. Orlando, E.M. Goodrich, S. Saksena, R. Kuriyel, C.M. Simpson, S. Pearl, A.L. Zydney, High performance tangential flow filtration, *Biotech. Bioeng.* **56**, 71-82 (1997).
- [3] S. Mochizuki, A.L. Zydney, Theoretical analysis of pore size distribution effects on membrane transport, *J. Mem. Sci.* **82**, 211-227 (1993).
- [4] S. Loh, U. Beuscher, T.K. Poddar, A.G. Porter, J.M. Wingard, S.M. Husson, S. R. Wickramasinghe, Interplay among membrane properties, protein properties and operating conditions on protein fouling during normal-flow microfiltration, *J. Mem. Sci* **332**, 93-103 (2009).
- [5] D. Yu, M.D. McLean, J.C. Hall, R. Ghosh, Purification of a human immunoglobulin G1 monoclonal antibody from transgenic tobacco using membrane chromatographic processes, *J. Chromatography A* **1187**, 128-137 (2008).
- [6] B.V. Bhut, S.R. Wickramasinghe, S.M. Husson, Preparation of high-capacity, weak anion-exchange membranes for protein separations using surface-initiated atom transfer radical polymerization, *J. Mem. Sci.* **325**, 176-183 (2008).

-
- [7] B.V. Bhut, S.M. Husson, Dramatic performance improvement of weak anion-exchange membranes for chromatographic bioseparations, *J. Mem. Sci.* **337**, 215-223 (2009).
- [8] B.J. Hinds, N. Chopra, T. Rantell, R. Andrews, V. Gavalas, L.G. Bachas, Aligned multiwalled carbon nanotube membranes, *Science* **303**, 62-65 (2004).
- [9] J.K. Holt, H.G. Park, Y. Wang, M. Stadermann, A.B. Artyukhin, C.P. Grigoropoulos, A. Noy, O. Bakajin, Fast mass transport through sub-2-nanometer carbon nanotubes, *Science* **312**, 1034-1037 (2006).
- [10] S. Kim, J.R. Jinschek, H. Chen, D.S. Sholl, E. Marand, Scalable fabrication of carbon nanotube/polymer nanocomposite membranes for high flux gas transport. *Nano Lett.* **7**, 2806-2811 (2007).
- [11] M. Yu, H.H. Funke, J.L. Falconer, R.D. Noble, High density, vertically-aligned carbon nanotube membranes, *Nano Lett.* **9**, 225-229 (2009).
- [12] F. Fornasiero, H. Gyu-Park, J.K. Holt, M. Stadermann, C.P. Grigoropoulos, A. Noy, O. Bakajin, Ion exclusion by sub-2-nm carbon nanotube pore, *Proc. Natl. Acad. Sci.* **105**, 17250-17255 (2008).
- [13] H. Xu, W.A. Goedel. mesoscopic rings by controlled wetting of particle imprinted templates, *Angew. Chem. Int. Ed.* **42**, 4696-4700 (2003).
- [14] F. Yan, W.A. Goedel, A simple and effective method for the preparation of porous membranes with three-dimensionally arranged pores, *Adv. Mater.* **16**, 911-915 (2004).
- [15] H. Xu, W.A. Goedel. Preparation of ultrathin free-standing porous metal films, *Small* **8-9**, 808-812 (2005).
- [16] X.S. Peng, J. Jin, I. Ichinose, Mesoporous separation membranes of polymer-coated copper hydroxide nanostrands, *Adv. Funct. Mater* **17**, 1849-1855 (2007).

-
- [17] X. Peng, J. Jin, Y. Nakamura, T. Ohno, I. Ichinose, Ultrafast permeation of water through protein-based membranes. *Nat. Nanotechnol.* **4** 353-357 (2009).
- [18] R.L. Fleischer, H.W. Alter, S.C. Furman, P.B. Price, R.M. Walker, Particle track etching *Science* **178**, 255-263 (1972).
- [19] I. Vlassiuk, P.Y. Apel, S.N. Dmitriev, K. Healy, Z.S. Siwy, Versatile ultrathin nanoporous silicon nitride membranes, *Proc. Natl. Acad. Sci.* **106**, 21039-21044 (2009).
- [20] H.D. Tong, H.V. Jansen, V.J. Gadgil, C.G. Bostan, E. Berenschot, E. C.J.M. van Rijn, M. Elwenspoek, Silicon nitride nanosieve membrane, *Nano Lett.* **4**, 283-287 (2004).
- [21] A. Thormann, N. Teuscher, M. Pfannmöller, U. Rothe, A. Heilmann, Nanoporous aluminum oxide membranes for filtration and biofunctionalization, *Small* **3**, 1032-1040 (2007).
- [22] H.U. Osmanbeyoglu, T.B. Hur, H.K. Kim, Thin alumina nanoporous membranes for similar size biomolecule separation, *J. Mem. Sci.* **343**, 1-6 (2009).
- [23] C.C. Striemer, T.R. Gaborski, J.L. McGrath, P.M. Fauchet, Charge- and size-based separation of macromolecules using ultrathin silicon membranes, *Nature* **445**, 749-753 (2007).
- [24] D.Z. Fang, C.C. Striemer, T.R. Gaborski, J.L. McGrath, P.M. Fauchet, Methods for controlling the pore properties of ultra-thin nanocrystalline silicon membranes, *J. Phys.: Condens. Matter* **22**, 454134 (2010).
- [25] M.N. Kavalenka, C.C. Striemer, D.Z. Fang, K. Shome, T.R. Gaborski, J.L. McGrath, P.M. Fauchet, Ballistic and non-ballistic gas flow through ultrathin nanopores *Phys. Rev. Lett* In Review.

- [26] M.N. Kavalenka, D.Z. Fang, C.C. Striemer, J.L. McGrath, P.M. Fauchet, Hybrid polymer/ultrathin porous nanocrystalline silicon membranes system for flow-through chemical vapor and gas detection, *Active Polymers* 199-204 (2009).
- [27] A.A. Agrawal, B.J. Nehilla, K.V. Reisig, T.R. Gaborski, D.Z. Fang, C.C. Striemer, P.M. Fauchet, J.L. McGrath, Porous nanocrystalline silicon membranes as highly permeable and molecularly thin substrates for cell culture, *Biomaterials* **31**, 5408-5417 (2010).
- [28] A.S. Michaels, Analysis and prediction of sieving curves for ultrafiltration membranes: a universal correlation? *Sep. Sci. Technol.* **15**, 1305-1322 (1980).
- [29] S. Yao, D.E. Hertzog, S. Zeng, J.C. Mikkelsen, J.G. Santiago, Porous glass electroosmotic: design and experiments, *J. Colloid Interf. Sci.* **268**, 143-153 (2003).
- [30] M.D. Luque de Castro, F. Priego Capote, N. Sánchez Ávila, Is dialysis alive as a membrane-based separations technique? *TrAC, Trends Anal. Chem.* **27**, 315-326 (2008).
- [31] W.H. Fissell, H.D. Humes, A.J. Fleischman, S. Roy, Dialysis and nanotechnology: now, 10 years, or never? *Blood Purif.* **25**, 12-17 (2007).
- [32] J.P. Kooman, F.M. van der Sande, K.M. Leunissen, The long road to wearable blood-cleansing devices, *Blood Purif.* **25**, 377-382 (2007).
- [33] W.H. Fissell, S. Manley, A. Westover, H.D. Humes, A.J. Fleischman, S. Roy. Differentiated growth of human renal tubule cells on thin-film and nanostructured materials, *ASAIO J* **52** 221-227 (2006).
- [34] E. Kim, H. Xiong, C.C. Striemer, D.Z. Fang, P.M. Fauchet, J.L. McGrath, S. Amemiya, A structure-permeability relationship of ultrathin nanoporous silicon membrane: a comparison with the nuclear envelope, *J. Am. Chem. Soc.* **130**, 4230-4231 (2008).

- [35] J. Guo, S. Amemiya. Permeability of the nuclear envelope at isolated *Xenopus* oocyte nuclei studied by scanning electrochemical microscopy. *Anal. Chem.* **77** 2147-2156 (2005).
- [36] H.C. Berg, E.M. Purcell. Physics of chemoreception, *Biophys. J.* **20**, 193-219 (1977).
- [37] A.M. Berezhkovskii, Y.A. Makhnovskii, M.I. Monine, V.Y. Zitserman, S.Y. Shvartsman, Boundary homogenization for trapping by patchy surfaces. *J. Chem. Phys.* **121**, 11390-11394 (2004).
- [38] Y.A. Makhnovskii, A.M. Berezhkovskii, V.Y. Zitserman, Homogenization of boundary conditions on surfaces randomly covered by patches of different sizes and shapes, *J. Chem. Phys.* **122**, 236102 (2005).
- [39] R. Ishimatsu, J. Kim, P. Jing, C.C. Striemer, D.Z. Fang, P.M. Fauchet, J.L. McGrath, S. Amemiya, Ion-selective permeability of an ultrathin nanopore silicon membrane as probed by scanning electrochemical microscopy using micropipet-supported ITIES tips, *Anal. Chem.* **82**, 7127-7134 (2010).
- [40] E.M. Renkin, Filtration, diffusion, and molecular sieving through porous cellulose membranes, *J. Gen. Physiol.* **38**, 225-243 (1954).
- [41] R.E. Beck, J.S. Schultz, Hindered diffusion in microporous membranes with known pore geometry, *Science* **170**, 1302-1305 (1970).
- [42] W.M. Deen, Hindered transport of large molecules in liquid-filled pores, *AIChE J.* **33**, 1409-1425 (1987).
- [43] P. Dechadilok, W.M. Deen, Hindrance factors for diffusion and convection in pores, *Ind. Eng. Chem. Res.* **45**, 6953-6959 (2006).
- [44] T.F. Weiss, *Cellular Biophysics, Vol. 1: Transport* (MIT Press, Cambridge, MA, 1996) pp. 119-137.

-
- [45] P. Dechadilok, W.M. Deen, Electrostatic and electrokinetic effects on hindered diffusion in pores, *J. Mem. Sci* **336**, 7-16 (2009).
- [46] P.M. Bungay, H. Brenner, The motion of a closely-fitting sphere in a fluid-filled tube, *Int. J. Multiphase Flow* **1**, 25-56 (1973).
- [47] J.J.L. Higdon, G.P. Muldowney, Resistance functions for spherical particles, droplets and bubbles in cylindrical tubes, *J. Fluid Mech* **298**, 193-210 (1995).
- [48] G.M. Mavrovouniotis, H. Brenner, Hindered sedimentation, diffusion, and dispersion coefficients for brownian spheres in circular cylindrical pores, *J. Colloid Interf. Sci* **124**, 269-283 (1988).
- [49] P.C. Hiemenz, R. Rajagopalan, *Principles of colloid and surface chemistry* (Marcel Dekker, New York, ed. 3, 1997) pp. 534-574.
- [50] R.F. Probstein, *Physicochemical Hydrodynamics* (Wiley, Hoboken, NJ, ed. 2, 2003) pp. 165-236.
- [51] M.K. Menon, A.L. Zydney, Protein charge ladders: a new technique for studying electrostatic interactions in ultrafiltration systems, *J. Mem. Sci.* **181**, 179-184 (2001).
- [52] W.D. Munch, L.P. Zestar, J.L. Anderson, Rejection of polyelectrolytes from microporous membranes, *J. Mem. Sci.* **5**, 77-102 (1979).
- [53] F.G. Smith, W.M. Deen, Electrostatic effects on the partitioning of spherical colloids between dilute bulk solution and cylindrical pores, *J. Colloid Interf. Sci* **91**, 579-589 (1983).
- [54] W.M. Deen, F.G. Smith, Hindered diffusion of synthetic polyelectrolytes in charged microporous membranes, *J. Mem. Sci.* **12**, 217-237 (1982).
- [55] Z. Dagan, S. Weinbaum, R. Pfeffer, An infinite-series solution for the creeping motion through an orifice of finite length, *J. Fluid Mech.* **115**, 505-523 (1982).

-
- [56] S.F. Sweeney, G.H. Woerhrle, J.E. Hutchinson, Rapid purification and size separation of gold nanoparticles via diafiltration, *J. Am. Chem. Soc.* **128**, 3190-3197 (2006).
- [57] S. Yu, S.B. Lee, M. Kang, C.R. Martin, Size-based protein separations in poly(ethylene glycol)-derivatized gold nanotubule membranes, *Nano Lett.* **1**, 495-498 (2001).
- [58] A.T. Conlisk, S. Datta, W.H. Fissell, S. Roy, Biomolecular transport through hemofiltration membranes, *Ann. Biomed. Eng.* **37**, 722-736 (2009).
- [59] X. Wang, C. Cheng, S. Wang, S. Liu, Electroosmotic pumps and their applications in microfluidic systems, *Microfluid. Nanofluid.* **6**, 145-162 (2009).
- [60] N.-C. Tsai, C.-Y. Sue. Review of MEMS-based drug delivery and dosing systems, *Sensor. Actuat. A-Phys.* **134**, 555-564 (2007).
- [61] E.L.P. Uhlig, W.F. Graydon. The electro-osmotic actuation of implantable insulin micropumps, *J. Biomed. Mater. Res.* **17**, 931-943 (1983).
- [62] L. Jiang, J. Mikkelsen, J.-M. Koo, D. Huber, S. Yao, L. Zhang, P. Zhou, J.G. Maveety, R. Prasher, J.G. Santiago, T.W. Kenny, K.E. Goodson. Closed-loop electroosmotic microchannel cooling system for VLSI circuits, *IEEE T. Compon. Pack. T.* **25**, 347-355 (2002).
- [63] S. Zeng, C.-H. Chen, J. C. Mikkelsen Jr., J.G. Santiago. Fabrication and characterization of electroosmotic pumps, *Sensors Actuators B.* **79**, 107-114 (2001).
- [64] W.-E. Gan, L. Yang, Y.-Z. He, R.-H. Zeng, M.L. Cervera, M. de la Guardia. Mechanism of porous core electroosmotic pump flow injection system and its application to determination of chromium(VI) in waste-water, *Talanta* **51**, 667-675 (2000).

-
- [65] S.K. Vajandar, D. Xu, D.A. Markov, J.P. Wikswo, W. Hofmeister, D. Li, SiO₂-coated porous anodic alumina membranes for high flow rate electroosmotic pumping, *Nanotechnology* **18** 275705 (2007).
- [66] S. Yao, A.M. Myers, J.D. Posner, K.A. Rose, J.G. Santiago. Electroosmotic pumps fabricated from porous silicon membranes, *J. Microelectromech. Sys.* **15**, 717-728 (2006).
- [67] D.B. Burns, A.L. Zydney, Buffer effects on the zeta potential of ultrafiltration membranes, *J. Mem. Sci.* **172**, 39-48 (2000).
- [68] K.J. Kim, A.G. Fane, M. Nystrom, A. Pihlajamaki, W.R. Bowen, H. Mukhtar, Evaluation of electroosmosis and streaming potential for measurement of polymeric membranes, *J. Mem. Sci.* **116**, 149-159 (1996).

Chapter 2

Diffusion Separations[†]

2.1 Abstract

Diffusion based separations are essential for laboratory and clinical dialysis processes. New molecularly thin nanoporous membranes may improve the rate and quality of separations achievable by these processes. In this work we have performed protein and small molecule separations with 15 nm thick porous nanocrystalline silicon (pnc-Si) membranes and compared the results to 1- and 3- dimensional models of diffusion through ultrathin membranes. The models predict the amount of resistance contributed by the membrane by using pore characteristics obtained by direct inspection of pnc-Si membranes in transmission electron micrographs. The theoretical results indicate that molecularly thin membranes are expected to enable higher resolution separations at times before equilibrium compared to thicker membranes with the same pore diameters and porosities. We also explored the impact of experimental parameters such as porosity, pore distribution, diffusion time, and chamber size on the sieving characteristics. Experimental results are found to be in good agreement with the theory, and ultrathin membranes are shown to impart little overall resistance to the diffusion of molecules

[†]Adapted from: J.L. Snyder, A. Clark, Jr., D.Z. Fang, T.R. Gaborski, C.C. Striemer, P.M. Fauchet, J.L. McGrath, An experimental and theoretical analysis of molecular separations by diffusion through ultrathin nanoporous membranes, *J. Mem. Sci.* **369**, 119-129 (2011).

smaller than the physical pore size cutoff. The largest molecules tested experience more hindrance than expected from simulations, indicating that factors not incorporated in the models, such as molecule shape, electrostatic repulsion, and adsorption to pore walls, are likely important.

2.2 Introduction

Membranes with nanometer scale pores are an important technology for the separation of proteins and small molecules, with use in research, industrial, and clinical arenas. Dialysis, a diffusion based separation modality requiring a nanoporous membrane, is a staple in laboratory purifications and buffer exchanges. Similarly, the clinical process of hemodialysis utilizes nanoporous membranes for the diffusive separation of proteins coupled with pressurized flow for fluid balance. The development of new membrane materials are needed to improve the precision and efficiency of these frequently used procedures [1, 2].

Many of the polymer based membranes currently used in dialysis have long tortuous pores and log normal pore distributions with extended tails [3], resulting in low resolution molecular weight cutoffs. With pore characteristics such as these, only molecules differing significantly in size can be clearly separated. This is of significant concern to hemodialysis. Low-flux dialysis membranes are able to filter urea and small toxins while retaining serum albumin, but often unwanted middle weight molecules, including β_2 -microglobulin, cytokines, and leptin, are retained as well [4]. Retention of β_2 -microglobulin in particular can cause amyloidosis and can be used as a predictor of patient mortality [5, 6]. High-flux membranes, which have larger pore sizes and cutoffs, are able to better clear middle weight species, but have been linked to serum albumin loss [7, 8].

In addition to having non-ideal pore distributions, traditional dialysis membranes are orders of magnitude thicker than their nominal pore size. The diffusion of molecules

traversing this thickness is greatly reduced compared to free diffusion, requiring long times for laboratory and clinical separations. This has led to a call for thin nanoengineered membranes to enable wearable dialysis units [9]. In the case where filters are used for isolating small analytes, the thickness and tortuous pores present high surface area for adsorption, which may result in the significant loss of low abundance species.

Due to the infrastructure created by the microelectronics industry, silicon is an attractive fabrication platform for engineered nanomembranes [10]. Silicon based membranes with arrays of well defined slit pores fabricated via photolithography techniques have been shown to be useful in a number of separation and biological experiments [11]. Silicon has also been used as a platform for aligned carbon nanotube (CNT) growth and the creation of CNT membranes [12, 13]. However, both of these novel membranes are still many microns thick. In 2004, Tong *et al.* fabricated an ultrathin (10 nm) silicon nitride nanosieve with precise, individually drilled pores, a process that is too time consuming for scale up [14]. More recently, a thin (0.7 - 1 μm) anodized alumina membrane, in which the pores self-assemble, was developed with the use of thin film deposition on silicon, although the pore sizes 0.7-1 μm are not on the same scale as the nanosieve [15].

We have previously reported an ultrathin porous membrane material with self-assembling pores called porous nanocrystalline silicon (pnc-Si) [16]. Previous studies with these membranes have shown diffusion based separations of binary mixtures of proteins [16] and the rapid diffusion of small molecules through the pores [17]. In addition, recent experiments have shown that pnc-Si has high hydraulic permeability [18], can precisely separate closely sized nanoparticles under pressure [18], and can be used as a highly permeable cell culture substrate [19]. Pnc-Si membranes are fabricated using standard photolithography and silicon chip manufacturing techniques. The freestanding membranes can be made between 7 and 30 nm thick, which is on the same order as their pore sizes. Pore sizes can be tuned by adjusting annealing temperature or ramp rate during pnc-Si production, and pore distributions, which are directly measured us-

ing transmission electron microscopy [18], fall within the size scale of small molecules, proteins, and larger complexes. While pnc-Si membranes have a distribution of pores, the membranes have a distinctly sharp cutoff. Current processes enable the production of more than 100 membrane chips per 4" wafer, and this process can be scaled up to a 6", 8", or 12" substrate, which would enable the production of thousands of chips per wafer or whole wafer membrane cartridges for dialysis procedures.

Because of their thinness and unambiguous pore distributions, pnc-Si membranes can be used to test theories of molecular diffusion and can help in understanding how ultrathin membranes can impact diffusive separations. While a porous membrane will prevent any molecule larger than the largest pore from diffusing through, it also hinders the diffusion of molecules smaller than this pore size. Traditional theory suggests that the hindrance is due to 1) steric interactions between the molecule and the pore entrance and 2) frictional interactions between the molecule and the pore walls as it passes through [20]. This theory has seen experimental verification with experiments using track etched mica [21] and porous alumina membranes [22]. Early hindrance models considered the diffusion solely along the central axis of the pore [20, 23, 24], although newer treatments average the hindrance radially across the entire cross-section [25]. An additional cause of hindrance arises from the parallel diffusion of molecules across the membrane surface between pores [17, 27]. The parallel diffusion and entrance effects are negligible for a thick membrane but significantly contribute to the total resistance of an ultrathin membrane; once a molecule finds a pore it needs only to diffuse a distance on the order of its own length to exit the other side.

In this work we have performed separations with proteins and small molecules using pnc-Si membranes. Using equations defining the resistance to diffusion along the surface of and through a membrane, we have developed 1-dimensional and 3-dimensional models of molecular diffusion. We used these models to analyze the influence of factors such as membrane thickness, porosity, pore size distribution, time of separations, and system geometry on separations. The experimental results were compared with the diffusion

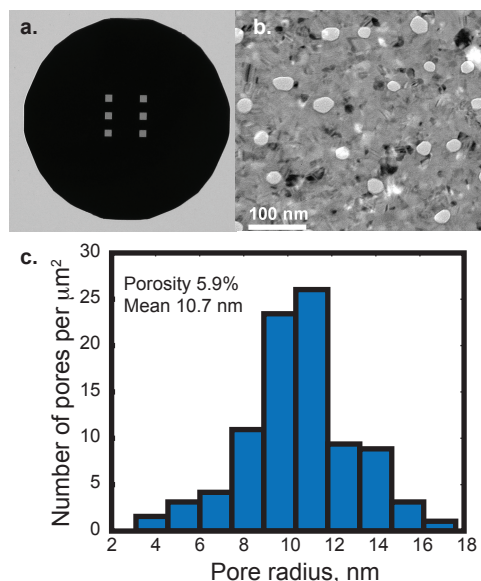


Figure 2.1: Pnc-Si membrane. **a.** 6.5 mm diameter silicon chip with six $0.2 \times 0.2 \mu\text{m}$ freestanding pnc-Si membrane material. **b.** TEM micrograph of nanometer scale pores in 15 nm thick pnc-Si membrane film. Pores are white ellipsoids and nanocrystals are black spots. **c.** Pore characteristics as determined from image processing of $2 \mu\text{m}$ squared micrograph of the membrane in panel **b**.

models, and good agreement was observed for small molecules. We consider the effect of protein adsorption, and we discuss the potential effects of additional factors including molecular shape, electrostatics, and convection.

2.3 Experimental

2.3.1 Pnc-Si Membrane Fabrication and Characterization

Detachable chips with 15 nm thick freestanding pnc-Si membranes were fabricated on $200 \mu\text{m}$ thick 4" silicon wafers according to Striemer *et. al.* [16]. 6.5 mm diameter circular chips with six $0.2 \times 0.2 \text{ mm}$ windows of freestanding pnc-Si membranes were prepared for the experimental separations (Fig 2.1a). Pore characterization was performed using transmission electron microscopy (TEM) on 3 mm diameter chips, which are smaller in diameter so as to fit into the TEM sample holder. Each TEM chip had

four 0.1 x 0.1 mm windows of freestanding pnc-Si membranes. The wafers were annealed in a rapid thermal processing unit at 1000 °C for 60 s with a ramp rate of 100 °C/s.

A Hitachi H-7650 transmission electron microscope was used to view the TEM formatted chips in bright-field mode at 80 kV. Micrographs were taken with an Olympus Cantega 11 megapixel digital camera at a resolution of 100 kX. The TEM micrograph in Fig. 2.1b shows white open pores and black diffracting nanocrystals within the gray crystallized film. Pore characteristics were determined from TEM micrographs using a MATLAB based image processing program developed by our group (available at: <http://nanomembranes.org/resources/software/>) (Fig. 2.1c). A trained operator can use the program to find pore edges and thereby determine the shape and dimensions of pores and the porosity [18].

2.3.2 Protein and Small Molecule Separations

We set up an experimental system that enabled the separations of several proteins and small molecules. The experimental chips from *Section 2.1* were sealed into polypropylene tubes (SiMPore Inc., West Henrietta, NY) between a viton o-ring and polypropylene retention ring (Fig. 2.2a). The polypropylene tube held the fluid wells in contact with the ultrathin membrane, and the retentate and dialysate were removed at the completion of the diffusion experiment.

A series of differently sized proteins and small molecules were prepared for separation experiments. β -galactosidase, phosphorylase b, bovine serum albumin, ovalbumin, and carbonic anhydrase (Sigma-Aldrich, St. Louis, MO) were dissolved 100 mM KCl at a 1 mg/mL concentration. Myosin (Sigma) was used as an intact membrane control, as it is too large to pass through the nanopores. Rhodamine 6g and hydrogen peroxide were prepared at 100 μ M in 100 mM KCl. For each protein or small molecule being tested, 20 μ L of the sample was pipetted onto the retentate side of the membrane and 20 μ L of 100 mM KCl was pipetted onto the dialysate side. Membranes selected for the experiments had pore characteristics as indicated by Fig. 2.1c (Porosity 5.9%, Mean

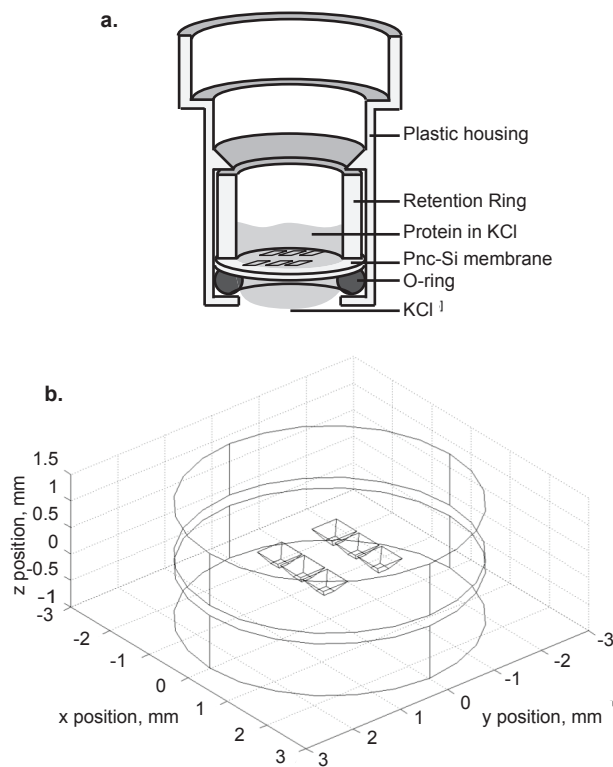


Figure 2.2: Experimental setup and 3-D computational diffusion model. a. Schematic of experimental setup. **b.** CAD model of experimental system: 6 windows terminated in 15 nm thick membrane material separate two fluid wells.

pore radius 10.7 nm). Diffusion was allowed to occur for 24 and 48 hour time points in a sealed container to prevent evaporation.

The retentate and dialysate samples were collected at the completion of the experiment. The protein samples were analyzed using SDS polyacrylamide gel electrophoresis (SDS-PAGE). The hydrogen peroxide was measured using the Amplex Red hydrogen peroxide kit (Invitrogen, Carlsbad, CA) which produces a colored substrate. Absorbance scans of cytochrome c, rhodamine 6g, and Amplex Red assay were taken using an Infinite M200 plate reader (Tecan, Mannedorf, Switzerland). The dimensions of the proteins and small molecules were obtained from literature and from dynamic light scattering measurements using a Zetasizer (Malvern, Worchestershire, UK).

2.4 Theory

2.4.1 1-D Analytical Model

We first developed a simple 1-dimensional model comprised of two fluid wells of length a , separated by a membrane with thickness d to understand dialytic separations with ultrathin membranes (Fig 2.5a). The retentate well, so named as it will contain molecules retained by the membrane at the completion of the simulation, is given an initial homogeneous concentration of molecules. Over the course of the simulation, molecules able to diffuse through the pores will enter the dialysate well. The diffusion of species is governed by Fick's Second Law of diffusion,

$$\frac{\partial c}{\partial t} = D \frac{\partial^2 c}{\partial x^2}, \quad (2.4.1)$$

where c is the concentration, t the time, D the diffusion coefficient, and x the position within the model. In each fluid well, the diffusing species have a free diffusion coefficient

as defined by the Stokes-Einstein relation,

$$D_0 = \frac{k_b T}{6\pi\mu R_s}, \quad (2.4.2)$$

where k_b is Boltzmann's constant, T the temperature, μ the viscosity, and R_s the molecule radius. Diffusion through the membrane is characterized with a reduced diffusion coefficient D_m , where D_m is a function of both molecule and pore sizes (see below).

As the fluid wells are several orders of magnitude longer than the membrane is thick, we can assume the membrane is in a quasi-steady state and that the concentration profile in this region is linear [28]. This means that at a point x within the membrane, the concentration will be given by

$$c(x, t) = c(a, t) - (x - a) \frac{c(a, t) - c(a + d, t)}{d}. \quad (2.4.3)$$

The flux within the membrane, J_m can then be written as

$$J_m = -D_m \frac{\partial c}{\partial x} = D_m \frac{c(a, t) - c(a + d, t)}{d}. \quad (2.4.4)$$

If we neglect molecular adsorption to the membrane, the flux within the membrane, Eq. (2.4.4), is equal to the flux entering from or leaving the membrane to the fluid wells, J_f ,

$$J_f = -D_0 \frac{\partial c}{\partial x} \Big|_{x=a} = -D_0 \frac{\partial c}{\partial x} \Big|_{x=a+d} = J_m. \quad (2.4.5)$$

We use Eq. (2.4.3, 2.4.4, 2.4.5) to form the following jump condition describing the change in concentration across the membrane,

$$c(a + d, t) - c(a, t) = -\frac{J_f d}{D_m} = \frac{D_0 d}{D_m} \frac{\partial c}{\partial x}. \quad (2.4.6)$$

We will treat the membrane at position a as an infinitely thin discontinuity in con-

centration, although the membrane thickness d is necessary in the calculation of the concentration jump condition.

To develop a non-dimensional statement of diffusion between the two compartments, we first introduce the parameter β ,

$$\beta = \frac{D_0 d}{D_m a}, \quad (2.4.7)$$

as a ratio of membrane resistance, Ω_m to well resistance, Ω_w , or

$$\beta = \frac{\frac{d}{D_m}}{\frac{a}{D_0}} = \frac{\Omega_m}{\Omega_w}. \quad (2.4.8)$$

We also introduce the following scaled forms of our variables:

$$\hat{x} = \frac{x}{a}, \quad \hat{t} = \frac{t D_0}{a^2}, \quad \hat{c} = \frac{c - C_2}{C_1 - C_2}, \quad (2.4.9)$$

where C_1 is the initial concentration of the molecule to be simulated in the retentate and C_2 the initial concentration in the dialysate. The final non-dimensional problem is:

$$\frac{\partial \hat{c}}{\partial \hat{t}} = \frac{\partial^2 \hat{c}}{\partial \hat{x}^2}, \quad 0 \leq \hat{x} < 1 \text{ and } 1 < \hat{x} \leq 2, \quad (2.4.10)$$

$$\frac{\partial \hat{c}}{\partial \hat{x}}(0, \hat{t}) = 0, \quad \frac{\partial \hat{c}}{\partial \hat{x}}(2, \hat{t}) = 0, \quad (2.4.11)$$

$$\hat{c}(1+, \hat{t}) - \hat{c}(1-, \hat{t}) = \beta \frac{\partial \hat{c}}{\partial \hat{x}}(1\pm, \hat{t}), \quad (2.4.12)$$

$$\frac{\partial \hat{c}}{\partial \hat{t}}(1+, \hat{t}) - \frac{\partial \hat{c}}{\partial \hat{t}}(1-, \hat{t}) = 0, \quad (2.4.13)$$

$$\hat{c}(\hat{x}, 0) = \begin{cases} 1 & 0 \leq \hat{x} < 1 \\ 0 & 1 < \hat{x} \leq 2. \end{cases} \quad (2.4.14)$$

Eq. (2.4.10) is a dimensionless statement of Fick's Second Law, which holds for the entire system except for the discontinuity at the membrane. Eq. (2.4.11) represents the requirement for no outward flux at the ends of the model. Eq. (2.4.12) is a non-dimensional form of Eq.(2.4.6) that incorporates the idea of a discontinuity at the mem-

brane. Eq. (2.4.13) ensures the continuity of flux entering and leaving the membrane within the fluid well portion of the model. Eq. (2.4.14) is the initial concentration condition, which give the retentate and dialysate non-dimensional concentrations of 1 and 0 respectively.

The solution to this problem is (see Appendix A):

$$\hat{c}(\hat{x}, \hat{t}) = \frac{1}{2} + \sum_{n=1}^{\infty} \frac{\sin \lambda_n}{\lambda_n + \cos \lambda_n \sin \lambda_n} \psi_n(\hat{x}) e^{-\lambda_n^2 \hat{t}}, \quad (2.4.15)$$

where the eigenfunctions ψ_n are given by

$$\psi_n(\hat{x}) = \begin{cases} \cos \lambda_n \hat{x} & 0 \leq \hat{x} < 1 \\ -\cos \lambda_n (2 - \hat{x}) & 1 < \hat{x} \leq 2, \end{cases} \quad (2.4.16)$$

and the eigenvalues λ_n are found by solving the following transcendental equation,

$$\tan \lambda_n = \frac{2}{\beta \lambda_n}. \quad (2.4.17)$$

For comparison purposes, we have also found an analytic solution for diffusion in an identical system lacking a membrane (Appendix B).

2.4.2 Defining Membrane Resistance

Membrane characteristics, including thickness, porosity, and pore distribution, can be directly incorporated into the analytical solution through the parameter β . In this manner, we can test the resistance imparted by specific membranes on a range of molecule sizes. We will consider the membrane resistance to be from two sources: 1) pore discovery via diffusion to the pore entrance [17, 29] and 2) the steric and frictional hindrance as a molecule enters and passes through a pore [20, 23, 24, 25].

It has been shown that small molecules encounter negligible hindrance as they diffuse across an ultrathin membrane [17]. The limiting factor for the permeation of these

molecules is locating and diffusing to a pore, as pore to pore distances are often greater than the membrane thickness. By modifying an expression for the trapping rate of molecules to an adsorbing patch on a surface [29], Kim *et al.* developed a simple expression for the permeability, k_p , of a small molecule through a membrane,

$$k_p = 2D_0NR_P, \quad (2.4.18)$$

where N is the density of pores and R_p is the average pore radius [17]. As this expression neglects steric or frictional hindrances within the pore, we can consider it to be a statement of the pore discovery permeability, P_d . We can rewrite Eq. (2.4.18) given the pore distributions of pnc-Si membranes as

$$P_d = \frac{2D_0}{A_{Im}} \sum_i R_{pi} \quad (2.4.19)$$

where i is the index over every pore in the distribution as determined by TEM image processing, A_{Im} the processed area of the TEM images, and R_p the particular pore radius.

As the size of the molecule increases relative to the pore sizes, so do the effects of steric and frictional hindrance. We use a cross sectionally averaged hindrance equation to determine the reduced diffusion coefficient D_m ,

$$\begin{aligned} \frac{D_m}{D_0} = & 1 + \frac{9}{8}\lambda \ln \lambda - 1.56034\lambda + 0.528155\lambda^2 + \\ & 1.91521\lambda^3 - 2.81903\lambda^4 + 0.270788\lambda^5 + \\ & 1.1015\lambda^6 - 0.435933\lambda^7 \end{aligned} \quad (2.4.20)$$

where λ is the ratio of molecule radius to pore radius (R_s/R_p) [25]. We can determine the transmembrane permeability, P_t , by summing the diffusion coefficients weighed by

the contribution of each pore to the porosity,

$$P_t = \frac{1}{A_{Im}d} \sum_i D_{mi} \pi R_{pi}^2. \quad (2.4.21)$$

Both the pore discovery and transmembrane permeabilities are functions of the molecule size and membrane characteristics and are independent of the concentration difference.

The membrane resistance, Ω_m , or reciprocal of the total permeability, can be obtained by adding the permeabilities like conductances in series [26],

$$\Omega_m = \frac{1}{\frac{1}{P_d} + \frac{1}{P_t}} \quad (2.4.22)$$

The membrane resistance can then be inserted into Eq. (2.4.7) to obtain the ratio of resistances β .

2.4.3 3-D Computational Model

While the 1-D analytic model provides the most basic description of diffusion through an ultrathin membrane and allows simple analysis of the physics of this process, it is not readily comparable with our experiments due to the 3-D geometry of our device. To make this comparison, we have created a 3-dimensional model using the transient diffusion module of COMSOL Multiphysics (COMSOL, Stockholm, SWE). A CAD representation consistent with our experimental system, retentate and dialysate wells separated by a membrane of specific thickness and active area, was built in COMSOL (Fig. 2.2b). Simulated molecules were given diffusion coefficients according to Eq. (2.4.2). We determined the total permeability of the membrane from pore distributions, Eq. (2.4.22), and multiplied it by the membrane thickness to obtain a membrane diffusion coefficient, which was given to the membrane material in the 3-D model.

The model was meshed by creating a swept mesh through the membrane region by connecting “Extremely Fine” predefined meshes in the wells. The larger fluid wells were then re-meshed with a “Finer” predefined mesh. An initial concentration was

specified for the retentate well at time 0, and diffusion was simulated for 24 and 48 hours. The concentration of the molecule tested was integrated throughout the retentate and dialysate wells, and a ratio was taken to obtain the sieving coefficients, Eq. (2.5.1). Batch processing for multiple molecules was performed using MATLAB (The MathWorks, Natick, MA).

2.5 Results and Discussion

2.5.1 Protein and Small Molecule Separations

In Fig. 2.3a we show representative SDS-PAGE results of a 24 hours separation of myosin, β -galactosidase, phosphorylase b, albumin, ovalbumin, and carbonic anhydrase using pnc-Si membranes. The smaller proteins diffuse into the dialysate, while the largest remain within the retentate only. Mass balances show that little protein is adsorbed in this system, and the sum of retentate and dialysate band intensities add up to the starting solution (Fig. 2.3b). Adsorption in our system can occur on the plastic housing or surface of the membrane, but membrane internal area is low compared to conventional membranes ($0.01\mu\text{m}^2$ instead of $100\mu\text{m}^2$ of internal surface area per μm^2 of frontal surface) [18]. We also obtained absorbance scans of retentate and dialysate wells for separations of colored species, as demonstrated for rhodamine 6g in Fig 2.3c.

We use a ratio of dialysate to retentate concentrations,

$$S = \frac{C_{\text{dialysate}}}{C_{\text{retentate}}}, \quad (2.5.1)$$

to track the extent of molecular diffusion within the system. We refer to S as a sieving coefficient because of its similarity in definition and use to the sieving coefficient used in convective transport based separations [30]. While sieving coefficients are not normally used to describe diffusion based systems, we find that such a measure is of use in the visualization of separations in our experiments and model. At equilibrium, both

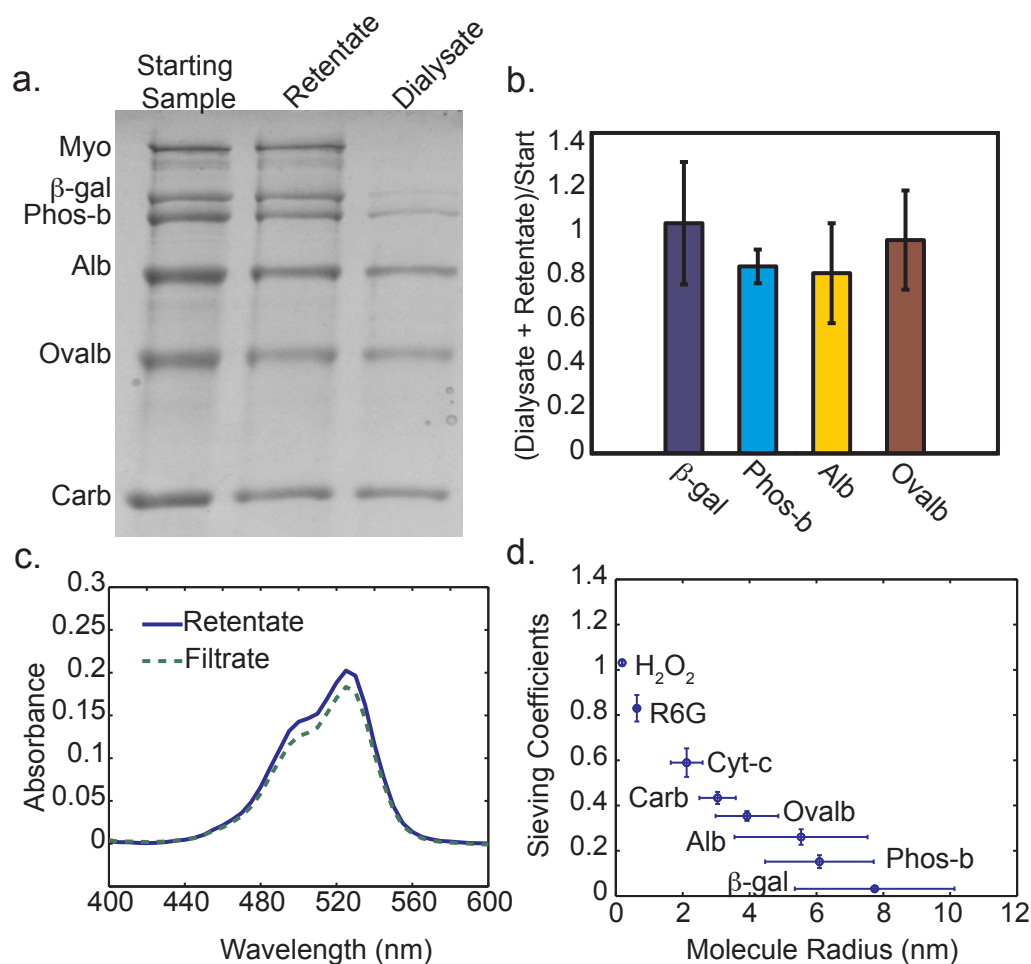


Figure 2.3: Experimental Results. **a.** SDS-PAGE of 24 hour protein separation. As proteins get smaller in size, they diffuse through the membrane to a greater extent. Myosin serves as an intact membrane control. **b.** Mass balance performed by normalizing retentate and dialysate SDS-PAGE gel band intensity to band intensity of starting sample. **c.** Absorbance scans of rhodamine 6g 24 hour diffusion. **d.** Sieving coefficients from experimental proteins and small molecules for a 24 hour separation with molecule sizes determined by DLS (Myo - myosin, β -gal - β -galactosidase, Phos-b - phosphorylase-b, Alb - albumin, Ovalb - ovalbumin, Carb - carbonic anhydrase, Cyt-c - cytochrome c, R6G - rhodamine 6g).

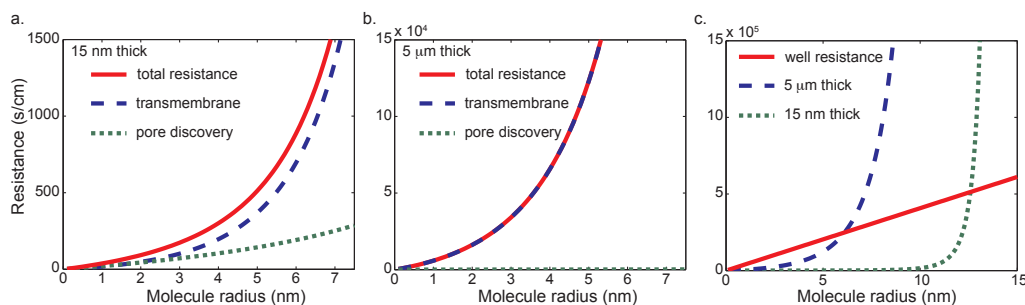


Figure 2.4: Components of resistance for thin and thick membranes with 15 nm pores and comparison to fluid well resistance. **a.** Resistances for an ultrathin (15 nm) membrane. For small molecules, the transmembrane and pore discovery resistances are similar. The addition of the two create a larger total resistance. At molecule sizes approaching the pore size, the transmembrane permeability dominates the total resistance. **b.** Resistances for a thick (5 μm) membrane. Transmembrane resistance is the dominating resistance for all molecule sizes and overlaps with the total resistance in this panel. The pore discovery resistance has the same values as in panel a., though is too small in comparison to be viewed. **c.** Comparison of well resistance and membrane resistance for thick and ultrathin membranes. Due to the high transmembrane resistance in thick membranes, the total membrane resistance surpasses the fluid well resistance at much smaller molecule sizes than the ultrathin membrane case.

dialysate and retentate would have the same concentration and S is equal to 1. Since intensity is proportional to concentration, we can determine S for the protein samples by taking a ratio of dialysate to retentate band intensities from the images of the SDS-PAGE gels using ImageJ [31]. S for colored species was taken as the ratio of peak absorbance of the dialysate to the retentate. In Fig. 2.3d we show sieving coefficients for a 24 hour diffusion experiment plotted against sizes as obtained by literature and dynamic light scattering measurements (Table 2.3).

2.5.2 Resistance Components

The diffusion models were used to better understand the factors, such as membrane resistance, which influence molecular passage in our experiments. In our models, we consider the membrane resistance to be the combination of two separate resistances, the pore discovery ($1/P_d$) and transmembrane ($1/P_t$) resistances. The characteristics

of the membrane greatly affect the contributions of each of these terms. In Fig. 2.4a we show the pore discovery resistance, transmembrane resistance, and the sum of these resistances for a 15 nm thin membrane with the pore characteristics the pnc-Si membranes used in the experiments (Fig. 2.1c). In an ultrathin membrane, the pore discovery resistance is on the same order or sometimes even greater than the transmembrane resistance for molecules much smaller than the physical pore cutoff. Steric and frictional hindrances within the membrane are minimal for small molecules, but since the distance between pores is similar to the distance through the pores, the pore discovery resistance can be significant and in some cases even dominant (see Supplement). For larger molecules, the transmembrane resistance outweighs the pore discovery resistance and eventually becomes infinite for molecules as large as or larger than the pores.

In thick membranes with the same pore characteristics of a pnc-Si membrane, the transmembrane resistance dominates for all molecule sizes (Fig. 2.4b). The numerical value of the total resistance in thick membranes is also much higher than ultrathin membranes. A comparison can be made between total membrane resistances and the resistance to diffusion within the fluid wells (a/D_0) (Fig. 2.4c). The total resistance for thick membranes surpasses the well resistance at smaller molecule sizes than for ultrathin membrane, even though both membranes have the same pore radii and porosity.

2.5.3 Visualizing Membrane Resistance

The 1-D analytical model removes geometric complexity and reduces the problem to the basic physics of separation. This enables simple visualization and analysis of the theoretical separations. In Fig. 2.5 we compare results for the diffusion of a 5 nm radius molecule with no membrane, an ultrathin membrane (15 nm), and a thick membrane (5 μm). Both membranes were given pore distributions from the pnc-Si membrane in Fig. 2.1c. The separations depicted in Fig. 2.5 are for a system with 1 mm fluid wells at 0, 100, 1000, and 10,000 seconds.

The concentration profiles of the free diffusion (Fig. 2.5b) and ultrathin membrane

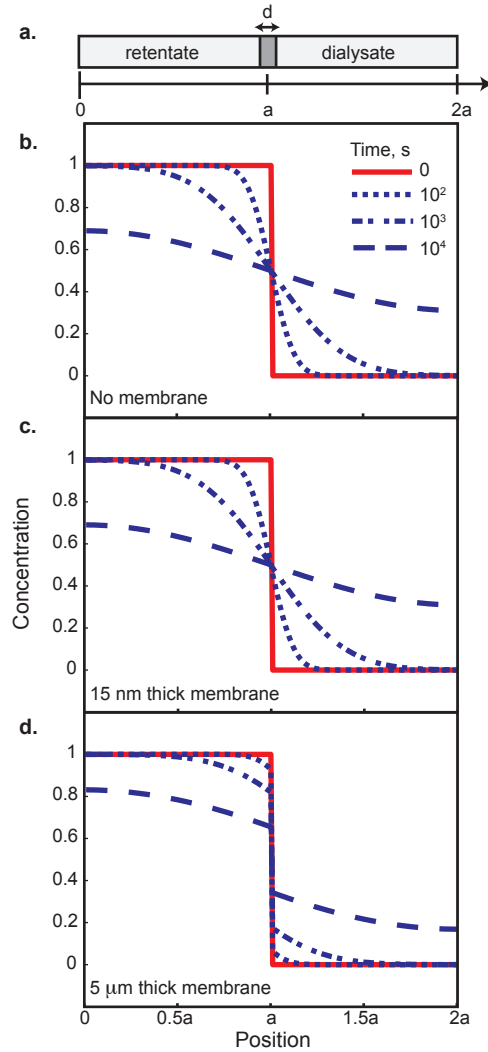


Figure 2.5: Concentration profiles in 1-D model. **a.** Schematic of 1-D analytic model: retentate and dialysate fluid wells are separated by a membrane of thickness d . **b.** In a simulation without a membrane, a 5 nm radius molecule diffuses into the dialysate well ($a = 1$ mm) based on its free diffusion coefficient. **c.** In the case of an ultrathin (15 nm thick) membrane, in which the 5 nm radius molecule is significantly smaller than the largest pores in the distribution (Fig. 2.1c), the diffusion is indistinguishable from the no membrane case. **d.** If a thick (5 μm) membrane with the same pore radii and porosity separate the wells, the diffusion is hindered, as indicated by the large concentration jump across the membrane and the slower approach to equilibrium.

(Fig. 2.5c) simulations are identical, indicating that a 5 nm radius molecule experiences negligible hindrance from the molecularly thin membrane under these conditions. While there is resistance from the ultrathin membrane, a molecule only experiences this hindrance over a distance similar to its own size, and so the transport time is negligible compared to bulk transport.

A 5 μm thick membrane with the same pore characteristics as the 15 nm thick membrane has a 300x larger β , Eq. (2.4.7), for a separation with a 5 nm radius molecule. The concentration profiles for this case (Fig. 2.5d) demonstrate an obvious concentration jump across the membrane. The higher resistance slows the diffusion of the molecules through the membrane and increases the time required for the system to reach equilibrium.

2.5.4 Sieving by Thin and Thick Membranes

To visualize separations over an entire range of molecule sizes, we use the 1-D model to generate sieving coefficients, Eq. (2.5.1), over time. To simplify the analysis, we have used a monodisperse, 10 nm radius pore distribution. The sieving coefficients for molecule radii ranging from 0.5 to 12 nm and times of 1, 6, and 24 hours using both 15 nm and 5 μm thick membranes are shown in Fig. 2.6. Again, we have included a free diffusion case for comparison. A sieving coefficient of 1 indicates that the system has reached equilibrium.

We observe that diffusion through ultrathin membranes follows the free diffusion curve until the molecule size is within $\sim 30\%$ of the physical pore cutoff for short times and $\sim 10\%$ for long times. The steepness of the sieving profile near the cutoff indicates that high resolution separations are possible with molecularly thin membranes and that the resolution improves as equilibrium is approached. In contrast, separations with thick membranes lag behind the free diffusion curves at all times. Even the diffusion of the smallest molecules through thick membranes is slowed by the 10 nm radius pores. The hindrance is higher for molecules in the thicker membrane because of the length of

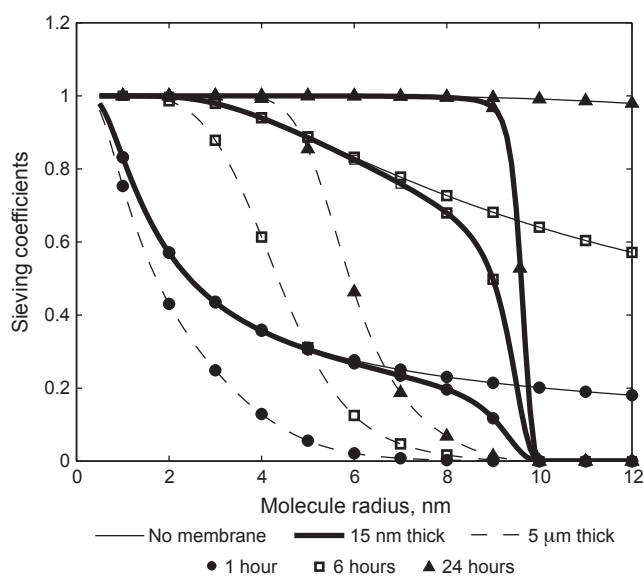


Figure 2.6: Sieving profiles of 15 nm thick and 5 μm thick membranes for 1, 6, and 24 hour time points. Both 15 nm and 5 μm thick membranes have a pore radius cutoff of 10 nm. A no membrane (free diffusion) simulation at each time point is shown for comparison. For small molecules, the diffusion through the thin membrane is indistinguishable from free diffusion. Diffusion through the thin membrane slows as the molecules approach the pore cutoff. The thick membrane shows strong hindrance at all molecule sizes, raising the time to equilibrium and lowering the resolution of the separation.

the pores they must diffuse through, and this lowers the resolution of the separation at any time. Thus molecularly thin membranes are expected to fractionate mixtures based on size more quickly and have a higher resolution cutoff than their thick counterparts at any time before equilibrium is reached.

2.5.5 Factors that Influence Membrane Separations

In addition to membrane thickness, several other factors can affect the performance of membranes in dialysis, including 1) porosity, 2) pore size distributions, 3) time of separations, and 4) well geometry. Understanding the impact of these factors is important for the optimization of experimental separations. We can visualize the effect of these factors by normalizing sieving coefficients, S_{mem} , to those from a membraneless separation, S_0 . The ratio S_{mem}/S_0 deviates from 1 as membrane resistance slows transport relative to free diffusion. A curve generated by taking this ratio for a range of molecule sizes will be referred to as a normalized sieving profile. In the panels of Fig. 2.7 we examine the effects of porosity (Fig. 2.7a), pore size distributions (Fig. 2.7b), time (Fig. 2.7c), and well geometry (Fig. 2.7d) on the normalized sieving profile. A dotted line indicates the projected equilibrium at infinitely long times.

We first investigated the influence of porosity on separations (Fig. 2.7a). The results show that as the porosity of an ultrathin membrane decreases, the effective cut-off and sieving resolution of the membrane both decrease at a particular time point. Recalling that the resolution improves as equilibrium is approached, we see that the lower porosity diminishes resolution by directly increasing both pore discovery and transmembrane resistances and slowing transport. A thick (5 μm) membrane with 5% porosity is shown for comparison. Note that even with 10x lower porosity than a thick membrane, an ultrathin membrane exhibits sharper resolution separations at the same time point.

Next we inspected the contribution of different pore sizes on separations with ultrathin membranes (Fig. 2.7b). To perform this analysis, porosity was kept constant at 5%, and we simulated membranes with 5 nm radius pores (636 pores/ μm^2) and 10

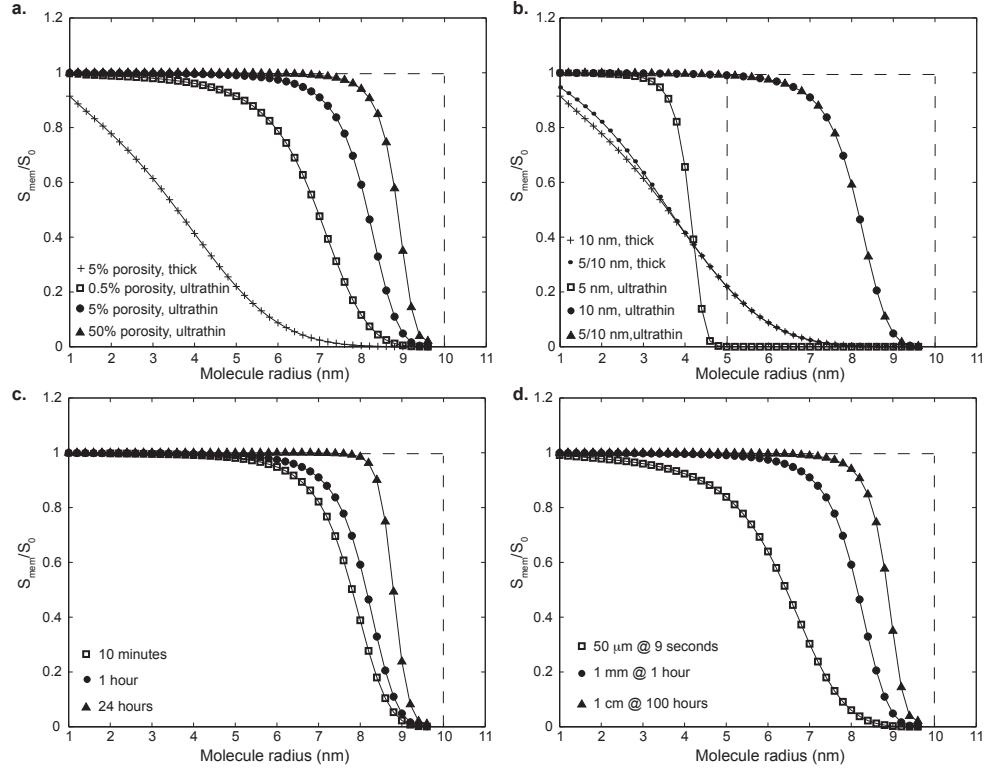


Figure 2.7: Factors that influence separations by ultrathin membranes. Here we plot sieving coefficients normalized to sieving coefficients obtain from a membraneless separation (free diffusion case), S_{mem}/S_0 , for a series of molecule sizes. This normalized sieving profile shows the extent to which hindrance by the membrane influences the separations. Except for the particular factor being adjusted, the separations are for a 15 nm thick membrane with 5% porosity and 10 nm radius pores for a 1 hour separation in a system with 1 mm fluid wells. The dotted line represents equilibrium (time > 100 days). **a.** Lowering porosity increases the influence of the membrane on molecules below the 10 nm cutoff. A 5 μ m thick membrane is included for comparison. **b.** Small pores do not change the normalized sieving profile for 15 nm thick membranes. Adding more small pores to a thick membrane has some effect on the sieving profile. Separations with thin membranes are thus governed by the pores close to the physical pore cutoff, while the entire distribution of the membrane affects the separations for thick membrane. **c.** The membrane has a greater affect on the normalized sieving profile at shorter time scales. This occurs because slight hindrance differences are significant at short times. **d.** Smaller wells reach equilibrium faster but are more sensitive to the membrane. Profiles are shown in each case at a characteristic time to equilibrium $0.4\tau_{eq}$, where $\tau_{eq} = a^2/D_0$.

nm radius pores (159 pores/ μm^2). The 10 nm radius pore membrane exhibits a sharp drop in the normalized sieving profile near the 10 nm cutoff, and a similar 5 nm cut-off is visible for the 5 nm radius pore membrane. If we add the pore distributions of these membranes together and simulate a 5 and 10 nm radius pore membrane with 10% porosity, we see a normalized sieving profile similar in appearance to the original 10 nm radius pore membrane. This illustrates that pores significantly below the physical pore cutoff do not contribute to the separation even though they increase the overall membrane porosity. In the case of the thick membrane, the addition of the 5 nm radius pores does effect the normalized sieving profile for the smallest molecules. Although the effect on the sieving profile is slight, it serves to illustrate that thicker membranes are more sensitive to pore sizes below the cut-off than an ultrathin membrane.

We then examined the effect of time on the normalized sieving profiles (Fig. 2.7c). As we saw for non-normalized sieving curves (Fig. 2.6), shorter times are associated with smaller effective cut-offs and lower resolution. This is because small size differences between molecules can result in significant hindrance differences at short times. The non-equilibrium profiles are not only relevant for short duration experiments, but they can represent the steady-state profiles in a device where a constant concentration jump is maintained across the membrane by the supply and removal of species. Our results suggest that diffusion in such a situation would deviate from free diffusion for molecules within $\sim 30\%$ of the pore size cut-off.

The final factor we have chosen to investigate is the geometry of the experimental system. Separations in longer fluid wells will have a larger equilibrium time constant, τ_{eq} ,

$$\tau_{eq} = \frac{a^2}{D_0}, \quad (2.5.2)$$

and in Fig. 2.7d we show simulations at $0.4 \tau_{eq}$ for several geometries (Fig. 2.5d). Specifically, we compare our standard 1 mm well at 1 hour to a 1 cm well at 100 hours and a 50 μm well at 1/400th of an hour (9 seconds). Even though each system has

evolved the same degree toward equilibrium and uses the same membrane, the cut-off and resolution are clearly lower for the smaller geometry. This occurs because the wells become smaller and the transfer time across the membrane becomes a more significant fraction of the diffusion through the entire system, and thus the membrane has a greater resistance relative to the bulk resistance. The 50 μm separation is of particular interest because this form factor could be realized in the development of microfluidic separation devices or bioreactors.

Our results should help guide the design of devices and conditions that achieve separations by diffusion through ultrathin membranes. In comparison to conventional thick membranes, ultrathin membranes will reach equilibrium faster and will enable higher resolution separations at time points far from equilibrium. As separations are carried out for longer times, the resolution of the separation will improve and the molecular cutoff will occur at a size similar to the largest pore size. The yield and purity of both the retentate and dialysate species will also improve with time. At times far from equilibrium, the resolution of separations with ultrathin membranes remains high but has a smaller effective cutoff. Thus there is an opportunity to purify species well below the absolute cutoff, although with lower yield than an optimized process. These short duration separations, will require simulations to anticipate the cutoff, resolution, purity, and yield. One important determinant of the quality of separation is the geometry of the diffusion chamber. While smaller volumes approach equilibrium quicker, the relative contribution of membrane resistance is higher and thus the benefit of smaller systems does not increase in direct proportion to the reduced size.

2.5.6 Comparison to Experiments

Simulations with the 3-D model reveal a high sensitivity to system geometry. A slice through the 3-D model after 10 hours of diffusion of a 5 nm radius molecule shows significant depletion directly above the membrane windows but shallow gradients elsewhere, illustrating slow lateral diffusion in the bulk. (Fig. 2.8). Thus the timescale for lateral

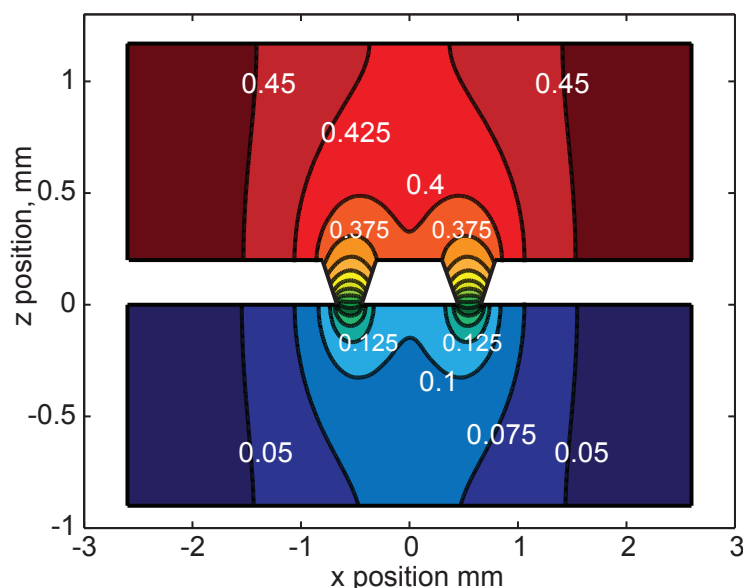


Figure 2.8: Slice through 3-D model after 10 hours of diffusion of a 5 nm radius molecule. Concentration isolines show diffusion through the membrane (at z position 0) from the retentate (top) to the dialysate (bottom).

diffusion in the bulk will be a major determinant of the time to equilibrium because of the limited degree to which the membranes span the cross section of the chambers. The retentate and dialysate samples were completely homogenized during collection, and so we compare simulations to experiments by integrating the simulated retentate and dialysate wells to compute average concentrations.

In Fig. 2.9, we compare 3-D simulations to diffusion experiments at 24 and 48 hours. At both time points, the experimental separations follow the sieving profile predicted from the pore distribution shown in Fig. 2.1c for all but the largest molecules, β -galactosidase and phosphorylase b (Fig 2.9a). These results support the prediction that an ultrathin membrane offers effectively no resistance to small molecules but indicates a greater hindrance than predicted by existing sieving models for molecules larger than 30% of the membrane pore size.

There are several likely explanations for the differences between experiments and theory for large molecules. First we note that any factor that reduces measured pore sizes

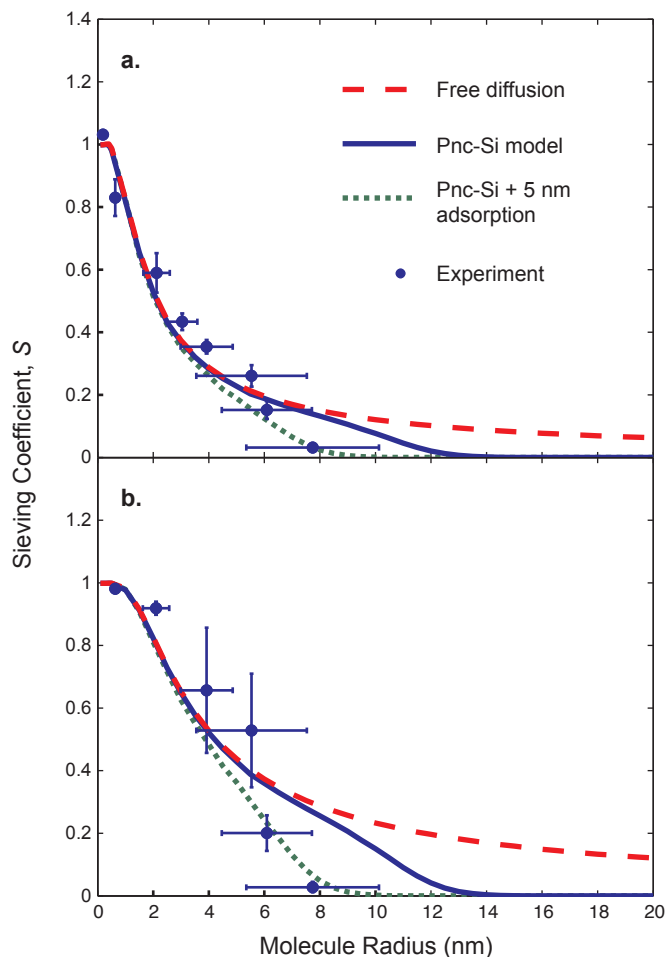


Figure 2.9: Experimental and 3-D model sieving profiles for pnc-Si separations at a. 24 and b. 48 hours using DLS sizing for experimental data. The sieving profile (solid line) deviates from free diffusion (dashed line) near the physical pore size cutoff. The largest molecules deviate from the theoretical sieving profile. We plot at additional simulation with an added 5 nm protein adsorption ring to the pores, and this adjustment fits the data for both 24 and 48 hours.

from those measured in TEM micrographs would slow diffusion relative to predictions. For example, electrostatic repulsion would reduce the effective pore size and increase the transmembrane resistance [32, 33]. Previous experiments with different salt concentrations have shown that electrostatics do influence the diffusion of molecules through the pores [16]. At the salt concentrations in these experiments (100 mM), the Debye length, or distance to $1/e$ dropoff of surface potential, is only ~ 1 nm and so the effect on pore size reduction appears too small to account for the hindrance. A rigorous treatment of electrostatics, such as the analysis by Smith and Deen [34], could be used to create more detailed future models in cases where electrostatic interactions are important.

A second known factor that will reduce pore sizes is protein adsorption to the edges of pores. While adsorption causes negligible sample loss to the membrane (Section 2.5.1), this does not mean that adsorption does not occur. Indeed, we have previously shown that incubation with albumin creates a ~ 3.5 nm thick protein layer on the internal surface of the pore [16], which is consistent with the thickness of an albumin monolayer [35]. The effects of adsorption can be added to the simulation by subtracting the thickness of the adsorption layer from the pore sizes. We simulated several thicknesses of protein coating, and found that a 5 nm layer fit both the 24 and 48 hour data (Fig. 2.9). A 5 nm layer does not impede the diffusion of small molecules, but creates more hindrance for larger molecules. Given that there are several proteins in the system with sizes greater than 5 nm, it is reasonable that a ring of denatured proteins of this size is created. Note that the size and composition of this protein layer is likely to change with time [35].

Another source of potential inaccuracy in our simulations could be found in the hindrance function itself, Eq. (2.4.20). While the theoretical treatments behind this equation establish its validity for $0 \leq \lambda \leq 0.95$, few experiments test hindrance theory for molecules close in size to the pore sizes in cylindrical pores [25]. One practical difficulty with verifying the equations for larger particles is that the passage through long pores is so slow that it can be difficult to measure. In this way ultrathin membranes

provide an opportunity to test long-standing theory about sieving through cylindrical pores more easily than before. Proteins are not an ideal choice for such tests, as the effects of protein adsorption, shape, and flexibility are all important to consider (see Supplement for more comprehensive data on molecular shapes and sizes). Future tests of these sieving models should be done with rigid nanoparticles and a known charge density.

The influence of convection is considered to be minimal due to the low volumes and isolation of the system from thermal gradients and air currents, through gravity and osmosis may cause flow through the membrane. Given a 1 mm pressure head, gravity induced flow through the membrane is at best several nanoliters (see Supplement). While collected volumes in retentate and dialysate are similar to initially pipetted volumes, osmotic pressure calculations indicate that initial volumetric flow rates could fall between 10^{-5} and 10^{-4} $\mu\text{L/s}$, and could lead to the transfer of ~ 2 μL (10% volume change) in an hour at the most (see Supplement). The initial flow rate would decrease over time and may be much lower than calculated as the calculation neglected proteins that can pass through the membrane and the highly mobile ions in the buffer. Fluid entering the retentate by osmosis will slow diffusion to the dialysate due to the convection and reduction of the concentration gradient. Experiments with pure proteins at 1 mg/mL and proteins at a partial concentration of 1 mg/mL within a 5 mg/mL mixture have yielded similar sieving coefficients, indicating that the effects of osmosis in the more concentrated mixtures are minimal.

Interactions between molecules within the pores, a function of the concentration, might also lead to a discrepancy between experiment and theory. However, total protein mixture concentrations are low enough that molecular interactions would not be predicted in the bulk (see Supplement). Interactions between molecules within pores should also be minimal in ultrathin membranes where pore lengths are similar to molecule sizes, as pores are likely to contain only one molecule at a time.

2.6 Conclusions

In this work we have performed experimental molecular separations using ultrathin (15 nm) nanoporous membranes and compared experiments to hindrance theory. Ultrathin membranes present a unique opportunity for high resolution separations not afforded by thick conventional membranes. Our 1-D diffusion model indicates that longer times are required for higher resolution separations, and ultrathin membranes allow separations to reach equilibrium more quickly than their thicker counterparts. Even far from equilibrium, high resolution separations are attainable with ultrathin membranes. In simulated separations with ultrathin membranes, molecules 30% smaller than the largest membrane pores experience essentially no resistance from the membrane and diffuse as if by free diffusion through the barrier. This contrasts to simulations with 5 μm thick membranes which show hindrance and low resolution at all molecule sizes until very long times. A 3-D model that captures the physical geometry of our experimental system compares well to experimental separations. In our experiments, small molecules and small proteins diffuse through the membrane as if by free diffusion, but the largest proteins exhibit lower sieving coefficients than our model predicts suggesting that neglected factors, such as shape, electrostatics, and adsorption can affect the separation characteristics for larger molecules. The discrepancy between theory and experiments is eliminated if we assume a 5 nm absorbed protein layer reduces all pore sizes identified in the membrane histogram. We expect that the models presented here will help guide the design of experiments and devices that use ultrathin membranes for dialysis and molecular separations, although more advanced sieving models will need to be developed and tested to accurately predict the rate of passage of molecules close in size to the largest pores.

2.7 Appendix A

We can solve the problem in equation (9) using separation of variables so that

$$\hat{c}(\hat{x}, \hat{t}) = \psi(\hat{x})T(\hat{t}). \quad (2.7.1)$$

The solution for the temporal component of the concentration, $T(t)$, is

$$T(\hat{t}) = e^{-\lambda^2 \hat{t}} \quad (2.7.2)$$

where λ is a constant. By utilizing the no-flux boundary conditions, Eq. (2.4.11), we can obtain the following statement for $\psi(x)$

$$\psi(\hat{x}) = \begin{cases} A_L \cos \lambda \hat{x}, & 0 \leq \hat{x} < 1 \\ A_R \cos \lambda(2 - \hat{x}), & 1 < \hat{x} \leq 2 \end{cases} \quad (2.7.3)$$

where A_L and A_R are all constants. Flux continuity, Eq. (2.4.13), requires

$$(A_L + A_R) \sin \lambda = 0, \quad (2.7.4)$$

and the concentration jump condition, Eq. (2.4.12), allows us to write

$$(A_L - A_R) \cos \lambda = -\beta A_L \lambda \sin \lambda. \quad (2.7.5)$$

These equations will results in two families of eigenfunctions. The first family is obtained when $\sin \lambda$ in Eq. (2.7.4) is equal to zero. This set of even eigenfunctions have eigenvalues that are integer multiples of π , so that

$$\lambda_n^{(e)} = n\pi, \quad \psi_n^{(e)} = \cos(n\pi\hat{x}) \quad 0 \leq \hat{x} \leq 2. \quad (2.7.6)$$

The second family results when $\sin \lambda$ does not equal zero and instead A_L equals $-A_R$

in Eq. (2.7.4). In this case Eq. (2.7.5) reduces to

$$\tan \lambda_n^{(o)} = \frac{2}{\beta \lambda_n^{(o)}}. \quad (2.7.7)$$

This transcendental equation can be solved to find an infinite number of odd eigenvalues $\lambda_n^{(o)}$ for

$$\psi_n^{(o)} = \begin{cases} \cos \lambda_n^{(o)} \hat{x}, & 0 \leq \hat{x} < 1 \\ -\cos \lambda_n^{(o)} (2 - \hat{x}), & 1 < \hat{x} \leq 2. \end{cases} \quad (2.7.8)$$

The complete solution of the equation is an eigenfunction expansion of the form

$$\hat{c}(\hat{x}, \hat{t}) = c_o + \sum_{n=1}^{\infty} c_n \psi_n(\hat{x}) e^{-\lambda_n^2 \hat{t}} \quad (2.7.9)$$

where the coefficients c_o and c_n are solved for using the initial value, Eq. (2.4.14), and the following relations:

$$c_o = \frac{1}{2} \int_0^2 \hat{c}(\hat{x}, 0) d\hat{x} \quad (2.7.10)$$

$$c_n = \frac{\int_0^2 \hat{c}(\hat{x}, 0) \psi_n(\hat{x}) d\hat{x}}{\int_0^2 \psi_n^2(\hat{x}) d\hat{x}}. \quad (2.7.11)$$

Thus the final solution is

$$\hat{c}(\hat{x}, \hat{t}) = \frac{1}{2} + \sum_{n=1}^{\infty} \frac{\sin \lambda_n}{\lambda_n + \cos \lambda_n \sin \lambda_n} \psi_n(\hat{x}) e^{-\lambda_n^2 \hat{t}}. \quad (2.7.12)$$

It should be noted that all even eigenfunctions, other than the one associated with $\lambda_0^{(e)}$, give zero coefficients. This means that Eq. (2.7.12) requires the odd eigenfunctions given by Eq. (2.7.7) and only the constant first even eigenfunction, c_o .

2.8 Appendix B

An additional 1-D analytical model lacking a membrane, or the free diffusion case, was simulated for comparison purposes. The following problem was scaled using Eq. (2.4.9)

in the text:

$$\frac{\partial \hat{c}}{\partial \hat{t}} = \frac{\partial^2 \hat{c}}{\partial \hat{x}^2}, \quad 0 \leq \hat{x} \leq 2, \quad (2.8.1)$$

$$\frac{\partial \hat{c}}{\partial \hat{x}}(0, \hat{t}) = 0, \quad \frac{\partial \hat{c}}{\partial \hat{x}}(2, \hat{t}) = 0, \quad (2.8.2)$$

$$\hat{c}(\hat{x}, 0) = \begin{cases} 1, & 0 \leq \hat{x} < 1 \\ 0, & 1 < \hat{x} \leq 2 \end{cases} \quad (2.8.3)$$

where Eq. (2.8.1) is Fick's Second Law of Diffusion, (2.8.2) the no flux conditions, and (2.8.3) the initial value. The solution to this problem is:

$$\hat{c}(\hat{x}, \hat{t}) = \frac{1}{2} + \sum_{n=1}^{\infty} \frac{\sin \lambda_n}{\lambda_n} \cos(\lambda_n \hat{x}) e^{-\lambda_n^2 \hat{t}}, \quad (2.8.4)$$

where

$$\lambda_n = \frac{n\pi}{2}. \quad (2.8.5)$$

2.9 Supplement

2.9.1 Resistances

Diffusion of molecules within a porous membrane is slowed due to the membrane resistance, and in the text we look into the types of resistances in an ultrathin membrane. Resistance, Ω , is the reciprocal of the permeability defined by Fick's Law,

$$J = D_m \frac{dc}{dx} = P \Delta c = \frac{1}{\Omega} \Delta c \quad (2.9.1)$$

where J is the flux, D_m the membrane diffusion coefficient, c the concentration, x the membrane thickness, and P the permeability. These resistances used in the model are: 1) the pore discovery resistance and 2) the transmembrane resistance. The pore discovery resistance describes the diffusion to a pore at the surface of a membrane. The transmembrane resistance is the internal steric and frictional hindrance scaled by the

membrane porosity, and is also the resistance that defines the cutoff of the membrane.

In the case of no steric or frictional hindrance, the the diffusion coefficient within the membrane would equal the free diffusion coefficient, and the transmembrane resistance would be the free diffusion coefficient weighted by the porosity. This simple porosity weighted resistance is on the same order, but generally smaller than the pore discovery resistance. The pore discovery resistance is functionally different from the simple porosity weighted resistance as it is based on the distances between pores on the surface of the membrane.

The pore discovery resistance is only significant for the case of an ultrathin membrane, as the distance between pores is similar to the distance through the pores (Fig. 2.4). In some cases the pore discovery resistance can surpass the transmembrane resistance (Fig. 2.10a). For this to occur, the molecule must be very small in comparison to the pores. When considering the diffusion of very small ions through an ultrathin membrane with large pores, the pore discovery resistance is the only term required (Fig. 2.10b).

2.9.2 Concentration

High concentrations of molecules could create interactions between molecules that reduce their diffusion in solution. In a constrained space such as a pore, any interactions would have an even greater effect on the diffusion within this region. Our model does not take into account reduced diffusion due to interactions at high concentrations, and this would lead to disagreement between the model and experiment at elevated concentration. In this section we evaluate the concentration of our experiments and the extent to which it may affect our model.

Using a simple geometric argument, we can calculate the distance between molecules in one of the separation mixtures used in this study (1 mg/mL of each carbonic anhydrase, ovalbumin, albumin, phosphorylase b, and β -galactosidase at a total concentration of 5 mg/mL). We first find the total number of molecules in 1 L of the

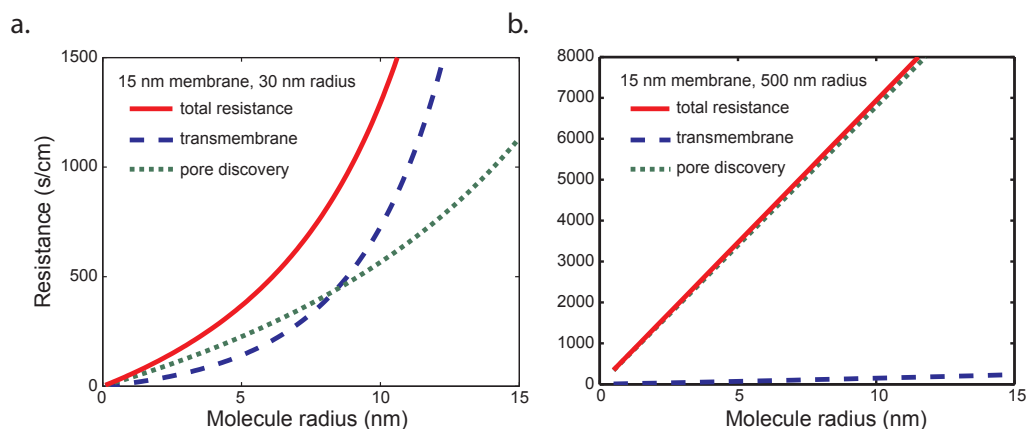


Figure 2.10: Membrane resistance to diffusion **a.** Resistances for a 15 nm thick membrane, with 5% porosity and 30 nm radius pores. The pore discovery resistance is greater than the transmembrane resistance for the smallest molecules. The pore discovery resistance also highly contributes to the total resistance for larger molecules. **b.** Resistances for a 15 nm membrane with 5% porosity and 500 nm radius pores. The pore discovery resistance dominates in this scenario, as there is little steric or frictional hindrance and distance between pores is large.

separation mixture (Table 2.1). The total number of molecules is then divided by 1 L to find the average volume that each molecule occupies, and the cubed root is taken to find the average distance between molecules. For this particular mixture, we find that each molecule is separated on average by 112 nm.

Baltus et al use an equation originally developed by Graessley for the calculation of

Table 2.1: Total number of molecules in the separation mixture.

Molecule	Mol. Mass (g/mol)	Conc. $\times 10^{-6}$ (mol/L)	$\#/L \times 10^{-19}$
carb. anhydrase	37,000	2.0	8.2
ovalbumin	45,000	5.1	3.2
albumin	67,000	1.5	1.1
phosphorylase-b	195,000	2.2	0.74
β -galactosidase	495,000	2.7	0.61
			Sum = 13.9×10^{-19}

Table 2.2: Critical concentrations of proteins as predicted by Graessley equation.

Molecule	R_h	Critical Concentration (mg/mL)
cytochrome c	2.12	222
carbonic anhydrase	3.04	180
ovalbumin	3.92	82.1
albumin	5.54	156
phosphorylase-b	6.09	274
β -galactosidase	7.74	262

a critical concentration in which polymers begin to overlap and interact in free solution,

$$c_{crit} = \frac{1}{8N_A R_g^3}, \quad (2.9.2)$$

where the critical concentration c_{crit} is a molar concentration, N_A Avagadro's number and R_g the molecule's radius of gyration [36, 37]. By this equation, a 40 kDa dextran with an 8 nm radius of gyration would give a critical concentration of ~ 16 mg/mL. In contrast, proteins are much more compact and would be expected to have a much higher critical concentration. As we do not have radius of gyration data for the proteins used in this study, we substitute the hydrodynamic radii, R_h , as obtained from DLS (Table 2.3) and find the minimum critical concentrations (Table 2.1).

The critical concentrations and the estimated distances between molecules are much too high for molecule interaction to have much of an effect on our system. We also note that if there were interactions between molecules, they would be limited within the pnc-Si membrane because of its dimensions. At 15 nm, the pore depth is on the same order as the size of one or two molecule diameters. Interactions between molecules within membrane pores would have a more significant effect on thick membranes.

2.9.3 Osmosis

Another factor that could lead to disagreement between model and experiment is osmotic flow between the retentate and dialysate wells. As the model is solely diffusion based, convective transport of molecules within the experiment would affect the final molecule concentrations within the two wells as well as the final volume in the wells. Here we estimate the expected osmotic flow rates for the experimental concentrations.

We can calculate the osmotic pressure, $\Delta\Pi$, in our system using van't Hoff's equation

$$\Delta\Pi = RT(c_0 - c_L), \quad (2.9.3)$$

where R is the gas constant, T the temperature, and $c_0 - c_L$ the concentration difference of the protein across the membrane. The osmotic pressure can then be used to calculate the volume flux, J_v , through a membrane,

$$J_v = L_p(\Delta P - \sigma_0 \Delta\Pi) \quad (2.9.4)$$

where the hydraulic permeability, L_p is a function of the porosity χ , pore size R_p , fluid viscosity μ , and pore length L [24], or

$$L_p = \frac{\chi r_0^2}{8\mu L}. \quad (2.9.5)$$

ΔP is the hydraulic pressure in the system, and can be set to zero for our experimental setup. σ_0 is the osmotic reflection coefficient, which equals 1 in the case where the protein cannot cross the membrane.

In our experiments, the largest proteins held back by the membrane are 495 kDa, and with a concentration of 1 mg/mL, an osmotic pressure of 5.0 Pa is obtained. Using a pore radius of 10 nm, a porosity of 5%, and a pore length of 15 nm, the volume flux through the membrane is $2.3 \times 10^{-7} \text{ m}^3/(\text{s} \cdot \text{m}^2)$, and given an active membrane area of $2.4 \times 10^{-7} \text{ m}^2$, the volumetric flow is $5.6 \times 10^{-5} \text{ } \mu\text{L/s}$. At a 10 mg/mL concentration the

volumetric flow becomes $5.6 \times 10^{-4} \mu\text{L/s}$.

These volumetric flow rates are the initial flow rates, and as water passes through the membrane, these rates will decrease. Molecules that have reflection coefficients less than one and can pass through the membrane as well as freely diffusing salts will serve to lower these initial rates as well. While there may be some effect of osmosis on the experimental separation, the effects appear to be minor for small molecules as there is good agreement with theory. We have also observed that sieving coefficients are within our measurement error for a particular protein whether it is alone or within a mixture at the same partial concentration.

2.9.4 Gravitational Flow

Gravitational flow is another form of convection that could cause molecule transport in the experimental system. The experiments are set up so that the retentate well is above the dialysate well. Given a height difference of 1 mm, we would expect a gravitational pressure ($\Delta P = \rho_w gh$) of 1×10^{-7} bar. We report flow rates of $23 \text{ cc}/(\text{cm}^2 \cdot \text{min} \cdot \text{bar})$ for deionized water through pnc-Si membranes [18]. Using an active area of $2.4 \times 10^{-7} \text{ m}^2$ and a 24 hour time period, the expected permeation of water is 7.9 nL toward the dialysate well. The effect of gravity on the flow of material through the membrane is thus minimal.

2.9.5 Molecule Sizes

For our comparison of experimental results to our predictive model, we measured the sizes of our experimental molecules using dynamic light scattering (DLS) with a Malvern Zetasizer. In Table 2.3 we show the radii obtained from DLS intensity distributions, where the error is equal to the width of the distribution. While DLS gives us an experimental radius from hydrodynamic data, the algorithm for the radius calculation assumes a spherical colloid. Radii for hydrogen peroxide and rhodamine 6g were calculated using Stokes-Einstein equation and diffusion coefficient data in the indicated references.

To test the effects of shape on diffusion, we also measured the long and short axis radii from x-ray crystallography (Xtal) structures deposited in the Protein Data Bank (PDB, www.pdb.org) using Jmol. Error is the standard deviation of three measurements. PDB IDs enable easy location of structure files from PDB database. Human serum albumin was used for albumin structure as there was no bovine serum albumin structure within the PDB.

Table 2.3: Hydrodynamic and crystallographic radii of molecules.

Molecule	MW (k)	DLS Rad.	Xtal Long Rad.	Xtal Short Rad.	PDB ID
H ₂ O ₂	0.03	0.19 ± 0.01 [38]			
R6g	0.48	0.63 ± 0.06 [39]			
cyt. c	12	2.12 ± 0.48	1.40 ± 0.12	1.02 ± 0.09	2B4Z [40]
carb.	37	3.04 ± 0.54	2.11 ± 0.06	1.54 ± 0.21	1V9E [41]
ova.	45	3.92 ± 0.94	3.84 ± 0.28	1.57 ± 0.21	1OVA [42]
BSA	67	5.54 ± 1.99	4.05 ± 0.11	2.09 ± 0.09	1AO6 [43]
phos.-b	195	6.09 ± 1.62	5.87 ± 0.17	2.82 ± 0.08	1GPB [44]
β-gal.	464	7.74 ± 2.39	8.62 ± 0.13	6.12 ± 0.18	1DP0 [45]

2.10 References

- [1] M.D. Luque de Castro, F. Priego Capote, N. Sánchez Ávila, Is dialysis alive as a membrane-based separations technique? *TrAC, Trends Anal. Chem.* **27**, 315-326 (2008).
- [2] W.H. Fissell, H.D. Humes, A.J. Fleischman, S. Roy, Dialysis and nanotechnology: now, 10 years, or never? *Blood Purif.* **25**, 12-17 (2007).
- [3] S. Mochizuki, A.L. Zydney, Theoretical analysis of pore size distribution effects on membrane transport, *J. Mem. Sci.* **82**, 211-227 (1993).
- [4] R. Vanholder, G. Glorieux, W. Van Biesen. Advantages of new hemodialysis membranes and equipment, *Nephron Clin. Pract.* **114**, c165-c172 (2010).

- [5] M. Jadoul, Dialysis-related amyloidosis: importance of biocompatibility and age, *Nephrol. Dial. Transpl.* **13**, 61-64 (1998).
- [6] A.K. Cheung, M.V. Rocco, G. Yan, J.K. Leypoldt, N.W. Levin, T. Greene, L. Agodoa, J. Bailey, G.J. Beck, W. Clark, A.S. Levey, D.B. Ornt, G. Schulman, S. Schwab, B. Teehan, G. Eknoyan. Serum β -2 microglobulin levels predict mortality i dialysis patients: results of the HEMO study, *J. Am. Soc. Nephrol.* **17**, 546-555 (2006).
- [7] D. Lee, M. Haase, A. Hasse-Fielitz, K. Paizis, H. Goehl, R. Bellomo. A pilot, randomized, double-blind, cross-over study of high cut-off versus high-flux dialysis membranes, *Blood Purif.* **28**, 365-372 (2009).
- [8] D.H. Krieter, B. Canaud. High permeability of dialysis membranes: what is the limit of albumin loss. *Nephrol. Dial. Transplant.* **18**, 651-654 (2003).
- [9] J.P. Kooman, F.M. van der Sande, K.M. Leunissen, The long road to wearable blood-cleansing devices, *Blood Purif.* **25**, 377-382 (2007).
- [10] W.H. Fissell, A. Dubnisheva, A.N. Eldridge, A.J. Fleishman, A.L. Zydney, S. Roy, High-performance silicon nanopore hemofiltration membranes, *J. Mem. Sci.* **326**, 58-63 (2009).
- [11] C.A. Lopez, A.J. Fleischamn, S. Roy, T.A. Desai, Evaluation of silicon nanoporous membranes and ECM-based microenvironments on neurosecretory cells, *Biomaterials* **27**, 3075-3083 (2006).
- [12] J.K. Holt, H.G. Park, Y. Wang, M. Stadermann, A.B. Artyukhin, C.P. Grigoropoulos, A. Noy, O. Bakajin, Fast mass transport through sub-2-nanometer carbon nanotubes, *Science* **312**, 1034-1037 (2006).
- [13] B.J. Hinds, N. Chopra, T. Rantell, R. Andrews, V. Gavalas, L.G. Bachas, Aligned multiwalled carbon nanotube membranes, *Science* **303**, 62-65 (2004).

- [14] H.D. Tong, H.V. Jansen, V.J. Gadgil, C.G. Bostan, E. Berenschot, E. C.J.M. van Rijn, M. Elwenspoek, Silicon nitride nanosieve membrane, *Nano Lett.* **4**, 283-287 (2004).
- [15] H.U. Osmanbeyoglu, T.B. Hur, H.K. Kim, Thin alumina nanoporous membranes for similar size biomolecule separation, *J. Mem. Sci.* **343**, 1-6 (2009).
- [16] C.C. Striemer, T.R. Gaborski, J.L. McGrath, P.M. Fauchet, Charge- and size-based separation of macromolecules using ultrathin silicon membranes, *Nature* **445**, 749-753 (2007).
- [17] E. Kim, H. Xiong, C.C. Striemer, D.Z. Fang, P.M. Fauchet, J.L. McGrath, S. Amemiya, A structure-permeability relationship of ultrathin nanoporous silicon membrane: a comparison with the nuclear envelope, *J. Am. Chem. Soc.* **130**, 4230-4231 (2008).
- [18] T.R. Gaborski, J.L. Snyder, C.C. Striemer, D.Z. Fang, M. Hoffman, P.M. Fauchet, J.L. McGrath, High performance separation of nanoparticles with ultrathin porous nanocrystalline silicon membranes, *ACS Nano* **4**, 6973-6981 (2010).
- [19] A.A. Agrawal, B.J. Nehilla, K.V. Reisig, T.R. Gaborski, D.Z. Fang, C.C. Striemer, P.M. Fauchet, J.L. McGrath, Porous nanocrystalline silicon membranes as highly permeable and molecularly thin substrates for cell culture, *Biomaterials* **31**, 5408-5417 (2010).
- [20] E.M. Renkin, Filtration, diffusion, and molecular sieving through porous cellulose membranes, *J. Gen. Physiol.* **38**, 225-243 (1954).
- [21] R.E. Beck, J.S. Schultz, Hindered diffusion in microporous membranes with known pore geometry, *Science* **170**, 1302-1305 (1970).
- [22] S.K. Dalvie, R.E. Baltus, Transport studies with porous alumina membranes, *J. Mem. Sci.* **71**, 247-255 (1992).

- [23] P.M. Bungay, H. Brenner, The motion of a closely-fitting sphere in a fluid-filled tube, *Int. J. Multiphase Flow* **1**, 25-56 (1973).
- [24] W.M. Deen, Hindered transport of large molecules in liquid-filled pores, *AIChE J.* **33**, 1409-1425 (1987).
- [25] P. Dechadilok, W.M. Deen, Hindrance factors for diffusion and convection in pores, *Ind. Eng. Chem. Res.* **45**, 6953-6959 (2006).
- [26] A.M. Berezhkovskii, Y.A. Makhnovskii, M.I. Monine, V.Y. Zitserman, S.Y. Shvartsman, Boundary homogenization for trapping by patchy surfaces. *J. Chem. Phys.* **121**, 11390-11394 (2004).
- [27] H.C. Berg, *Random walks in biology* (Princeton Univ. Press, Princeton, NJ, 1993).
- [28] T.F. Weiss, *Cellular Biophysics, Vol. 1: Transport* (MIT Press, Cambridge, MA, 1996) pp. 119-137.
- [29] Y.A. Makhovovskii, A.M. Berezhkovskii, V.Y. Zitserman, Homogenization of boundary conditions on surfaces randomly covered by patches of different sizes and shapes, *J. Chem. Phys.* **122**, 236102 (2005).
- [30] D.R. Latulippe, K. Ager, A.L. Zydney. Flux-dependent transmission of supercoiled plasmid DNA through ultrafiltration membranes. *J. Mem. Sci.* **294**, 169-177 (2007).
- [31] Rasband, W.S., ImageJ, U. S. National Institutes of Health, Bethesda, Maryland, USA, <http://rsb.info.nih.gov/ij/>, 1997.
- [32] N.S. Pujar, A.L. Zydney, Electrostatic and electrokinetic interactions during protein transport through narrow pore membranes, *Ind. Eng. Chem. Res.* **33**, 2473-2482 (1994).
- [33] W.D. Munch, L.P. Zestar, J.L. Anderson, Rejection of polyelectrolytes from microporous membranes, *J. Mem. Sci.* **5**, 77-102 (1979).

- [34] F.G. Smith III, W.M. Deen, Electrostatic effects on the partitioning of spherical colloids between dilute bulk solution and cylindrical pores, *J. Colloid Interf. Sci.* **91**, 571-590 (1983).
- [35] M.S. Ehrenberg, A.E. Friedman, J.N. Finkelstein, G. Oberdorster, J.L. McGrath, The influence of protein adsorption on nanoparticle association with cultured endothelial cells, *Biomaterials* **30**, 603-610 (2009).
- [36] J.H. Shao, R.E. Baltus, Effect of solute concentration on hindered diffusion in porous membranes. *AIChE J* **46**, 1307-1316 (2000).
- [37] W.W. Graessley, Polymer chain dimensions and the dependence of viscoelastic properties on concentration, molecular weight and solvent power, *Polymer* **21**, 258-262 (1980).
- [38] C. B. Muller, A. Loman, V. Pacheco, F. Koberling, D. Willbold, W. Richtering, J. Enderlein, Precise measurement of diffusion by multi-color dual-focus fluorescence correlation spectroscopy, *EPL-Europhys. Lett.* **83**, 46001 (2008).
- [39] B. Csóka, G. Nagy, Determination of diffusion coefficient in gel and in aqueous solutions using scanning electrochemical microscopy, *J. Biochem. Bioph. Methods* **61**, 57-67 (2004).
- [40] N. Mirkin, J. Jaconcic, V. Stojanoff, A. Moreno. High resolution X-ray crystallographic structure of bovine heart cytochrome c and its application to the design of an electron transfer biosensor. *Proteins* **70**, 83-92 (2008).
- [41] R. Saito, T. Sato, A. Ikai, N. Tanaka. Structure of bovine carbonic anhydrase II at 1.95 Å resolution. *Acta Crystallogr., Sect. D* **60**, 792-795 (2004).
- [42] P.E. Stein, A.G. Leslie, J.T. Finch, R.W. Carrell. Crystal structure of uncleaved ovalbumin at 1.95 Å resolution. *J. Mol. Biol.* **221**, 941-959 (1991).

-
- [43] S. Sugio, A. Kashima, S. Mochizuki, M. Noda, K. Kobayashi. Crystal structure of human serum albumin at 2.5 Å resolution. *Protein Eng.* **12**, 439-446 (1999).
- [44] K.R. Acharya, D.I. Stuart, K.M. Varvill, L.N. Johnson. *Glycogen phosphorylase b: description of the protein structure* (World Scientific Publishing, Singapore, 1991).
- [45] D.H. Juers, R.H. Jacobson, D. Wigley, X.J. Zhang, R.E. Huber, D.E. Tronrud, B.W. Matthers. High resolution refinement of β -galactosidase in a new crystal form reveals multiple metal-binding sites and provides a structural basis for alpha-complementation. *Protein Sci.* **9**, 1685-1699 (2000).

Chapter 3

Charge-Based Separations

3.1 Abstract

Molecules and nanoparticles are selectively separated by size as they diffuse through ultrathin porous nanocrystalline silicon (pnc-Si) membranes. As pnc-Si membranes have an innate negative charge, electrostatic interactions can also be used to tune separations. In this work, separations of negatively charged proteins, double-stranded DNA, and nanoparticles are performed with pnc-Si membranes at high and low ionic concentrations. The diffusion of these species is reduced at low salt concentrations, which correlate with less shielding of the surface potential. Both negatively charged proteins and double stranded DNA oligomers had significantly different molecular cutoffs for the different salt concentration solutions. At high ionic concentrations, the rigid DNA oligomers were able to pass through pores with diameters shorter than their long axis, indicating that both short and long axis are important when considering the sieving characteristics of a rigid rod. There was no difference observed separations at different salt concentrations with neutral nanoparticles. Electrostatic terms were added to a previously developed sieving model (Chapter 2), which was shown to compare well with nanoparticle separations.

3.2 Introduction

Nanoporous membranes are an efficient and inexpensive platform used for molecule and particle separations in both research and industry. The separations and purifications performed using nanoporous membranes are often determined by the size selective properties of the membranes; however, electrostatic interactions can also play a roll. Repulsive interactions between charged membranes and like charged molecules or particles effectively reduce the pore size and can hinder the passage of a species through the pores.

These interactions are enhanced in low ionic concentration solutions because shielding of the surface potential, ψ_s , by counterions in the solution is reduced. As a charge material is immersed in an ionic solution, a diffuse layer of counterions associates with the surface. The electric potential exponentially decays within the diffuse layer, and the distance at which the potential equals ψ_s/e , or the approximate length of the diffuse layer, is called the Debye length,

$$\kappa^{-1} = \sqrt{\frac{\epsilon k_b T}{2q^2 c}}. \quad (3.2.1)$$

where ϵ is the dielectric permittivity, k_b the Boltzman constant, T the temperature, and q and c the charge and concentration of the counterion for a symmetric salt [1]. At low ionic concentrations, the Debye length is long and the effects of the surface potential are felt further into the pore interior, which due to repulsive interactions can lead to effectively smaller pores for like charged molecules. The Debye length itself has been used as an approximation for the electrostatic pore size reduction with some success [2].

Electrostatic interactions have been used as a method to tune molecular separations. Molecules of similar size have been separated by using solutions at low ionic concentration and at the isoelectric point of one of the proteins [3, 4]. Proteins that have been modified to have varying numbers of charged residues have been used as charge ladders to visualize the charge-based separation characteristics [5]. The membranes themselves

have been modified by addition of covalently linked charged moieties [4, 6] or by coating with metallic films [7]. In the case of the latter, electric currents through the film have allowed for a switchable charge bias [8].

The membranes used in the previous charge-based separation studies have had thicknesses within the micron range [3, 4, 5, 6, 7, 8]. Such membranes have increased resistance to diffusional transport and fluid flow [9, 10]. In this work, we study the diffusion of molecules through a negatively charged ultrathin (15 nm) nanoporous membrane made from a material termed porous nanocrystalline silicon (pnc-Si) [11]. The nanometer scale pores can be tuned between 5 and 80 nm by the temperature of an annealing step [12]. The ultrathin characteristics have presented unique opportunities in several applications. Small molecules experience little resistance to diffusion [9, 11, 13, 14] while larger molecules are selectively hindered by the pores [9]. Fluid and gas flow has been shown to be orders of magnitude higher than thicker nanoporous membranes [10, 15]. Pnc-Si membranes have little electrical resistance and high electric fields can be achieved across the short distance, which enables rates of electroosmosis that surpass all other electroosmotic materials (Chapter 5).

Previous experiments with pnc-Si membranes have shown that electrostatics can affect the diffusion of small molecules in low salt conditions [11, 13]. While the membrane thickness is not much larger than the molecule diameter, the repulsive forces between the membrane and like charged molecules were large enough to slow or stop diffusion. In this work we take a look at how charge effects can influence the diffusion of larger molecules and nanoparticles. We use globular molecules, proteins, and cylindrical molecules, DNA, to test how molecular shape may play a roll as well. Both negatively charged and neutral spherical nanoparticles were used to probe the electrostatic interactions. Pnc-Si membranes are a useful modeling tool because of their well characterized pores and thickness, and we model the diffusion of charged species by adding electrostatic terms to a previously developed sieving model [9].

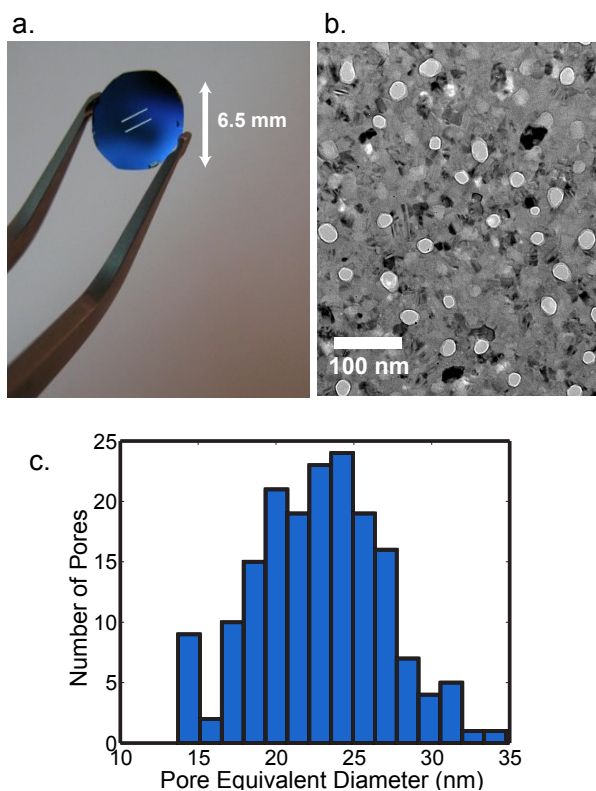


Figure 3.1: Pnc-Si membranes for charge-based separations. **a.** Pnc-Si membranes were fabricated as two 0.1 x 2 mm slits on a 6.5 mm circular silicon chip. **b.** White pores are visible on a field of black diffracting nanocrystals when viewed by transmission electron microscopy. **c.** Pore characteristics can be obtained through image processing routines.

3.3 Methods

3.3.1 Pnc-Si membranes

Pnc-Si membranes are fabricated using previously described techniques on 200 μm thick 4 inch wafers [11, 12]. Photolithography masks were used to define the experimental silicon chips and internal freestanding membrane area depicted in Fig. 3.1, and ~ 80 chips were defined per wafer. A three layer stack of 20 nm silicon dioxide/15 nm amorphous silicon/ 20 nm silicon dioxide was sputtered onto the masked wafers, which were heated to 800-1000°C at 100°C/s in a Solaris 150 rapid thermal processor (Surface Science Integration, El Mirage, AZ) to crystallize the amorphous layer. The pores form between the crystals during this step, and the membrane was exposed through bulk silicon etching with ethylenediamine pyrocatechol with pyrazine (Transene Company, Inc., Danvers, MA) and removal of protective oxide masks with buffered oxide etchant (Mallinckrodt Baker, Phillipsburg, NJ). The pores of the freestanding pnc-Si membranes were analyzed using transmission electron microscopy and image processing algorithms (Fig 3.1b,c). Pnc-Si membranes were prepared for experiments by oxidizing in an oxygen plasma with a chemical vapor deposition oven (Yield Engineering Systems, Livermore, CA). The membranes used in these studies had average pore sizes of ~ 20 nm and porosities of 5%.

3.3.2 Protein Separations

The proteins in Table 3.1, purchased from Sigma-Aldrich (St. Louis, Missouri), were all negatively charged at neutral pH because of their low isoelectric points (pI). Stocks were made by dissolving the powdered proteins in 10 or 100 mM KCl at a concentration of 10 mg/mL. The stocks were combined to form protein mixtures with a final concentration of 0.5 mg/mL for each respective protein at either 10 or 100 mM KCl. Pnc-Si membrane chips were sealed in polypropylene tubes against o-rings [9]. The membrane was used to separate two fluid wells, each 20 μL in volume. The retentate well was initially filled

with the protein mixture at a desired salt concentration and the dialysate well was filled with the equivalent KCl salt concentration. At the termination of the experiment, the retentate contained proteins retained by the membrane while the dialysate contained proteins that were able to diffuse through the membrane. The polypropylene tubes were sealed in microcentrifuge tubes with Parafilm (Pechinney Plastic Packaging, Chicago, IL) and diffusion was allowed to occur for 24 hours.

At the completion of the experiment, the retentate and dialysate volumes were pipetted off the pnc-Si membrane and the proteins were denatured with SDS sample buffer and heating at 95°C. The samples were run on 10% SDS-PAGE gels and stained with coomassie blue. Digital images were taken of the stained gels, and band intensities were measured using ImageJ [16].

The degree of separation was measured using sieving coefficients,

$$S = \frac{\text{concentration of dialysate}}{\text{concentration of retentate}}. \quad (3.3.1)$$

Sieving coefficients, while commonly used to indicate the degree of separation in force flow experiments, can also be used in diffusion separations to describe the progress toward equilibrium [9]. A sieving coefficient of 1 indicates that the separation has fully equilibrated, while a sieving coefficient of zero means the protein is unable to diffuse through the membrane. As intensity is proportional to concentration, sieving coefficients were obtained from the gels by taking the ratio of the integrated band intensities for the retentate and dialysate of each protein. Finally, protein size was obtained using dynamic light scattering (DLS) measurements with a Zetasizer (Malvern Instruments, Worcestershire, UK).

3.3.3 DNA Separations

Double-stranded DNA oligomers of 10 - 1000 base pairs were purchased from Integrated DNA Technologies (Coralville, IA). As each base pair ~ 0.34 nm, the oligomers were

from 3.4 to 340 nm long with a 2 nm radius. The oligomers were allowed to diffuse through the pnc-Si membranes in solutions of 10, 50, and 100 mM salts in phosphate buffered saline in the same setup described for protein. After the experiment was complete, retentate and dialysate wells were removed and run on 1.5% agarose gels. The gels were stained with ethidium bromide and imaged using a Fluor-S MultiImager (BioRad, Hercules, CA). Sieving coefficients were again calculated from the ratio of the integrated band intensities.

3.3.4 Nanoparticle Separations

Gold colloids were purchased from BBInternational (Cardiff, UK) with diameters of 5 and 10 nm and left untreated. Quantum dots (QDs) with a carboxy-PEG coating were purchased from Invitrogen (Carlsbad, CA), and size and zeta potential were measured using the Zetasizer. Silica colloids (c-dots) with fluorescent cores were provided by Ulrich Wiesner's lab at Cornell University [17]. The c-dots were produced as 10 nm Cy-5 labeled and 22 nm sulfo-rhodamine labeled particles with approximate sizes provided by Wiesner's lab. The zeta potential of 22 nm dots was measured using a Zetasizer (Malvern Instruments, Worcestershire, UK), however 10 nm dots could not be measured using this method due to interaction between the 633 nm laser and the fluorescence spectrum of the Cy-5 dye. Ionic concentrations of particle stocks were adjusted by adding 100 mM KCl. Diffusion experiments were set up in the same manner as the protein and DNA separations. Sieving coefficients for gold nanoparticles were determined from retentate and dialysate absorbance peak at 525 nm. Fluorescent emission at 525 nm with excitation at 450 nm for quantum dots and emission at 670 nm with excitation at 620 nm for Cy-5 c-dots were used to determine the respective sieving coefficients.

3.4 Experimental Results

3.4.1 Protein Separations

SDS-PAGE gels of 24 hour protein separations are shown in Fig. 3.2. For the 100 mM KCl experiment, all protein bands are found in the dialysate, while only carbonic anhydrase is strongly present in the dialysate of 10 mM KCl experiment. In Fig. 3.2, we show the sieving coefficients, which were obtained from densitometry of the gels, plotted against protein radius as determined by DLS measurements (Table 3.1). As the proteins are all expected to be negatively charged in the pH 7 solutions, the results indicate that there is greater repulsion between the membrane and proteins at lower ionic concentrations. However, the membrane pores are not completely “closed” by the electrostatic repulsion, as the smallest protein is able to diffuse through in 10 mM KCl.

Table 3.1: Physical characteristics of proteins

molecule	MW	DLS radius	pI
carbonic anhydrase	37000	3.04 ± 0.54	5.85 [18]
ovalbumin	45000	3.92 ± 0.94	4.8 [19]
albumin	67000	5.54 ± 1.99	5.4 [20]
phosphorylase b	195000	6.09 ± 1.62	5.77 [21]
β -galactosidase	495000	7.74 ± 2.39	4.6 [22]

3.4.2 DNA Separations

Agarose gels of DNA oligomers indicated differential separations at different salt concentrations (Fig. 3.3). In 100 mM salts, all oligomers are able to pass through the membrane, while in the 50 mM salt trial only oligomers 50 base pairs or less can diffuse through. Oligomers do not pass through the membrane in 10 mM salt. The low ionic concentrations therefore increase the membrane hindrance to negatively charged DNA oligomers. Osmotic gradients can form when ionic concentrations are unbalanced between the two wells, and in such cases all oligomers diffuse through the membrane

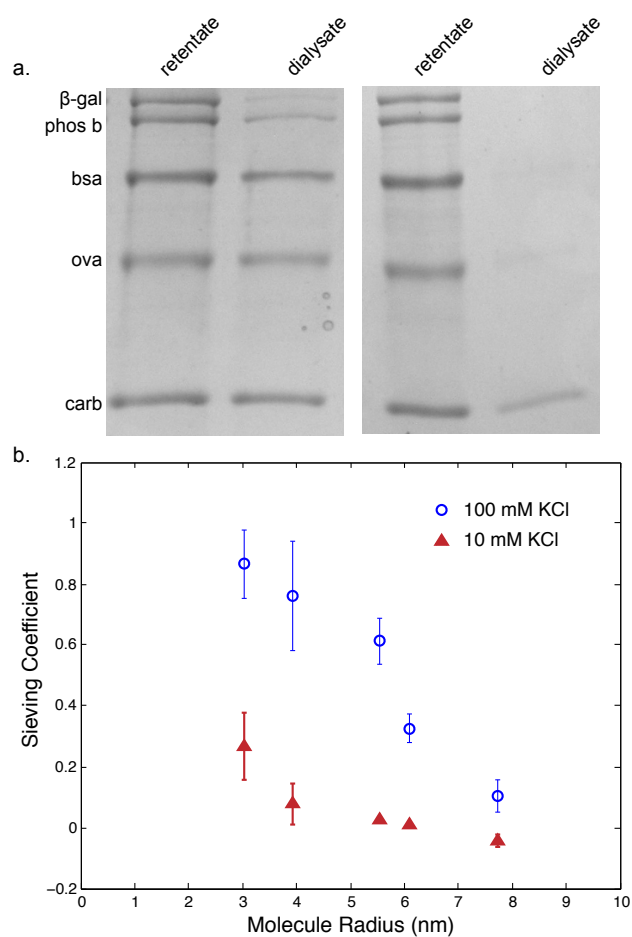


Figure 3.2: Charge-based protein separations. a. SDS-PAGE gels of 24 hour protein diffusion studies. b. Analysis of gels indicates reduced diffusion of proteins in the low ionic concentration experiment.

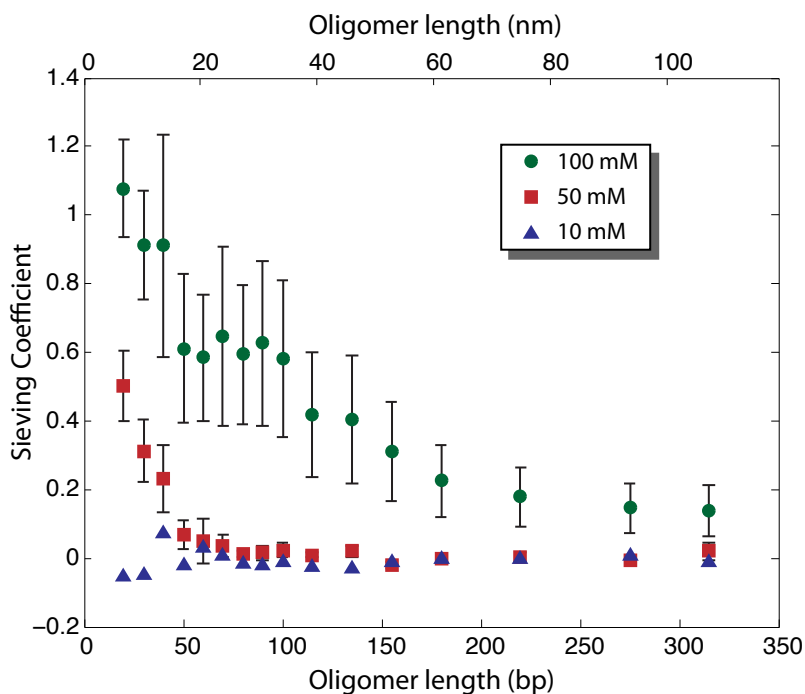


Figure 3.3: Charge-based DNA diffusion through pnc-Si membranes. **a.** The sieving coefficients of a 24 hour DNA separation experiment in 155 mM salts in PBS. **b.** The sieving coefficients of a 24 hours separation in 10 mM salts. Very few of the oligomers pass through the membrane at low salts (Figure prepared with the help of Paul Black).

even in low salt solutions. As DNA oligomers in this size range behave as rigid rods, it is thought that the osmotic gradient acts to align the DNA so that the short axis (~ 2 nm) passes through the pore. In osmotically balanced experiments, the oligomers will have some degree of rotational diffusion that influences the dynamics of diffusion through the pores.

3.4.3 Dynamics of DNA Diffusion

DNA oligomers have both rotational and translational diffusion. If an oligomer rotates faster than it translates along its axis, on the timescale of its diffusion to the pore, the oligomer will appear as a sphere (Fig. 3.4a). However, if the oligomer translates along its axis faster than it rotates, the oligomer may simply pass axially through the pore

with the hindrance defined by the radius of the oligomer (Fig. 3.4b). To compare these processes, we can look at the expressions for rotational and translational diffusion. The rotational diffusion of a cylinder can be expressed as

$$D_{\text{rot}} = k_b T \frac{\ln(L/2r) - 0.20}{2\pi\mu L} \quad (3.4.1)$$

where L is the length of the cylinder, r the radius of the cylinder, and μ the viscosity of the solution [24]. The average time for a rotation of θ radians can be calculated as

$$t = \frac{\theta^2}{6D_{\text{rot}}} \quad (3.4.2)$$

with three degrees of freedom. The translational diffusion along the long axis of the cylinder can be expressed similarly as [24],

$$D_{\text{trans}} = k_b T \frac{\ln(L/2r) - 0.66}{\frac{1}{3}\pi\mu L^3}. \quad (3.4.3)$$

The average time to translate a given distance with three degrees of freedom is

$$t = \frac{x^2}{6D_{\text{trans}}}. \quad (3.4.4)$$

In Fig. 3.4c, we compare the average time of a full rotation (2π rad) to a translation equal to the length of the oligomer. Note that these equations break down under 5 nm due to the small aspect ratio. The average time for translation is greater than the average time for rotation for all oligomer sizes. As the oligomer size increases, so does the time for translation of the longer length and full rotation of the molecule. In Fig. 3.4d we show the ratio of rotation to translation time. The smallest molecules translate much faster than they rotate, but as the molecules increase in size, this ratio plateaus at 0.8. Since both translation and rotation are on the same time scale, the sieving characteristics of cylindrical DNA oligomers must be determined by a combination of

long and short axes.

3.4.4 Nanoparticle Separations

Gold nanoparticles were not stable in high ionic concentration solutions, as was evidenced by a red shift in their absorbance while in solutions with concentrations > 10 mM. This red shift is due to irreversible aggregation of the particles, which is caused by a reduction in ionic shielding and fusing of the particles as they approach each other [25]. The gold particles have highly negative zeta potentials (-50 mV, Table 3.2) and do not appear to diffuse through membranes in experiments carried out at 0 mM (diH_2O) and 10 mM KCl for 24 hours. The sensitivity of this measurement was low, however, and sieving coefficients < 0.1 are difficult to measure. The 5 nm gold particles do not appreciably diffuse through membranes with 20 nm pores, though the same particles will pass through a membrane when pressurized [10]. While this observation may be due to the low sensitivity of the measurement or the potentially long times required to diffuse through a smaller effective pore diameter, pressurization may also provide a force that allows for particles to overcome an energy barrier that occurs within the short pores.

The QDs used in these experiments are composed of a core metallic particle surrounded by a carboxy-polyethylene glycol (PEG) coating. The carboxy-PEG coating allowed the particles to remain stable in high ionic concentration solutions, in comparison to the aggregating gold particles. The entire QD structure measured 12.8 nm by DLS measurements. Zeta potential measurements of QDs resulted in a -40 mV zeta potential, though the stock had visible aggregates after the measurement. This may be due to the electric field disrupting the PEG layer and allowing the metallic cores to aggregate. The PEG molecules are terminated in deprotonated COOH groups at neutral pH, which would provide a negative zeta potential. The charged QDs are able to pass through membranes in high ionic strength solutions, but not in low ionic strength solutions.

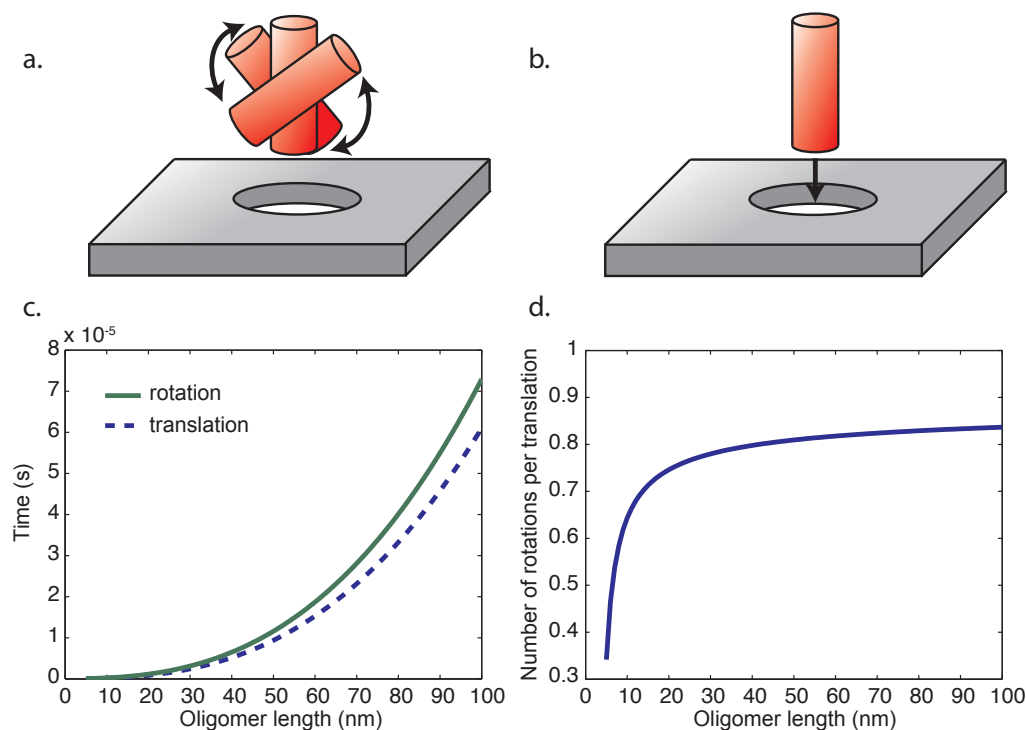


Figure 3.4: Relative times for DNA rotation and translation. **a.** If rotation occurs quickly in relation to translation time, the DNA molecule may appear as a sphere with diameter similar to length of the long axis. **b.** If DNA translation is faster than rotation, the DNA could pass through a small pore axially with its radius determining the hindrance. **c.** The average time for a DNA oligomer to fully rotate (2π rad) is compared to the average time for the molecule to diffuse its length. Full rotations are slower than the translation for all oligomer lengths. **d.** The ratio of rotation to translation time is taken from panel c. to obtain the number of full rotations for one translation of the oligomer's length. Small oligomers translate faster than they rotate. The hindrance of DNA oligomers must be based on a combination of long axis and radius dimensions.

Table 3.2: Separations with nanoparticles

particle	size (nm)	zeta potential (mV)	ionic strength (mM)	sieving coefficient
gold	5	-50	0	0
	5	-50	10	0
	10	-50	10	0
c-dot	10	0	0	0.58 ± 0.02
		0	50	0.59 ± 0.02
QD	12.8	-40	10	0.02 ± 0.01
		-40	100	0.24 ± 0.02

The silica c-dot particles have zeta potentials of zero, and represent a neutral particle. As such, c-dots are not expected to be influenced by electrostatic effects at low salt concentrations. Experiments at 0 mM and 50 mM KCl provide the same sieving coefficients (Table 3.2). In contrast to the negatively charged quantum dots, the 10 nm c-dots were able to diffuse through the membrane equally at both salt concentrations. The 22 nm c-dots were not able to diffuse through at either salt concentrations because of their large size.

The nanoparticle separations illustrate how the specific physicochemical characteristics of the particles influence the separations. Size alone is not a predictor of the degree to which a membrane can separate a species.

3.5 Theoretical Comparison

Our previously developed 3-D model of diffusion was shown to agree with protein separations in 100 mM KCl (Chapter 2, [9]); however, this model contained no electrostatic components. The dimensions of the experimental setup were included in a computer aided design (CAD) model and molecular diffusion was simulated over time using Multiphysics (COMSOL, Stockholm, SWE) (Fig. 3.5). In the free solution domains of the model, diffusing species are given free diffusion coefficients, D_0 , as obtained from the

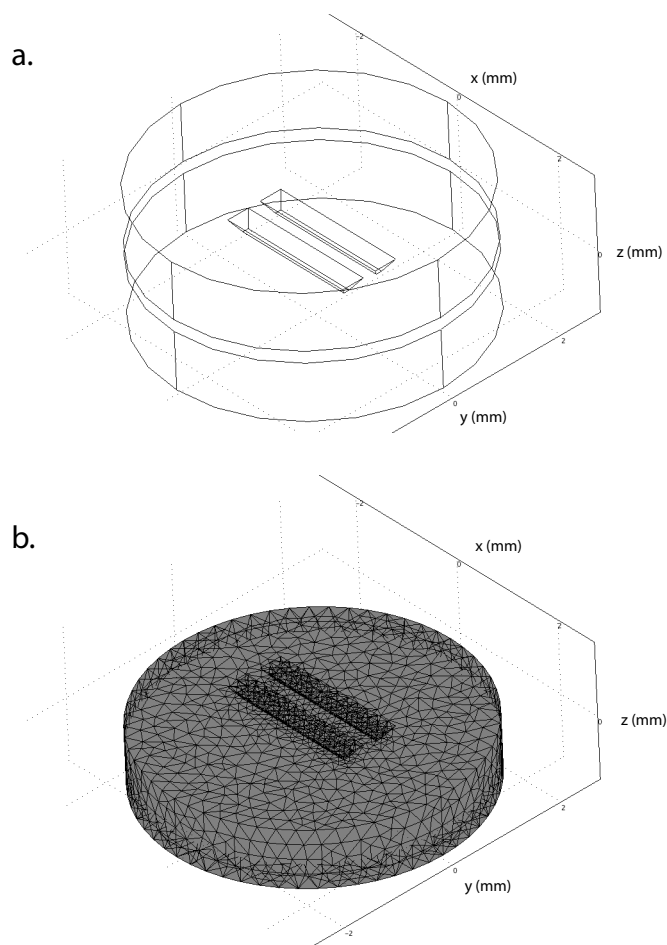


Figure 3.5: 3-D CAD model with mesh visualization. **a.** In the CAD model used for 3-D simulations, two slits of free standing membrane separate the retentate and dialysate wells. **b.** The COMSOL generated mesh in the vicinity of the freestanding membrane is shown by cutting away the top (retentate) fluid well. An “Extremely Fine” preset mesh is swept through the ultathin membrane subdomains, while the fluid wells are given the coarser “Finer” preset mesh.

Stokes-Einstein relation,

$$D_0 = \frac{k_b T}{6\pi\mu R_s}, \quad (3.5.1)$$

where R_s is the radius of the species. As shape and rotational diffusion are neglected, this treatment only holds well for spherical molecules and particles. In the thin membrane domain of the model, the simulated species are given an effective diffusion coefficient, D_m . The reduced diffusion within the membrane was obtained through the addition of two sources of resistance: resistance associated with diffusion parallel to the membrane surface to a pore entrance (pore discovery) and the resistance imparted by the pores during transmembrane diffusion. Sieving coefficients can be obtained at the completion of the simulation by taking the homogenized concentrations of the retentate and dialysate in the model.

Electrostatics can be modeled by their effect on the membrane resistance, and in this continuation of the previous model [9], we determine their influence on the transmembrane resistance. We defined the transmembrane resistance using hindrance theory, which considers the reduced diffusion to be a function of a partition coefficient, ϕ and a hindrance factor K_d , [26]

$$\frac{D_m}{D_0} = \phi K_d. \quad (3.5.2)$$

The partition coefficient describes the ratio of solubility in the pore to the bulk, and can be represented by

$$\phi = 2 \int_0^{1-\lambda} e^{-\mathbb{E}/k_b T} \rho \, d\rho \quad (3.5.3)$$

where λ is the ratio of molecule size to pore size, R_s/R_p , and ρ the radial parameter [27]. The Boltzmann factor $e^{-\mathbb{E}/k_b T}$ can be used to incorporate electrostatic effects, and traditional hindrance theory simplifies the integral by neglecting electrostatics and taking $\mathbb{E} = 0$ [26, 28]. The hindrance factor adds the effects of frictional resistance to Eq. (3.5.2),

$$K_d = \frac{\int_0^{1-\lambda} K^{-1} e^{-\mathbb{E}/k_b T} \rho \, d\rho}{\int_0^{1-\lambda} e^{-\mathbb{E}/k_b T} \rho \, d\rho} \quad (3.5.4)$$

where K is the enhanced drag, or the ratio of drag on a sphere within a pore to that of a free sphere [29]. Hindrance factors have been determined for molecule positions only on the centerline of the pore ($\rho = 0$) and for molecules occupying all possible radial positions within the pore, although the centerline approximation appears sufficient in most cases [28].

An early model of charge-based separations used partition coefficients and hindrance factors for the $\mathbb{E} = 0$ case and simple reduced pore radii and increased molecule radii by the Debye length [2]. While this method correlated with separation data, it was not an accurate theoretical model as Debye lengths are not a boundary of electric potential. An improved model by Dechadilok and Deen uses Boltzmann factors representing the electric potential for a molecule within a pore [29]. This model also included a consideration of the relaxation effect, or a retarding force caused by the continual distortion and reshaping of the diffuse layer during diffusion. The partition coefficient was found using a previous analytic solution by Smith and Deen [30]. A centerline approximation [31] was used to determine the hindrance factor under the assumption that electrostatics would serve to bias the molecule toward the centerline. The calculated excess drag due to the relaxation effect was found to be much smaller than the electrostatic reduction of the partition coefficient. Thus in our 3-D model, we model the transmembrane resistance by determining the electrostatic effects on the partition coefficient and by using a centerline hindrance factor.

To determine the partition coefficient, the energy within the Boltzmann factor of Eq. (3.5.3) is expressed as a dimensionless difference between the free energy of the species in the pore and at infinite separation, ΔG ,

$$\mathbb{E}(\rho) = R_p \epsilon (RT/F)^2 \Delta G \quad (3.5.5)$$

where ϵ is the permittivity of the solution, R the gas constant, and F Faraday's constant. Assuming that the diffusing species is a solid sphere with a constant surface charge

density, ΔG can be approximated as

$$\Delta G = \frac{\frac{8\pi\tau\lambda e^{\tau\lambda}}{(1+\tau\lambda)^2}\Lambda\sigma_s^2 + \frac{4\pi^2\lambda^2 I_0(\tau\rho)}{(1+\tau\lambda)I_1(\tau)}\sigma_s\sigma_p + \frac{\pi I_0(\tau\rho)}{\tau I_1(\tau)} \frac{(e^{\tau\lambda} - e^{-\tau\lambda})\tau\lambda\Gamma(\tau\lambda)}{(1+\tau\lambda)}\sigma_p^2}{\frac{\pi\tau e^{-\tau\lambda} - 2(e^{\tau\lambda} - e^{-\tau\lambda})\tau\lambda\Gamma(\tau\lambda)\Lambda}{(1+\tau\lambda)}} \quad (3.5.6)$$

where τ is the ratio of pore radius to Debye length, σ_s the surface charge density of the sphere, and σ_p the surface charge density of the pore [30]. I indicates modified Bessel functions of the first kind. For experimental comparison, the surface charge density of the sphere and pore are determined using

$$\sigma_s = \frac{\psi_s(1 + \tau\lambda)}{\lambda}, \sigma_p = \frac{\psi_p\tau I_1(\tau)}{I_0(\tau)} \quad (3.5.7)$$

where the surface potential of the pore and sphere, ψ_s and ψ_p , are estimated as experimentally derived zeta potentials. We note that the actual surface potential is most likely higher in magnitude than the zeta potential due to adsorbed counterions on the surface, but only the zeta potential can be obtained experimentally. The function $\Gamma(\tau\lambda)$ is given by $\Gamma(\tau\lambda) = \coth(\tau\lambda) - 1/\tau\lambda$ and the function Λ , is given by

$$\Lambda \cong \frac{\pi}{2} \sum_{i=0}^{\infty} \frac{\rho^i (2i)!}{2^3 (i!)^2} I_i \left[\tau K_{i+1}(2\tau) + \frac{3}{4} K_i(2\tau) \right] \quad (3.5.8)$$

where K represents modified Bessel functions of the second kind. Λ is accurate for $\tau \geq 3$, which is satisfied for pores 10 nm or larger at 10 mM ionic concentrations. The solution to the partition coefficient, Eq. (3.5.3) was found by taking 10 iterations of Λ and using Simpson's rule with 20 subintervals to solve the integral (convergence is obtained with these parameters). A polynomial of order eight was used to fit the coefficients from Higdon and Muldowney to obtain a centerline hindrance factor [31].

For our simulations, the transmembrane resistance was obtained for each pore in the pore distribution by using the partition coefficients and hindrance factor, Eq. (3.5.2). The transmembrane resistance was then added to the pore discovery resistance, and a reduced diffusion coefficient, D_m , was found for the membrane region of the model

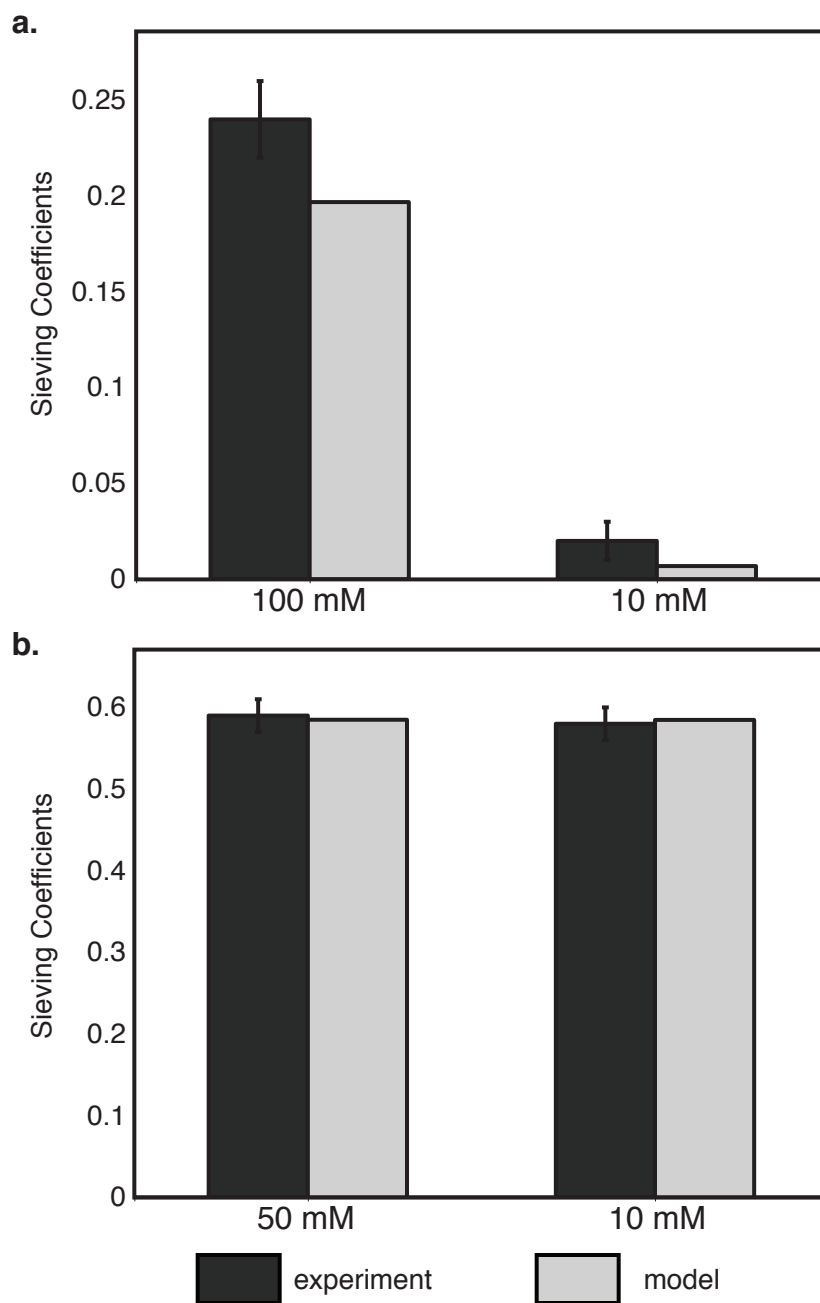


Figure 3.6: Experimental and theoretical separations with nanoparticles. a. Theory and experiment agree that negatively charged quantum dots have lower sieving coefficients in the lower ionic concentration separation. **b.** Neutral c-dots exhibit similar separations in different ionic concentration solutions for both theory and experiment.

(Chapter 2, [9]).

Experimental nanoparticle separations were compared to 3-D sieving simulations with the inclusion of electrostatic effects. Membrane zeta potential of -27 mV, obtained from streaming potential measurements (Chapter 5), was used in the simulations. QD comparisons were performed using the DLS measured size, 12.8 nm, and zeta potential, -40 mV. The sieving coefficients from the simulation were slightly lower to those of the experiments, which could be due to errors in QD size, pore size, QD zeta potential, or membrane zeta potential measurements. Both experiment and simulation show reduced sieving coefficients for the lower ionic strength experiments (Fig. 3.6a).

The neutral c-dot separations were also simulated using the 3-D sieving model. The model greatly underestimated the diffusion of 10 nm neutral particles. Since we could not confirm the particle size by DLS measurements, error in size measurement may contribute to the mismatch between experiment and model. We performed the simulation with smaller molecules, and found that 4.2 nm particles better matched the experimentally observed fast diffusion of the c-dots. In Fig. 3.6b we compare the c-dot experiments to simulations with neutral 4.2 nm particles. The model indicates that little difference in sieving coefficient is expected for neutral molecules at different salt concentrations.

3.6 Conclusions and Future Direction

The results presented in this work show that electrostatic interactions have a strong effect on separations with ultrathin membranes at low ionic concentrations. The physicochemical characteristics of the particles and molecules allow different degrees of electrostatic interaction, and thus are strong determinants of the separation quality. The negatively charged molecules and particles have different degrees of separation at high and low ionic concentrations, while neutral particles are unaffected. The cylindrical DNA oligomers were able to diffuse through pores that were smaller than their longest

dimension, and electrostatics had a strong effect on their diffusion as well. The surface charge of the species can be accounted for theoretically, and comparisons between theory and experiment hold for spherical particles.

This work can be expanded both experimentally and theoretically. While we featured separations with negatively charged and neutral species, we have not considered the effects of electrostatics on the diffusion of positively charged species through a negatively charged membrane. The membrane charge can be increased or changed from negative to positive by surface modifications such as silanization. Positive membranes have previously been shown to affect the diffusion of small charged dyes [11]. Attractive interactions could potentially increase the adsorption of molecules to the surface, which in turn may alter the membrane zeta potential [32]. Peptide nucleic acids (PNA) would allow for experiments with a neutral rod shaped species.

Computational simulations can be used to compare to particles and molecules as long as size and zeta potential data is available. Our first attempt at modeling particles appears to be promising, and this method can be extended to other spherical species. Hindrance factors can be obtained for cylindrical rods moving along the axis of a capillary [33], which may enable theoretical simulations for rigid rods like DNA oligomers or carbon nanotubes through pores. We do not take into account entrance and exit effects in our current model, which may be significant when considering electrostatic interactions in an short pore. Such effects may be observable using electrostatic force microscopy measurements [34].

In conclusion, this work highlights charge-based separations with nanometer scale molecules and species and pnc-Si membranes. Pnc-Si has also enabled the direct comparison of experimental separations to the theory of electrostatic interactions within pores.

3.7 References

- [1] R.F. Probstein, *Physicochemical Hydrodynamics* (Wiley, Hoboken, NJ, ed. 2, 2003) pp. 165-236.
- [2] W.D. Munch, L.P. Zestar, J.L. Anderson, Rejection of polyelectrolytes from microporous membranes, *J. Mem. Sci.* **5**, 77-102 (1979).
- [3] H.U. Osmanbeyoglu, T.B. Hur, H.K. Kim, Thin alumina nanoporous membranes for similar size biomolecule separation, *J. Mem. Sci.* **343**, 1-6 (2009).
- [4] R. van Reis, J.M. Brake, J. Charkoudian, D.B. Burns, A.L. Zydney, High-performance tangential flow filtration using charged membranes, *J. Mem. Sci.* **159**, 133-142 (1999).
- [5] M.K. Menon, A.L. Zydney, Protein charge ladders: a new technique for studying electrostatic interactions in ultrafiltration systems, *J. Mem. Sci.* **181**, 179-184 (2001).
- [6] D.B. Burns, A.L. Zydney, Buffer effects on the zeta potential of ultrafiltration membranes, *J. Mem. Sci.* **172**, 39-48 (2000).
- [7] C.R. Martin, M. Nishizawa, K. Jirage, M.S. Kang, S.B. Lee, Controlling ion-transport selectivity in gold nanotubule membranes, *Adv. Mater.* **13**, 1351-1362 (2001).
- [8] M. Nishizawa, V.P. Menon, C.R. Martin, Metal nanotubule membranes with electrochemically switchable ion-transport selectivity, *Science* **268**, 700-702 (1995).
- [9] J.L. Snyder, A. Clark Jr., D.Z. Fang, T.R. Gaborski, C.C. Striemer, P.M. Fauchet, and J.L. McGrath, An experimental and theoretical analysis of molecular separations by diffusion through ultrathin nanoporous membranes, *J. Mem. Sci.* **369**, 119-129 (2011).

- [10] T.R. Gaborski, J.L. Snyder, C.C. Striemer, D.Z. Fang, M. Hoffman, P.M. Fauchet, J.L. McGrath, High performance separation of nanoparticles with ultrathin porous nanocrystalline silicon membranes, *ACS Nano* **4** 6973-6981 (2010).
- [11] C.C. Striemer, T.R. Gaborski, J.L. McGrath, P.M. Fauchet, Charge- and size-based separation of macromolecules using ultrathin silicon membranes, *Nature* **445**, 749-753 (2007).
- [12] D.Z. Fang, C.C. Striemer, T.R. Gaborski, J.L. McGrath, P.M. Fauchet, Methods for controlling the pore properties of ultra-thin nanocrystalline silicon membranes, *J. Phys.: Condens. Matter* **22**, 454134 (2010).
- [13] E. Kim, H. Xiong, C.C. Striemer, D.Z. Fang, P.M. Fauchet, J.L. McGrath, S. Amemiya, A structure-permeability relationship of ultrathin nanoporous silicon membrane: a comparison with the nuclear envelope, *J. Am. Chem. Soc.* **130**, 4230-4231 (2008).
- [14] R. Ishimatsu, J. Kim, P. Jing, C.C. Striemer, D.Z. Fang, P.M. Fauchet, J.L. McGrath, S. Amemiya, Ion-selective permeability of an ultrathin nanopore silicon membrane as probed by scanning electrochemical microscopy using micropipet-supported ITIES tips, *Anal. Chem.* **82**, 7127-7134 (2010).
- [15] M.N. Kavalenka, C.C. Striemer, D.Z. Fang, K. Shome, T.R. Gaborski, J.L. McGrath, P.M. Fauchet, Ballistic and non-ballistic gas flow through ultrathin nanopores, *Phys. Rev. Lett* In Review.
- [16] W.S. Rasband, ImageJ, U. S. National Institutes of Health, Bethesda, Maryland, USA, <http://rsb.info.nih.gov/ij/>, 1997.
- [17] H. Ow, D.R. Larson, M. Srivastava, B.A. Baird, W.W. Webb, U. Wiesner, Bright and stable core-shell fluorescent silica nanoparticles, *Nano Lett.* **5**, 113-117 (2005).

- [18] E.F. Robertson, H.K. Dannelly, P.J. Malloy, H.C. Reeves, Rapid isoelectric focusing in a vertical polyacrylamide minigel system, *Anal. Biochem.* **167**, 290-294 (1987).
- [19] K. Suzuki, Y. Miyosawa, C. Suzuki, Protein denaturation by high pressure. Measurements of turbidity of isoelectric ovalbumin and horse serum albumin under high pressure, *Arch. Biochem. Biophys.* **101**, 225-228 (1963).
- [20] Q. Shi, Y. Zhou, Y. Sun, Influence of pH and ionic strength on the steric mass action model parameters around the isoelectric point of protein, *Biotechnol. Progr.* **21**, 516-523 (2005).
- [21] T. Hayakawa, J.P. Perkins, D.A. Walsh, E.G. Krebs, Physicochemical properties of rabbit skeletal muscle phosphorylase kinase, *Biochem.* **12**, 567-573 (1973).
- [22] A. Hoyoux, I. Jennes, P. Dubois, S. Genicot, F. Dubail, J.M. François, E. Baise, G. Feller, C. Gerday, Cold-adapted β -galactosidase from the antarctic psychrophile *Pseudoalteromonas haloplanktis*, *Appl. Environ. Microb.* **67**, 1529-1535 (2001).
- [23] D.R. Latulippe, K. Ager, A.L. Zydney. Flux-dependent transmission of supercoiled plasmid DNA through ultrafiltration membranes. *J. Mem. Sci.* **294**, 169-177 (2007).
- [24] J. Howard, *Mechanics of motor proteins and the cytoskeleton* (Sinauer Associates, Sunderland, MA, 2001) pp. 107.
- [25] C.S. Weisbecker, M.V. Merritt, G.M. Whitesides, Molecular self-assembly of aliphatic thiols on gold colloids, *Langmuir* **12**, 3763-3772 (1996).
- [26] W.M. Deen, Hindered transport of large molecules in liquid-filled pores, *AIChE J.* **33**, 1409-1425 (1987).
- [27] T.F. Weiss, *Cellular Biophysics, Vol. 1: Transport* (MIT Press, Cambridge, MA, 1996) pp. 119-137.

- [28] P. Dechadilok, W.M. Deen, Hindrance factors for diffusion and convection in pores, *Ind. Eng. Chem. Res.* **45**, 6953-6959 (2006).
- [29] P. Dechadilok, W.M. Deen, Electrostatic and electrokinetic effects on hindered diffusion in pores, *J. Mem. Sci.* **336**, 7-16 (2009).
- [30] F.G. Smith III, W.M. Deen, Electrostatic effects on the partitioning of spherical colloids between dilute bulk solution and cylindrical pores, *J. Colloid Interf. Sci.* **91**, 571-590 (1983).
- [31] J.J.L. Higdon, G.P. Muldowney, Resistance functions for spherical particles, droplets and bubbles in cylindrical tubes, *J. Fluid Mech.* **298**, 193-210 (1995).
- [32] K.J. Kim, A.G. Fane, M. Nystrom, A. Pihlajamaki, Chemical and electrical characterization of virgin and protein-fouled polycarbonate track-etched membranes by FTIR and streaming-potential measurements, *J. Mem. Sci.* **134**, 199-208 (1997).
- [33] J. Happel, H. Brenner, *Low Reynolds Number Hydrodynamics* (Prentice-Hall, Englewood Cliffs, NJ, 1965) pp. 331-346.
- [34] Y. Sugawara, T. Uchihashi, M. Abe, S. Morita, True atomic resolution imaging of surface structure and surface charge on the GaAs(110), *Appl. Surf. Sci.* **140**, 371-375 (1999).

Chapter 4

Pressurized Separations[†]

4.1 Abstract

Porous nanocrystalline silicon (pnc-Si) is a 15 nm thin free-standing membrane material with applications in small-scale separations, biosensors, cell culture, and lab-on-a-chip devices. Pnc-Si has already been shown to exhibit high permeability to diffusing species and selectivity based on molecular size or charge. In this report, we characterize properties of pnc-Si in pressurized flows. We compare results to long-standing theories for transport through short pores using actual pore distributions obtained directly from electron micrographs. The measured water permeability is in agreement with theory over a wide range of pore sizes and porosities and orders of magnitude higher than those exhibited by commercial ultrafiltration and experimental carbon nanotube membranes. We also show that pnc-Si membranes can be used in dead-end filtration to fractionate gold nanoparticles and protein size ladders with better than 5 nm resolution, insignificant sample loss, and little dilution of the filtrate. These performance characteristics, combined with scalable manufacturing, make pnc-Si filtration a straightforward solution to many nanoparticle and biological separation problems.

[†]Adapted from: T.R. Gaborski, J.L. Snyder, C.C. Striemer, D.Z. Fang, M. Hoffman, P.M. Fauchet, J.L. McGrath, High-Performance Separation of Nanoparticles with Ultrathin Porous Nanocrystalline Silicon Membranes, *ACS Nano* 4, 2010, 69736981.

4.2 Introduction

The need to physically separate similarly sized solutes is a ubiquitous problem in biological research and in the production of biomolecules and other nanoparticles. Compared to resin-based chromatography, membrane separations are simpler, more energy efficient, and more readily scaled between laboratory and industry [1]. Fundamental advances in membrane technology that impact the efficiency of ultrafiltration processes can lower drug and food costs, accelerate the process of discovery in biological laboratories, and enable new devices such as wearable blood dialysis systems. While membrane-based bind and elute strategies such as ion exchange and affinity methods have advanced significantly in recent years [2, 3, 4] size-exclusion chromatography, the most robust method for separating similarly sized macromolecules, still has no commonly used membrane analog. Ideally, a nanoporous membrane could be used as a sieve to precisely fractionate a mixture of nanoparticles forced through the membrane with little dilution or contamination of the filtrate.

Traditional ultrafiltration membranes, made from solvent-casted polymers, have tortuous path, sponge-like, pore structures that limit the resolution of separations. Such membranes are typically used to separate materials that are orders of magnitude different in size in dialysis, solute concentration, and buffer exchanges. The membranes are also micrometers thick and highly porous, giving more than $100 \mu\text{m}^2$ of internal surface area for every μm^2 of frontal surface [5]. High internal surface area leads to flow resistance, sample loss, and clogging in flow-through filtration systems. Experimental thin (~ 50 - 100 nm) tortuous path membranes made from cross-linked proteins [6] or polymers [6] have pore size cut-offs appropriate for nanofiltration (< 2 nm) rather than ultrafiltration (2 - 50 nm)[7].

To create idealized membranes for size-based separations, technologists have developed nanoporous membranes with well-defined and tunable pore sizes. Aluminum oxide and track-etched membranes are commercially available examples, but the pores in these

membranes are too large (>20 nm) for many biological separations. In addition, these membranes are very thick ($6\text{--}10\text{ }\mu\text{m}$) so that transport is too slow for many purification processes [8]. Silicon patterning techniques have been used to create membranes with uniform 10 nm wide pores [9], but the thickness ($4\text{ }\mu\text{m}$) and low porosity ($\sim 1\%$) of these membranes again limit transport. Flow through membranes created from aligned carbon nanotubes (CNTs) has been shown to exceed the predictions of viscous flow theory because of the smooth and hydrophobic walls of CNTs; however, the pore sizes are limited to a small range between 2 and 6 nm that depends on the particular CNT formulation used. Ultrathin silicon membranes (~ 10 nm) with defined pores (25 nm) were first created using an ion-beam drilling process that is far too slow for scale up [10]. Recently, track-etched technology has been applied to SiN membranes to create 100 nm thick membranes with pore sizes that can be tuned between ~ 10 and 50 nm depending on the time allotted to etching [11]; however, this technique requires access to a cyclotron capable of heavy ion (Bi, Xe) bombardment and thus also faces high volume manufacturing challenges.

Here we examine the pressurized flow and filtration properties of ultrathin porous nanocrystalline silicon (pnc-Si). Pnc-Si is a recently developed material created by crystallizing a thin amorphous silicon film to produce nanometer-sized voids that become throughpores [12]. The membranes are mass-produced on silicon wafers using standard microfabrication tools and processes. Free-standing membranes as thin as 15 nm have been shown to withstand up to an atmosphere of pressure without mechanical failure. Pore distributions exhibit sharp cut-offs that can be tuned between 5 and 80 nm by changing the annealing temperature during fabrication [12]. In contrast to polymer membranes, pnc-Si membranes have $\sim 0.1\text{ }\mu\text{m}^2$ of internal surface area for every μm^2 of frontal surface. Fast diffusion and molecular separations with pnc-Si have already been demonstrated for small solutes [12, 13]; however, the use of pnc-Si membranes as flow-through filters has not been previously investigated.

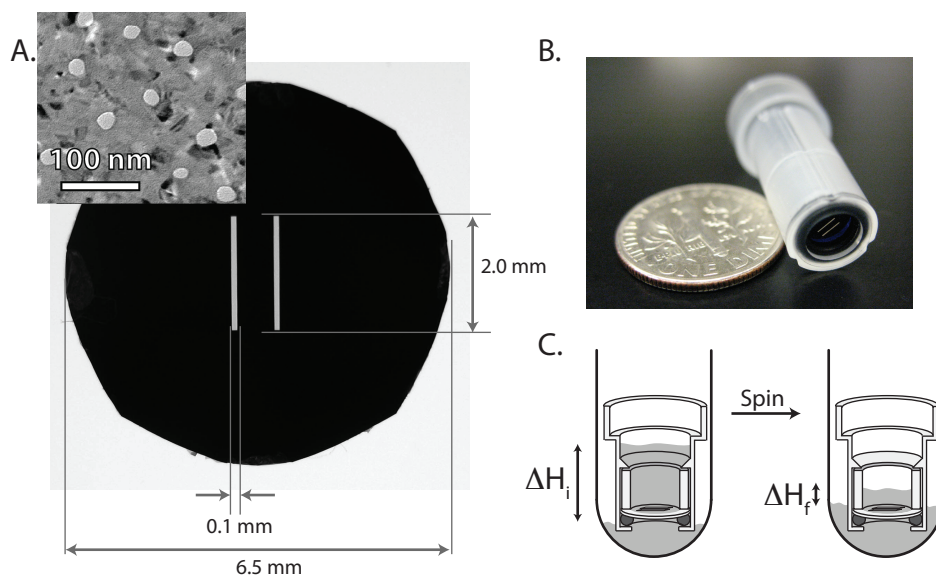


Figure 4.1: Pnc-Si membranes and experimental setup **A.** Circular pnc-Si chip formatted for plastic centrifuge tube inserts. The two internal slits are areas of free-standing pnc-Si membrane. Inset: TEM micrograph of pnc-Si membranes. Pores are white, and nanocrystals are black. **B.** Assembled centrifuge tube insert. **C.** Schematic of hydraulic permeability test. The insert is filled with water and placed in a larger collection tube pre-filled with water. The system is spun in a centrifuge, and the volume of water that passes through the membrane is measured. Hydraulic permeability measurements are taken before the system reaches equilibrium.

4.3 Results and Discussion

We examined the hydraulic permeability of pnc-Si membranes using bucket-style devices resembling those commonly used for concentrating nanomaterials (Fig. 4.1). The devices housed 6.5 mm diameter silicon membrane chips with free-standing membranes over two 2 mm × 0.1 mm windows (Fig. 4.1A). Water was forced through the membranes in a centrifuge. Interestingly, the membranes were found to be impermeable to water unless both sides of the membrane were wet (discussed below), so water was also added to the outer test tube to immerse the membrane. The difference in water levels between the inside and outside containers creates a pressure drop across the membrane that diminishes over time (Fig. 4.1C). Fluid volumes in both containers were determined by weighing samples at different time points, and the hydraulic permeability was

determined by fitting data to a formula that describes the evolution of fluid levels in both containers (see Supporting Information).

We compared water flow rates through pnc-Si to a formula derived by Dagan *et al.* [14] describing low Reynolds number flow through short pores accounting for entrance, exit, and tube resistances (see Supporting Information). We used custom image processing routines (Fig. 4.5) to determine the distribution of pore sizes in a transmission electron micrograph (Fig. 4.2A) and then used the Dagan formula to calculate the predicted water flow through each pore in the micrograph. The theoretical hydraulic permeability for each membrane tested was calculated by summing the flows through the individual pores and dividing by the total area imaged in the micrograph. An example of our analysis is shown in Fig. 4.2. Fig. 4.2A shows the pore number histogram for a particular membrane, and Fig. 4.2B shows the predicted water flow through each pore in the image. Dagan's formula has been previously validated for micrometer thick membranes with micrometer-sized pores [15, 16]. Here we find agreement between the formula and experiment for pnc-Si (Fig. 4.2C), indicating that continuum descriptions of fluids are appropriate for the analysis of flow through these nanometer thick membranes [16].

In Fig. 4.2D, we compare the hydraulic permeability of a pnc-Si membrane with a 12 nm average pore diameter to the permeabilities of carbon nanotube (CNT) membranes reported in the recent literature to give high flow rates [17, 18, 19, 20]. We also compare pnc-Si permeabilities to measurements for commercially available track-etched (TE) membranes assembled into the same centrifuge devices used for pnc-Si hydraulic permeability measurements. Direct comparisons between CNT, TE, and pnc-Si membranes are appropriate given that all three membranes have well-defined through-pores. Advances in manufacturing [21] allowed Yu *et al.* to create CNT membranes with 3 nm pores and $\sim 80\%$ porosity and achieve hydraulic permeability values of $3.3 \text{ cm}^3 \text{ cm}^{-2} \text{ min}^{-1} \text{ bar}^{-1}$ [20]. CNT membranes achieve high hydraulic permeabilities despite being thicker (2-200 μm) and having smaller pores (1-6 nm) than pnc-Si because the

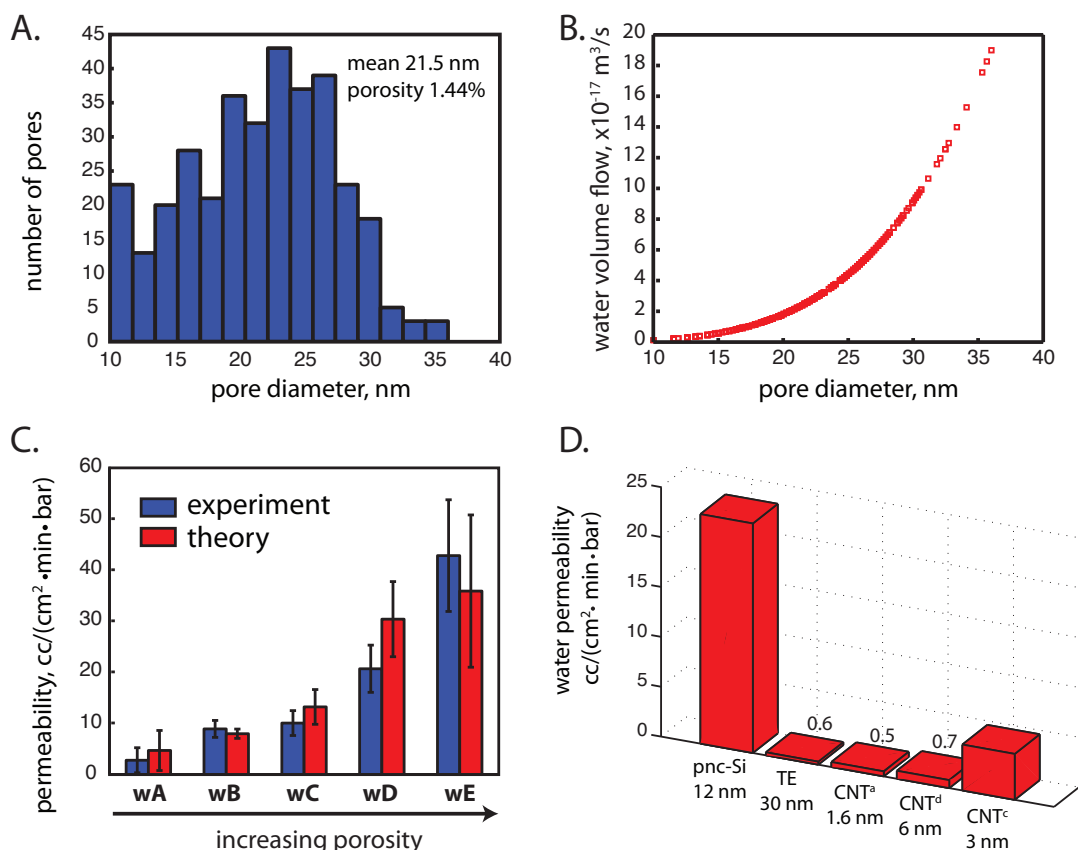


Figure 4.2: Experimental and theoretical water permeability **A.** Pore size distribution. The distribution was obtained from a transmission electron micrograph for a particular pnc-Si membrane. **B.** Pore-by-pore calculation of theoretical water flow rate through the membrane in **A**. The Dagan formula was used to calculate the flow through each pore identified in the TEM image. **C.** Experimental and theoretical hydraulic permeability. Membranes from five wafers (labeled wA through wE) were tested experimentally for hydraulic permeability using the device shown in Fig. 4.1C. Data for each wafer were grouped, and error bars reveal the standard deviations for these groups. The error for the theoretical permeability combines the two independent sources of error: processing error and image variability (see Supporting Information). For each wafer, the average porosity, average pore diameter, and number of contributing membranes are as follows: wA = 0.7%, 13.6 nm, $n = 4$; wB = 2.2%, 17.0 nm, $n = 2$; wC = 6.6%, 7.4 nm, $n = 6$; wD = 8.8%, 13.7 nm, $n = 6$; wE = 13.5%, 13.0 nm, $n = 3$. **D.** Water permeability of pnc-Si membranes is significantly higher than other nanoporous membranes. Experimentally obtained values for polycarbonate track-etched (TE) membranes agree with manufacturer claims. Data labels: (a) Holt et al. Science, 2006; (b) Yu et al., Nano Lett. 2009; (c) Majumder et al. Nature 2005. Note: all pore sizes are diameters.

smooth and hydrophobic nanotube walls allow fluids to slip [19, 22, 23]. Unlike CNT membranes, pnc-Si is hydrophilic and the assumption of no-slip, highly viscous flow agrees with measurement (Fig. 4.2). Still, the hydraulic permeability we measure for pnc-Si membranes with 1.4% porosity is 7 times higher than the highest porosity CNT membranes. Not surprisingly, we also found that the hydraulic permeability of pnc-Si membranes is ~ 35 -fold higher than 6 μm thick, hydrophilic TE membranes with slightly larger pore sizes (30 nm) and a 3-fold lower porosity ($\sim 0.5\%$ porosity). Indeed, the hydraulic permeability values we report for 15% porous pnc-Si ($\sim 40 \text{ mL cm}^{-2} \text{ min}^{-1} \text{ bar}^{-1}$) appear to be the highest on record for a nanoporous membrane (pores $< 100 \text{ nm}$), exceeding commercial ultrafiltration membranes ($\sim 2 \text{ mL cm}^{-2} \text{ min}^{-1} \text{ bar}^{-1}$) [24], high porosity nanoporous alumina ($\sim 1 \text{ mL cm}^{-2} \text{ min}^{-1} \text{ bar}^{-1}$) [25], experimental block copolymer membranes ($\sim 4 \text{ mL cm}^{-2} \text{ min}^{-1} \text{ bar}^{-1}$) [26], and 60 nm thick protein membranes ($\sim 15 \text{ mL cm}^{-2} \text{ min}^{-1} \text{ bar}^{-1}$) [6].

In our initial attempts to measure the hydraulic permeability of pnc-Si, we discovered that membranes are impermeable to water when one side of the membrane is left dry (Fig. 4.3). We explored several strategies to overcome water impermeability of the wet/dry configuration, including the use of high pressures ($> 1 \text{ atm}$), ozone treatment of membranes to decrease contact angles from $\sim 70^\circ$ to less than 15° (Fig. 4.6), and lowering surface tension 2-3-fold by adding surfactants (0.2 wt % SDS or 0.2 wt % Triton X-100) or using ethanol instead of water. We also switched from centrifuge-generated pressure to a simple pressure cell because we suspected centrifugal forces were quickly removing fluid droplets from the membrane backside and stopping flow. High water permeability was only observed when we immersed the membrane in water throughout the experiment or added a hygroscopic polymer, polyvinylpyrrolidone (PVP), to the membrane backside. The most reasonable explanation for impermeability of the wet/dry arrangements is that water cannot wick through the pores to wet the backside of a membrane. This is somewhat surprising given that capillary forces should easily drive water to fill 15 nm long hydrophilic pores. While we cannot confirm that the hydrophilic

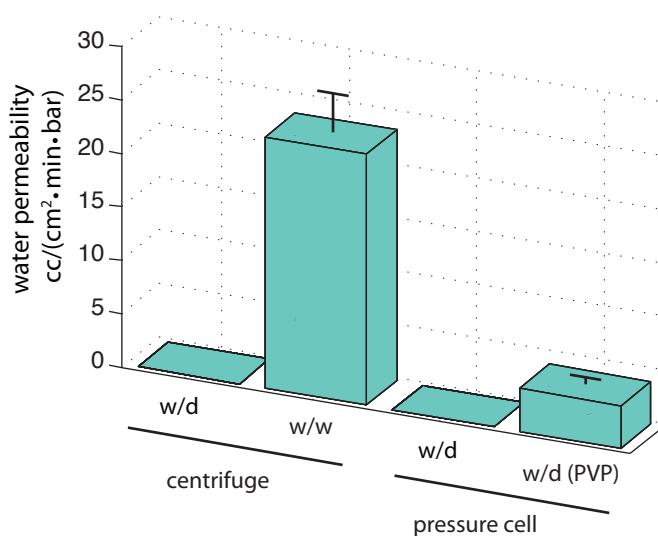


Figure 4.3: Pnc-Si membranes are impermeable in wet-dry configurations. Pnc-Si membranes were tested for hydraulic permeability in both a centrifuge and in a constant pressure cell. Membranes that are exposed to water on only side are not permeable to water at experimental pressures (0.1-1 bar), while membranes wetted on both sides have significant hydraulic permeability. Membranes coated with hygroscopic PVP were permeable to water when exposed to water on only one side. These samples had an initially lower flow rate, resulting in a lower time-averaged hydraulic permeability over the course of the experiment.

contact angles we measure on the top surface of pnc-Si chips also apply to pore walls, the fact that rapid transmembrane diffusion occurs when the membranes are immersed in water [12, 13] does suggest that water has no difficulty entering pores without applied pressure. Thus we suspect that the meniscus in a filled pore cannot advance around the obtuse angles at the pore exit under pressures compatible with pnc-Si membranes [12].

To examine the performance of pnc-Si membranes in size-exclusion separations, we filtered gold nanoparticles in a size ladder ranging between 5 and 30 nm in diameter. To avoid filtrate dilution from the immersing fluid in the centrifuge setup, we used a simple pressure cell for which flow could be initiated by the addition and removal of 5 μL of water to the membrane backside. The pressure cell was operated at 10 psi until it passed 100 μL of a 200 μL starting sample through membrane chips from three different wafers (F, G, H). Absorbance values in the retentate and filtrate were measured to

Table 4.1: Physical dimensions of protein in the size ladder

molecule	MW (intact, k)	structure	shape	size (nm)	reduced MW (k)
carbonic anhydrase	37	monomer	globular	4 ³⁸	37
ovalbumin	45	monomer	globular	6.5 ³⁹	45
albumin	67	monomer	globular	7.5 ⁴⁰	67
phosphorylase-b	19	homodimer	globular	8.3 ⁴¹	97
β -galactosidase	495	homotetramer	globular	17 ⁴²	116
myosin II heavy chain	400	homodimer	linear	160 \times 10 ⁴³	200

determine concentrations, and these were normalized to the starting concentration to calculate sieving coefficients. Results show that each pnc-Si membrane exhibited a sharp cut-off with negligible transmission of the larger particle and significant transmission (40-85%) of the smaller particle (Fig. 4.4A). Most notably, membranes from wafer F allow more than 80% transmission of 5 nm particles while fully blocking the larger 10 nm nanoparticle (Fig. 4.4A,B). Membranes from wafer G also exhibited a resolution of 5 nm, but a cut-off between 10 and 15 nm.

In contrast to pnc-Si, commercially available cellulose (MW cut-offs 3k and 100k) and PES membranes (MW cut-offs 3k, 30k, 50k, 100k) did not pass any nanoparticles between 5 and 30 nm. PES membranes with a reported MW cut-off of 300k did pass nanoparticles in this size range, although passage was clearly hindered as the particle size increased (Fig 4.4A). This result was surprising as the nominal pore size for 300k ultrafiltration membranes is expected to be \sim 18 nm [27, 28] and suggests the presence of a significant number of larger pores or defects in these high-flux membranes. We quantified losses by multiplying concentrations in the retentate and filtrate by the recoverable volumes in each compartment and compared this to the amount of starting material. For pnc-Si, losses were within the experimental uncertainty deriving from pipetting and measurement errors ($<5\%$), while losses were greater than 20% for the 300k PES membranes. Since no detectable quantities of nanoparticles passed into the filtrate and the PES membranes appeared pink after the experiment, the lost particles are presumably

Table 4.2: Stock nanoparticle sizes as determined by DLS and TEM

Manufacturer's Size (nm)	TEM Size (nm)	DLS Size (nm)
9.2 ± 0.9	7.8 ± 0.9 (STD)	9.7 ± 2.4 (STD)
15.2 ± 1.5	12.7 ± 0.9 (STD)	13.3 ± 3.4 (STD)

embedded in PES membranes. We also performed separation experiments on a protein size ladder containing globular proteins with the exception of a linear myosin control protein (Fig. 4.4D). Table 4.1 lists the unreduced and reduced sizes of the proteins used in the ladder. The unreduced sizes are relevant to the filtration process, while the reduced sizes are the molecular weights of monomers seen on the reducing gels. The results indicate complete retention of myosin and β -galactosidase (~ 17 nm) and a nearly undiluted transmission of the carbonic anhydrase (~ 4 nm). The transition between full transmission and full complete retention takes place between ovalbumin (~ 6.5 nm) and phosphorylase B (~ 8.3 nm), again suggesting a resolution of better than 5 nm for proteins as with nanoparticles.

Using dynamic light scattering, we confirmed that membranes from wafer G could be used to purify 10 nm particles from a mixture of 10 and 15 nm nanoparticles (Fig. 4.4C). Filtering a mixture of 10 and 15 nm stock largely recovers the light scattering profile of 10 nm nanoparticles with only a slight shift that presumably arises from some smaller particles in the 15 nm sample entering the filtrate. It is important to note that each nanoparticle stock is not perfectly monodisperse and that light scattering tends to broaden the distribution relative to the actual size of the nanoparticles. We established this by comparing the sizes of nanoparticles in the 10 and 15 nm stocks as measured by light scattering to the sizes of nanoparticles measured by electron microscopy (Table 4.2). Thus the purification of 10 nm particles from the 10 nm/15 nm mixture is implied by fact that the shifted spectrum of the filtered mixture closely resembles the original 10 nm spectrum.

High transmission of materials just below a cut-off is not typical of ultrafiltration

membranes [7, 29, 30] and may be enabled by the thinness of pnc-Si. Advanced sieving theories [31] demonstrate that diffusion can significantly boost the concentration of filtrate materials for ultrathin membranes compared to purely convective transport. The ratio of transport by convection versus diffusion is known as the Péclet number:

$$Pe = \frac{UL}{D} \quad (4.3.1)$$

where U is the average solvent velocity in a pore, L is the membrane thickness, and D is the diffusion coefficient of the species being transported. For 15 nm thick pnc-Si, $Pe \sim 0.1$, assuming a 4 nm monomeric protein ($D = 1 \times 10^{-6} \text{ cm}^2/\text{s}$) and a transmembrane velocity of 0.1 cm/s. By comparison $Pe \sim 3$ for filtration at similar velocities with a commercial ultrafiltration membrane having a 500 nm thick skin. In practice, hindrance from the membrane will increase Péclet numbers because the resistance to solute diffusion through a pore will be greater than the resistance to solute convection through a pore [32]. We estimate that a 12 nm pore would reduce the diffusion coefficient of a 4 nm protein ~ 6 -fold compared to free diffusion and increase Pe to ~ 0.7 for pnc-Si and to ~ 20 for conventional membranes. Thus, even after accounting for membrane resistance and despite high velocities within pores, diffusion is a significant contributor for molecularly thin membranes but not for conventional membranes.

The sieving function of pnc-Si is complex and will require more experimentation and advanced modeling to fully understand. For example, the nonlinear dependence of flow rates on pore size (Fig. 4.2B) makes the pore distribution effectively tighter and the cut-off sharper than implied by the physical pore size distribution. We illustrate this with a flow histogram in which we calculate the flow rate through each bin in the pore histogram in Fig. 4.2A (see Figure 4.7). This analysis shows that the smallest pores contribute very little to the bulk fluid transport and that the transition from the peak flow rates to the largest pore sizes occurs over ~ 5 nm rather than ~ 10 nm. We expect that the sharpness of this transition, rather than the breadth of the full pore distribution, is what

determines the resolution of the membrane in practice. The magnitude of the membrane cut-off is also not predicted from the physical pore distributions in a straightforward way. In the above experiments, gold nanoparticles were filtered in deionized water so that electrostatic repulsion between the negatively charged particles and the negatively charged membranes will reduce the effective pore sizes. In the case of protein filtration, adsorption is an additional factor known to reduce pore sizes by the thickness of a protein monolayer [12].

It is important to emphasize that while manufacturing is currently limited to making small membrane devices, the use of highly scalable semiconductor manufacturing allows large numbers of those devices to be made. The membranes used for the current work were produced on 4 inch wafers that contained more than 80 membrane chips. Continued optimization of manufacturing and chip design since the completion of this work is now resulting in more than 400 similar devices being produced on a 6 inch wafer at less than twice the cost (Fig. 4.8). Similarly, while the membranes used in the current work were limited to $\sim 1\%$ active membrane area, which is sufficient to characterize the intrinsic properties of the material, advances in manufacturing are now producing membranes with $\sim 10\%$ active area, which increases the total volumetric flow to $\sim 500 \mu\text{L}/\text{min}$ at 1 atm of pressure. Continued advances in manufacturing, including the use of [110] crystalline silicon to allow vertical etches through the support wafer (rather than the [100] silicon currently used), should allow the fraction of chip area occupied by free-standing membrane to increase at least another 4-fold. Since only standard semiconductor manufacturing processes are used in the production of pnc-Si, the volume of wafers produced each day is also highly scalable. Thus, while the prospects for scaled-up manufacturing of many of the nanoengineered membranes appearing in the literature are dim, large-scale manufacturing is very realistic and partially achieved already for pnc-Si.

The high hydraulic permeability, sharp size discrimination, scalable fabrication, and low loss characteristics of pnc-Si membranes suggest their immediate use in the purifi-

cation and production of nanoscale materials. For example, the cut-offs demonstrated here (5-30 nm) can be useful for purifying monomeric proteins from oligomers or for isolating monovalent quantum dots from multivalent dots that induce cross-linking in biological samples [33]. The membranes might also be used for the fractionation of nanoparticles from polydisperse mixtures emerging from batch production [34]. Other membrane-based techniques for high-resolution fractionation of nanoparticles do exist but have important limitations. Hutchison and co-workers purified 1.5 nm gold from a mixture including 3.1 nm gold using commercial ultrafiltration membranes and a diafiltration scheme that resulted in a 15-fold dilution of the smaller species [35]. Dead-end filtration with experimental graft [36] and block [26] copolymer membranes has been shown to provide high-resolution (~ 5 nm) size discrimination of nanoparticles; however, the pore sizes of these membranes are extremely sensitive to solvent conditions. In contrast, pnc-Si provides high-resolution separations with little dilution of the filtrate and a solvent-independent membrane structure. In a sophisticated process involving buffer and flow optimization, van Reis and colleagues were able to use commercial ultrafiltration membranes in a two-stage, recirculating, tangential flow filtration scheme to separate protein monomers and oligomers with high yield and low dilution [37]. While there is still much to learn about the sieving function of pnc-Si, pnc-Si and other ultrathin membranes hold promise for achieving similar performance characteristics with simpler filtration schemes.

4.4 Methods

4.4.1 Hydraulic Permeability of Pnc-Si.

Custom polypropylene centrifuge housings were designed to hold round formatted silicon chips and were mass-produced by Harbec Inc. (Ontario, NY). Devices were hand assembled by pressing a polypropylene retention ring against a pnc-Si chip and a 5 mm Viton O-ring placed at the base of the housing. The assembled devices and a

round-bottom 10 mL test tube were both weighed before the experiment.

In wet/wet experiments, 500 μL of distilled and deionized water was added to both the insert and the test tube. Before inserting the device into the centrifuge tube, a 30 μL droplet of water from the tube was added to the backside of the membrane to prevent an air bubble from forming beneath the membrane during immersion. The top of the centrifuge tube was sealed to prevent evaporation, and the tube was placed in a centrifuge and spun for 30-60 min at 75 rcf. After the experiment was finished, the insert was removed from the test tube. Any remaining water on the backside of the insert was removed and added back into the tube. The tube and insert final weights were subtracted from initial values to determine the volume of water in each. In most experiments, 100-200 μL of deionized water passed through the membrane over the course of 30-60 min of centrifugation. Control experiments with broken membranes gave hydraulic permeability values at least one order higher than those measured for intact pnc-Si, and control experiments with solid silicon frames detected no leaks.

In order to generate fluid flow without membrane immersion, we treated the membrane backside with polyvinylpyrrolidone (PVP, Sigma Aldrich, St. Louis, MO). Three microliters of 1 mg/mL PVP in methanol (w/v) was pipetted onto the backside of a membrane. The membrane was allowed to dry for a minimum of 2 h under ambient conditions. The membrane was assembled into the pressure cell with 500 μL of deionized water in the feed tube. The pressure was held constant at 3 psi for 30 min, and the water on the backside was collected and measured on a balance. Initial flow rates were low, likely due to a delay in the wetting process. This could explain the low calculated hydraulic permeability values for PVP-treated membranes compared to wet/wet format. After these experiments with PVP confirmed that the difficulty with wet/dry configuration was the lack of wetting on the membrane backside, we found that adding and removing droplets of water from the backside without PVP could be used to initiate flow in the pressure cell, although again the flow did not immediately rise to its peak values. For these reasons, we preferred the centrifuge setup for hydraulic permeability

studies. On the other hand, the pressure cell provided an advantage for separation studies because it did not require an immersing fluid that results in filtrate dilution. We verified that the flow of DI water through the pnc-Si membranes in the pressure cell was time-independent (Fig. 4.9).

4.4.2 Hydraulic Permeability of Track-Etched Membranes.

Commercially available polycarbonate track-etched membranes (Sterlitech) were cut into circular discs with a diameter of 0.70 cm (0.38 cm² area) using a custom pressure die. In order to test the hydraulic permeability of these membranes in a centrifuge setup, centrifuge filter units from Millipore (Microcon) were disassembled with slight application of pressure. The regenerated cellulose membranes were replaced with the previously cut polycarbonate track-etched membranes, and the Microcon devices were then reassembled. Centrifugation was performed with the same initial pressures as in the pnc-Si experiments for between 10 and 30 min. Graphs of volume passed through the membrane over time were created, and the hydraulic permeability was calculated from the extrapolated initial slope of these curves.

4.4.3 Membrane Production.

Pnc-Si membranes were fabricated as previously described [12]. Briefly, a 1000 thermal oxide was grown on both sides of a (100) N-type silicon wafer. The backside of the wafer was patterned using photolithography in order to form an etch mask for the nanocrystalline membranes. After lithography, the front side oxide was removed. A three-layer silicon dioxide (20 nm)/amorphous silicon (15 nm)/silicon dioxide (20 nm) film stack was then deposited onto the bare silicon wafer by RF magnetron sputtering (AJA International, North Scituate, MA). The deposition rates for the silicon dioxide and amorphous silicon layers are well-characterized [12]. Pores were formed by inducing a phase transition in the silicon layer from an amorphous to nanocrystalline state using a rapid thermal annealing process ranging from 850 to 1100 C (Surface Science Integration,

El Mirage, AZ). The membrane was released by etching the backside of the silicon wafer with a preferential silicon etchant, ethylenediamine pyrocatechol (EDP). Due to its high silicon to oxide etch selectivity, the EDP etch terminated at the first protective oxide layer in the membrane film stack. Finally, the protective oxide layers were etched with buffered oxide etchant (BOE), thus exposing the porous nanocrystalline silicon membrane. The mask was designed to yield 84 samples per silicon wafer. Each sample contained two $2000\ \mu\text{m} \times 100\ \mu\text{m}$ slits with free-standing 15 nm thick pnc-Si membranes.

4.4.4 Electron Microscopy.

Plan-view transmission electron microscopy of pnc-Si membranes was performed in bright-field mode at 80 kV using a Hitachi H-7650 transmission electron microscope (TEM). Membranes were formatted on each wafer to be compatible with the TEM specimen holder. Images were acquired with an Olympus Cantega 11 megapixel digital camera.

4.4.5 Pore Image Processing and UV/Ozone Treatments.

See legends of Supporting Information Fig. 4.5 and 4.6.

4.4.6 Gold Nanoparticle Filtration.

Stock solutions (0.01% w/v) of gold nanoparticles (British BioCell International, Cardiff, UK) were diluted 1:1 with ddH₂O. Two hundred microliters of diluted gold was placed in assembled plastic housings with pnc-Si membranes and pressurized to 10 psi using a pressure cell described above. Pressure was maintained until approximately one-half of the volume passed through the membranes (typically 5-15 min). The retentate and filtrate solutions were recovered and weighed to determine total volume recovery, which was typically 198 μL . The retentate solution was pipetted up and down against the membrane five times to maximize recovery of gold that had settled against the membrane. The peak absorbance between 500 and 550 nm of the retentate and filtrate was

measured on a NanoQuant plate using a Tecan plate reader (Tecan Group, Männedorf, Switzerland) and compared to stock solution peak values. Using the volume and concentrations of the retentate and filtrate, percent nanoparticle recovery was calculated. To perform a separation of 10 and 15 nm gold (Fig. 4.4C), equal parts of stock solutions were mixed without ddH₂O dilution.

Pall Nanosep filtration devices with PES membranes (Pall, Port Washington, NY) were tested in our pressure cell using a similar approach. Two hundred microliters of diluted gold was pressurized at 10 psi until approximately one-half of the volume passed through the filter. Like with pnc-Si membranes, the retentate solution was recovered by pipetting up and down against the membrane five times to maximize recovery. In most cases, a light pink color remained in the membrane even after vigorous pipetting, likely accounting for the reduced recovery percentages compared to pnc-Si.

Millipore Microcon filtration devices with cellulose membranes (Millipore, Billerica, MA) were also tested, but since Millipore devices could not easily be adapted to our pressure cell, separation experiments were performed in a fixed rotor centrifuge at 14,000 *ref* according to manufacturers instructions. All of the cellulose membranes tested (3k, 30k, 50k, and 100k rated molecular weight cut-off) retained all of the gold species.

4.4.7 Protein Separations.

One hundred microliters of a 1 mg/mL total protein mixture containing myosin, β -galactosidase, phosphorylase B, albumin, ovalbumin, and carbonic anhydrase in PBS was loaded into the plastic housing and pressurized at 2 psi for 40 min. The backside of the membrane was prewet with 10 μ L of PBS to initiate flow. Ten microliters of the filtrate was removed from the backside of the membrane and prepared for SDS-PAGE along with the starting solution and remaining feed solution (retentate). Silver stain was used to visualize proteins on the completed gels. The molecular weight and other physical properties of the proteins are given in Table 4.1. Note that the MW of the nonreduced (intact) molecules being filtered is different than the MW shown on the

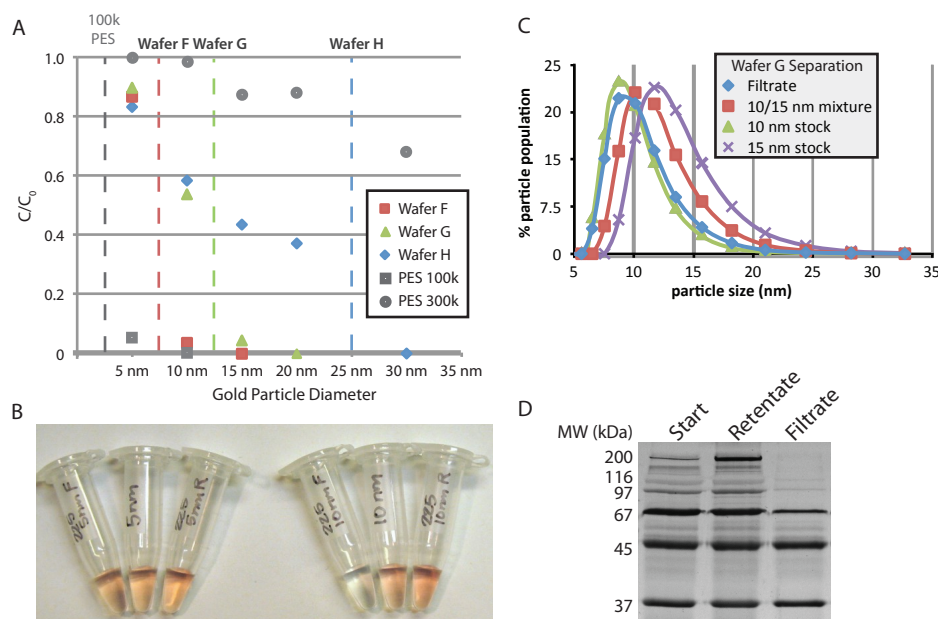


Figure 4.4: UV ozone treatment increases membrane hydrophilicity. **A.** Filtration of gold nanoparticles in a 5–30 nm size ladder. Gold nanoparticle solutions (0.01% solids) were filtered through three different pnc-Si membranes and one commercial PES membrane. Absorbance readings were used to calculate the nanoparticle concentrations and losses. The figure shows the ratio of concentrations in the filtrate vs feed solutions as a function of nanoparticle size. Dashed lines are the apparent cut-off for each wafer. **B.** Images of stock, retentate, and filtrate solutions for separations with wafer F. Tubes are labeled with particle size and R for retentate, F for filtrate. Stock particles are in the center with no letter designation. **C.** Purification of 10 nm particles from a mixture of 10 and 15 nm particles using wafer G. Dynamic light scattering spectra of 15 nm stock gold nanoparticles (black), 10 nm stock (blue), the starting solution containing equal concentrations of 10 and 15 nm particles (green), and the filtrate (red). **D.** Fractionation of a protein mixture by SDS-PAGE. The protein size ladder contains six proteins with distinct molecular weights ranging from 37k to 400k when the proteins are in their native state (see Supporting Information for details on protein structure and sizes).

reducing gel in Fig. 4.4D. Sizes are approximate based on crystal dimensions with the exception of myosin, which is taken from EM data.

4.5 Supplemental Methods and Figures

4.5.1 Analysis of hydraulic permeability in the wet/wet configuration

From a simple mass balance analysis the governing equation for the water volume transfer in the wet/wet format can be derived as

$$P = - \frac{\ln \frac{V_{cup}(t) - V_{cup,EQ}}{V_{cup,0} - V_{cup,EQ}}}{(t)\rho_w g \left[1 + \frac{A_{cup}}{A_a} \right]} \quad (4.5.1)$$

where P is the hydraulic permeability of the membrane, ρ_w is the density of water, g is the centrifugal acceleration calculated for the membrane position in the centrifuge, $V_{cup,0}$ is the initial volume of water in the interior cup obtained prior to centrifugation, $V_{cup}(t)$ is the volume of water in the interior cup at a later time t , and $V_{cup,EQ}$ is the equilibrium volume of water in the cup obtained from extended spins or from control runs using intentionally broken membranes. The cross sectional area of the cup, A_{cup} , and the annular cross section between the cup and the outer tube area A_a were calculated based on the dimensions of the two devices.

For cases such as pnc-Si where the active membrane material does not span the entire cross section interior cup, the formula above must be multiplied by the additional factor of A_{cup}/A_m , where A_m is the active membrane area. The active membrane area of chips used was estimated by light microscopy and a typical value was 0.0032 cm^2 . The cup area and annulus areas were 0.394 cm^2 and 0.925 cm^2 respectively. Note that the use of active area in hydraulic permeability calculations rather than total chip area is appropriate to determine the intrinsic behavior of the nanomaterial and avoid device-dependent values. This was also the approach for example, taken by Holt *et al.* [19] to calculate the hydraulic permeability of CNT membranes created as small active

areas on otherwise impermeable silicon chips. Expanding the amount of active area on pnc-Si chips is an engineering challenge that is being met with steady improvements in etching, patterning, and deposition processes. Fig. 4.8d shows the results of some of these improvements have led to new chip designs that have 10 times more active area than the device shown in Fig. 4.1c.

The Dagan equation [14] for flow through short pores used to predict flow through pnc-Si is given by:

$$Q_{\text{liquid}} = \frac{R_p^3 \Delta P}{\mu \left[3 + \frac{8}{\pi} \left(\frac{L}{R_p} \right) \right]} \quad (4.5.2)$$

where R_p is the average pore radius, ΔP is the pressure drop across the membrane, L is the membrane thickness and μ is the solution viscosity. This equation becomes the familiar Hagen-Poiseuille equation in the limit that L/R_p becomes large.

4.5.2 Estimate of uncertainty in predicted hydraulic permeability

Predictions of hydraulic permeability through pnc-Si membranes derived some uncertainty from the use of pore distributions from TEM images of actual membranes in calculations. There were two main sources of error in these calculations. First, the identification of pores in the pore image processor program varied slightly between users. Second, images only capture a small section of the membrane and so the histograms for individual fields on the same membrane varied to some degree. Calling these uncertainties σ_{user} and σ_{membrane} respectively, and assuming they are independent contributors to the overall uncertainty, σ_{all} , we can write $(\sigma_{\text{all}})^2 = (\sigma_{\text{user}})^2 + (\sigma_{\text{membrane}})^2$. We developed systematic tests to estimate each of these uncertainties and determine σ_{all} for Fig. 4.2d. σ_{user} was found by having four different qualified users operate the pore processing program and evaluate the pore characteristics of the five types of membranes presented in Fig. 4.2d. σ_{membrane} was found by having one user evaluate a set of TEM images from different fields of view for each of the five membrane types.

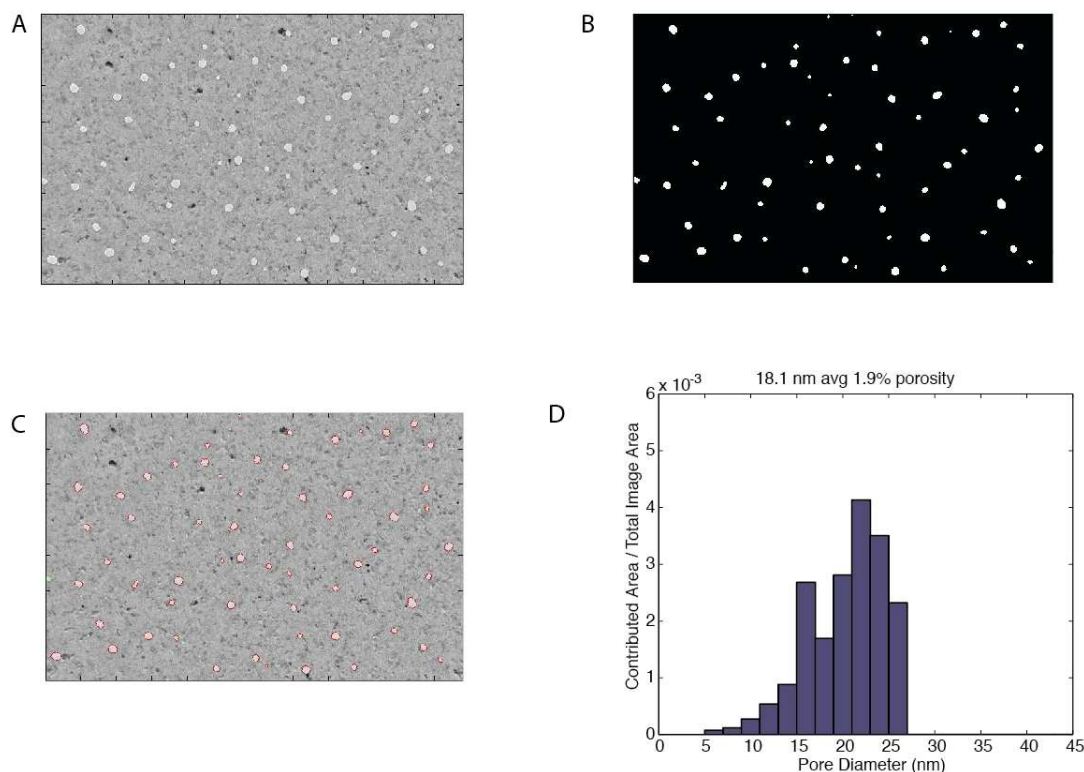


Figure 4.5: Pore processing of TEM images. We use a custom image processing program written in MATLAB to analyze pore characteristics of pnc-Si membrane TEM images. **A.** We first perform background correction by subtracting the average value from a local region of defined size from each pixel. We use a local region that is bigger than the size of the pores, but smaller compared to any light variations in the background. **B.** The image is transformed into a black and white image using a threshold value. The threshold value is chosen so that most pore pixels have an intensity value higher than the threshold and background pixels mostly fall below. Values higher than the threshold are white in the new binary image, and those below the threshold are black. Combinations of binary operations are then used to remove artifacts and better define pores in the image before finding the final statistics. An erode operation is used to shrink white areas within neighboring black areas, and a dilate operation is used to grow white areas. Erosions followed by dilations can remove noise and small artifacts from the image while retaining pores. Dilations followed by erosions can be used to fill in pores with inner regions below the threshold. The selection of these operations will vary depending on the image, and leads to user-to-user variability which we have quantified. **C.** Pore edges are identified and pore statistics, including diameters, pore areas, and porosity, are found. **D.** Pore distributions are typically found by plotting the contributed area for each pore diameter. Average diameter and porosity are indicated above the plot. The pore image processing routines are freely available at <http://nanomembranes.org/resources/software/>

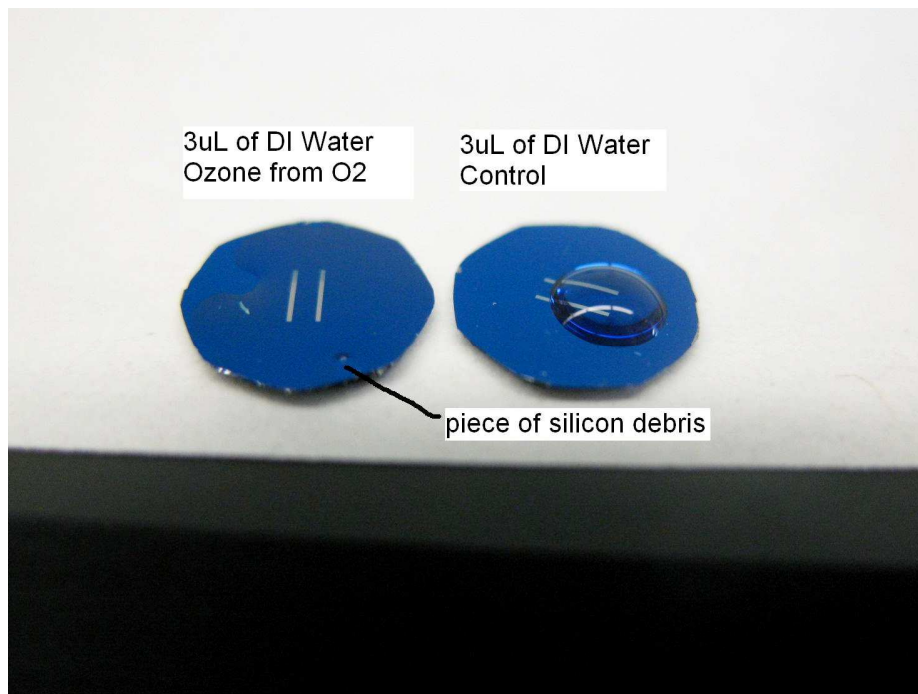


Figure 4.6: UV ozone treatment increases membrane hydrophilicity. In the effort to develop wet/dry hydraulic permeability we treated pnc-Si membranes with Novascan PSD-UVT UV/ozone system. Membranes were exposed to three minutes of oxygen at 50C followed by three minutes of UV treatment at 50C. The membranes were undisturbed in the chamber for 15 more minutes to allow the ozone react with the samples. Both figures show 3 μ L droplets of DI water. The fluid is so flat on the treated sample that it is hard to discern, except for the disturbance of the water layer caused by a small piece of debris.

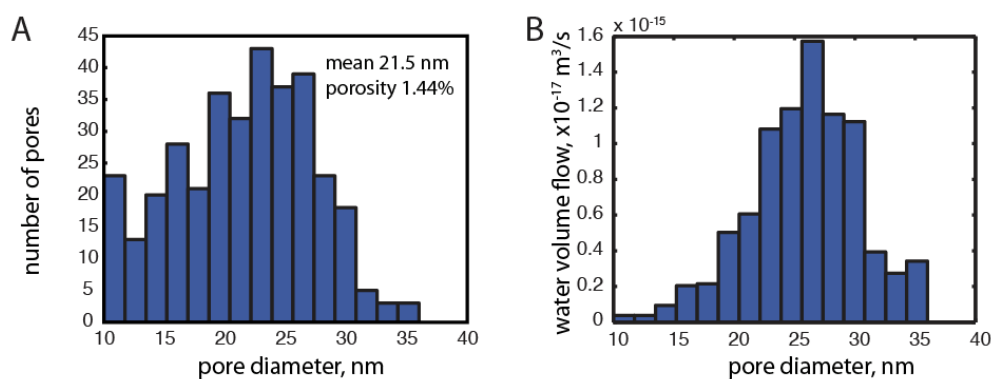


Figure 4.7: Flow sharpens the effective pore distribution. In panel **B** we have calculated the predicted flow through each of the bins in the pore size histogram in **A** (panel **A** is a repeat of Fig. 4.2A). The non-linear influence of flow on pore size reduces the influence of small pores and shortens the transition from maximum to minimum values on the right side of the histogram (sharper cut-off).

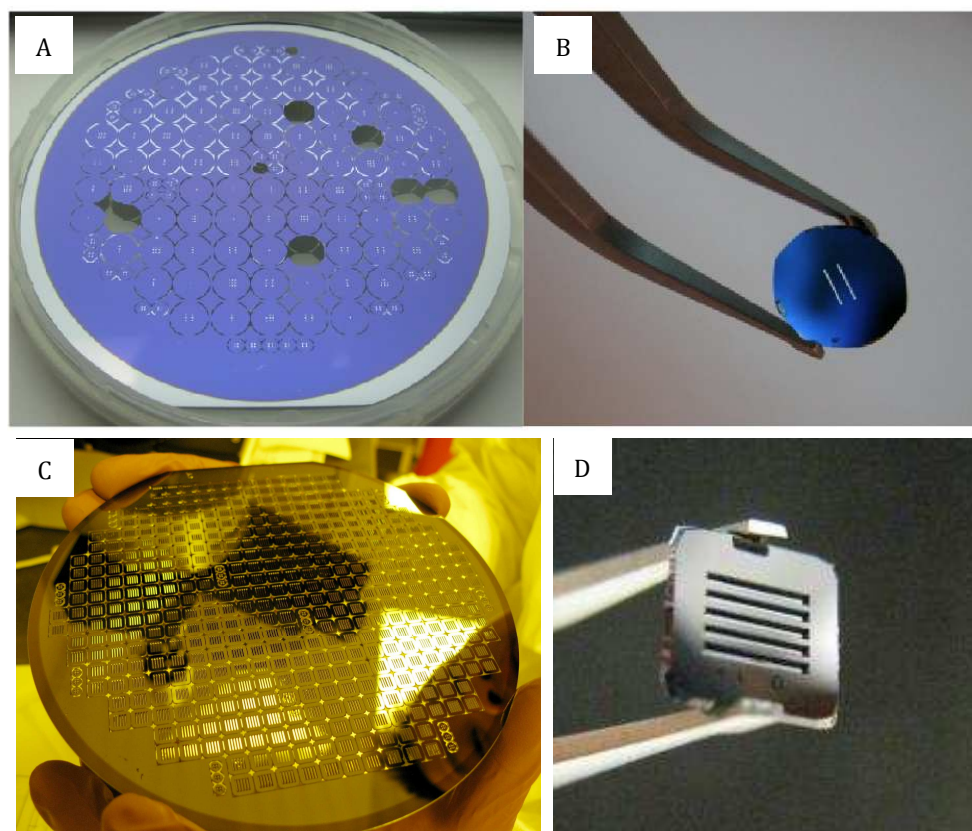


Figure 4.8: Pnc-Si membrane fabrication is highly scalable. **A.** Many pnc-Si membrane chips can be made per individual wafer, and this particular 4" wafer, left, has 84 chips formatted for centrifuge tubes and 46 smaller TEM grid chips. **B.** Pnc-Si chips are detached from the wafer by applying light pressure to the edges of the chips. **C.** Pnc-Si production has recently been scaled from 4 wafers to 6 and from round to square formats allowing more than 400 membrane devices with high active area to be produced with only marginally more cost compared to 4" wafers. **D.** Improved chip design now allows 10% of total chip area to be covered with active membrane, approximately 10x more membrane area than the chip shown in **C**.

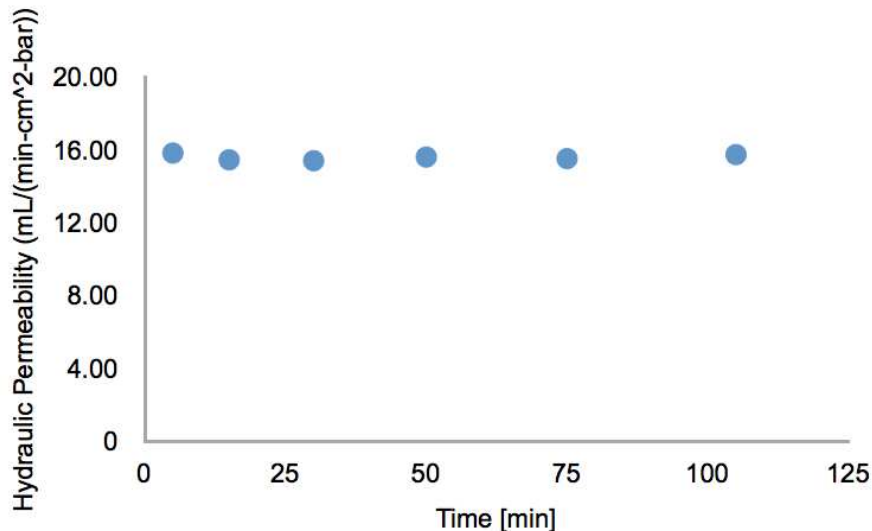


Figure 4.9: Hydraulic permeability of pnc-Si is time-independent. Distilled and deionized water was forced through a pnc-Si membrane in the pressure cell for over two hours and passed volumes were collected at the times shown to calculate an ‘instantaneous hydraulic permeability.

4.6 References

- [1] R. Ghosh, Protein Separation Using membrane chromatography: opportunities and challenges, *J. Chromatogr. A* **952**, 12-27 (2002).
- [2] B.V. Bhut, S. Husson, Dramatic performance improvement of weak anion-exchange membranes for chromatographic bioseparations, *J. Membr. Sci.* **337**, 215-223 (2009).
- [3] B. V. Bhut, S.R. Wickramasinghe, S. Husson, Preparation of high-capacity, weak anion-exchange membranes for protein separations using surface-initiated atom transfer radical polymerization, *J. Membr. Sci.* **325**, 176-183 (2008).
- [4] R. Ghosh, Rapid antibody screening by membrane chromatographic immunoassay technique, *J. Chromatogr. B* **844**, 163-167 (2006).

- [5] Y. Wang, B.M. Balgley, P.A. Rudnick, E.L. Evans, D.L. DeVoe, C.S. Lee, Integrated capillary isoelectric focusing/ nano-reversed phase liquid chromatography coupled with ESI-MS for characterization of intact yeast proteins, *J. Proteome Res.* **4**, 36-42 (2005).
- [6] X. Peng, J. Jin, Y. Nakamura, T. Ohno, I. Ichinose, Ultrafast permeation of water through protein-based membranes, *Nat. Nanotechnol.* **4**, 353-357 (2009).
- [7] M. Cheryan, *Ultrafiltration Handbook* (Technomic Publishing Co: Lancaster, PA, 1986).
- [8] C.R. Martin, Z. Siwy, Molecular filters: pores within pores, *Nat. Mater.* **3**, 284-295 (2004).
- [9] W.H. Fissell, A. Dubnisheva, A.N. Eldridge, A.J. Fleischman, A.L. Zydney, S. Roy, High-performance silicon nanopore hemofiltration membranes, *J. Membr. Sci.* **326**, 58-63 (2009).
- [10] H. Tong, H. Jansen, V. Gadgil, C. Bostan, E. Bereschot, C. van Rijn, M. Elwenspoek, Silicon nitride nanosieve membrane, *Nano Lett.* **4**, 283-287 (2004).
- [11] I. Vlassiouk, P.Y. Apel, S.N. Dmitriev, K. Healy, Z.S. Siwy, Versatile ultrathin nanoporous silicon nitride membranes, *Proc. Natl. Acad. Sci. U.S.A.* **106**, 21039-21044 (2009).
- [12] C.C. Striemer, T.R. Gaborski, J.L. McGrath, P.M. Fauchet, Charge- and size-based separation of macromolecules using ultrathin silicon membranes, *Nature* **445**, 749-753 (2007).
- [13] E. Kim, H. Xiong, C.C. Striemer, D.Z. Fang, P.M. Fauchet, J.L. McGrath, S. Amemiya, A structure-permeability relationship of ultrathin nanoporous silicon membrane: a comparison with the nuclear envelope, *J. Am. Chem. Soc.* **130**, 4230-4231 (2008).

- [14] Z. Dagan, S. Weinbaum, R. Pfeffer, An infinite-series solution for the creeping motion through an orifice of finite length, *J. Fluid Mech.* **115**, 505-523 (1982).
- [15] S. Dushman, *Scientific Foundations of Vacuum Technique* (Wiley, New York, ed. 2, 1962).
- [16] R. Kusmanto, E. Jacobsen, B. Finlayson, B. Applicability of continuum mechanics to pressure drop in small orifices, *Phys. Fluids* **16**, 4129-4134 (2004).
- [17] B.J. Hinds, N. Chopra, T. Rantell, R. Andrews, V. Gavalas, L.G. Bachas, Aligned multiwalled carbon nanotube membranes, *Science* **303**, 62-65 (2004).
- [18] M. Majumder, N. Chopra, R. Andrews, B.J. Hinds, Nanoscale hydrodynamics: enhanced flow in carbon nanotubes, *Nature* **438** 44 (2005).
- [19] J.K. Holt, H.G. Park, Y. Wang, M. Stadermann, A.B. Artyukhin, C.P. Grigoropoulos, A. Noy, O. Bakajin, Fast mass transport through sub-2-nanometer carbon nanotubes, *Science* **312**, 1034-1037 (2006).
- [20] M. Yu, H.H. Funke, J.L. Falconer, R.D. Noble, High density, vertically-aligned carbon nanotube membranes, *Nano Lett.* **9**, 225-229 (2009).
- [21] D.N. Futaba, K. Hata, T. Yamada, T. Hiraoka, Y. Hayamizu, Y. Kakudate, O. Tanaike, H. Hatori, M. Yumura, S. Iijima, Shape-engineerable and highly densely packed single-walled carbon nanotubes and their application as super-capacitor electrodes, *Nat. Mater.* **5**, 987-994 (2006).
- [22] G. Hummer, J.C. Rasaiah, J.P. Noworyta, Water conduction through the hydrophobic channel of a carbon nanotube, *Nature* **414**, 188-190 (2001).
- [23] V.P. Sokhan, D. Nicholson, N. Quirke, Transport properties of nitrogen in single walled carbon nanotubes, *J. Chem. Phys.* **120**, 3855-3863 (2004).
- [24] Millipore Corporation, Product Selection Guide: Ultrafiltration Selection Guide, 2008, available at <http://www.millipore.com/techpublications/tech1/Pf1172en00>

- [25] A. Thormann, N. Teuscher, M. Pfannmöller, U. Rothe, A. Heilmann, Nanoporous aluminum oxide membranes for filtration and biofunctionalization, *Small* **3**, 1032-1040 (2007).
- [26] F. Schacher, M. Ulbricht, A. Muller, Self-supporting, double stimuli-responsive porous membranes from polystyrene-block-poly(N,N-dimethylaminoethyl methacrylate) diblock copolymers, *Adv. Funct. Mater.* **19**, 1040-1045 (2009).
- [27] D.R. Latulippe, K. Ager, A.L. Zydney, Flux-dependent transmission of supercoiled plasmid DNA through ultrafiltration membranes, *J. Membr. Sci.* **294**, 169-177 (2007).
- [28] D.R. Latulippe, A.L. Zydney, Salt-induced changes in plasmid DNA transmission through ultrafiltration membranes, *Biotechnol. Bioeng.* **99**, 390-398 (2008).
- [29] L. Zeman, M. Wales, *Polymer Solute Rejection by Ultrafiltration Membranes. In Synthetic Membranes* Turbak, A. F., Ed. (American Chemical Society, Washington, DC, 1981) vol. 2.
- [30] A.S. Michaels, Analysis and prediction of sieving curves for ultrafiltration membranes: a universal correlation, *Sep. Sci. Technol.* **15**, 1305-1322 (1980).
- [31] S. Mochizuki, A.L. Zydney, Theoretical analysis of pore size distribution effects on membrane transport, *J. Cell Sci.* **82**, 211-227 (1993).
- [32] P. Dechadilok, W. Deen, Hindrance factors for diffusion and convection in pores, *Ind. Eng. Chem. Res.* **45**, 6953-6959 (2006).
- [33] M. Howarth, W. Liu, S. Puthenveetil, Y. Zheng, L.F. Marshall, M.M. Schmidt, K.D. Wittrup, M.G. Bawendi, A.Y. Ting, Monovalent, reduced-size quantum dots for imaging receptors on living cells, *Nat. Methods* **5**, 397-399 (2008).

- [34] B. Yen, N. Stott, K. Jensen, M.A. Bawendi, Continuous-flow microcapillary reactor for the preparation of a size- series of CdSe nanocrystals, *Adv. Mater.* **15**, 1858-1862 (2003).
- [35] S. Sweeny, G. Woehrle, J. Hutchinson, Rapid purification and size separation of gold nanoparticles via diafiltration, *J. Am. Chem. Soc.* **128**, 3190-3197 (2006).
- [36] A. Akthakul, A. Hochbaum, F. Stellacci, A. Mayes, Size fractionation of metal nanoparticles by membrane filtration, *Adv. Mater.* **17**, 532-535 (2005).
- [37] R. van Reis, S. Gadam, L.N. Frautschy, S. Orlando, E.M. Goodrich, S. Saksena, R. Kuriyel, C.M. Simpson, S. Pearl, A.L. Zydney, High performance tangential flow filtration, *Biotechnol. Bioeng.* **56**, 71-82 (1997).
- [38] R. Saito, T. Sato, A. Ikai, N. Tanaka, Structure of bovine carbonic anhydrase II at 1.95 resolution, *Acta Crystallogr., Sect. D* **60**, 792-795 (2004).
- [39] P.E. Stein, A.G. Leslie, J.T. Finch, R.W. Carrell, Crystal structure of uncleaved ovalbumin at 1.95 resolution, *J. Mol. Biol.* **221**, 941-959 (1991).
- [40] S. Sugio, A. Kashima, S. Mochizuki, M. Noda, K. Kobayashi, Crystal structure of human serum albumin at 2.5 resolution, *Protein Eng.* **12**, 439-446 (1999).
- [41] M. Gregoriou, M.E. Noble, K.A. Watson, E.F. Garman, T.M. Krulle, C. de la Fuente, G.W. Fleet, N.G. Oikonomakos, L.N. Johnson, The structure of a glycogen phosphorylase glucopyranose spirohydantoin complex at 1.8 resolution and 100 K: the role of the water structure and its contribution to binding, *Protein Sci.* **7**, 915-927 (1998).
- [42] D.H. Juers, R.H. Jacobson, D. Wigley, X.J. Zhang, R.E. Huber, D. E. Tronrud, B.W. Matthews, High resolution refinement of β -galactosidase in a new crystal form reveals multiple metal-binding sites and provides a structural basis for α -complementation, *Protein Sci.* **9**, 1685-1699 (2000).

-
- [43] A. Elliott, G. Offer, K. Burridge, Electron microscopy of myosin molecules from muscle and non-muscle sources, *Proc. R. Soc. London, Ser. B* **193**, 45-53 (1976).

Chapter 5

Electroosmosis[†]

5.1 Abstract

We have developed and tested low voltage electroosmotic pumps (EOPs) fabricated from 15 nm thin porous nanocrystalline silicon (pnc-Si) membranes. Electroosmotic flow rates of $2.6 \times 10^2 \text{ mL min}^{-1} \text{ cm}^{-2} \text{ V}^{-1}$ are demonstrated, which are at least three orders of magnitude higher than previous EOPs. Close agreement is observed between the experimental flow rates and theoretical calculations. We attribute the high flow rates to high electrical fields across the ultrathin membranes, estimated to be $\sim 8 \times 10^5 \text{ V/m}$. The surface of pnc-Si membranes can be modified by plasma oxidation or silanization, which respectively raises or lowers the zeta potential and electroosmotic flow rates. The silicon-based platform of pnc-Si membranes enables straight-forward integration into devices. The intrinsic efficiency of pnc-Si as an electroosmotic pump represents a new opportunity for ultralow voltage on-chip pumping and highly portable microfluidic devices.

[†]Adapted from: J.L. Snyder, D.Z. Fang, T.R. Gaborski, C.C. Striemer, P.M. Fauchet, J.L. McGrath, High performance, low voltage electroosmotic pumps with molecularly thin nanoporous silicon membranes, *Proc. Natl. Acad. Sci.* Submitted.

5.2 Introduction

Electroosmotic flow results from the interaction between an electric field and the diffuse layer of ions at a charged surface. In capillaries or pores, the migration of the diffuse layer toward the oppositely charged electrode causes the bulk fluid within the channel to flow through viscous drag. Electroosmotic pumps (EOPs) are designed to generate high flow rates in microchannels using these principles [1, 2]. EOPs present a number of advantages over mechanical pumps, including the lack of mechanical parts, pulse free flows, and ease of control through electrode actuation. EOPs have been suggested as pumps for cooling circuits [3] and microfluidic devices that aid in drug delivery [4, 5] or diagnostics [2, 6]. Microfluidic devices enable the miniaturization of multi-step laboratory processes into small, low cost, disposable units [7, 6]. The inclusion of multiple steps into a single device increases the need for the precision pumping of fluids on-chip.

High voltages (> 1 kV) are often required for EOPs to achieve sufficient flow rates in microchannels [8, 9]. However, devices with high voltage EOPs require bulky external power supplies and a skilled technician to operate, which defeats the ease of use and portability aims of a microfluidic diagnostic tool. For these reasons, the development of a low-voltage EOP is a current focus in the literature. Several recent low-voltage EOPs have been fabricated from porous silicon and alumina [10, 11, 12, 13] and are much thinner than their high voltage predecessors (60 - 350 μm compared to > 10 mm). Yao *et al.* suggest that further thinning of EOPs will enable better voltage specific characteristics [14]. Here we examine the electroosmotic pumping by nanoporous membranes that are more than two orders of magnitude thinner than any membrane material previously used in an EOP.

We have recently developed an ultrathin (15-30 nm), nanoporous membrane material, called porous nanocrystalline silicon (pnc-Si) [15]. Pnc-Si membranes are fabricated on silicon wafers using techniques standard to the microelectronics industry. The sili-

con platform enables control of freestanding membrane area (Fig. 5.1a) and industrial scale manufacturing [16]. Pore distributions are controlled by fabrication temperatures and ramp rates during a nanocrystal self-assembly step [17], and pores can be directly viewed and characterized with transmission electron microscopy. The silicon platform also enables the integration into a number of devices and fluidics systems. Previously, pnc-Si membranes have been shown to present little resistance to the diffusion of small molecules [15, 18, 19, 20] and have high permeability to water [16] and air flow [21].

In this work, we show that very small (0.4 mm^2) pnc-Si membranes can generate electroosmotic flows of $10 \text{ }\mu\text{L}/\text{min}$ at voltages of 20 V or lower. However, because the membranes themselves add very little electrical resistance to the system, the transmembrane voltages ($\sim 10 \text{ mV}$) are much smaller than the applied voltage. Thus the intrinsic EOP performance for pnc-Si membranes is $2.6 \times 10^2 \text{ mL min}^{-1} \text{ cm}^{-2} \text{ V}^{-1}$, more than three orders of magnitude higher than all previous EOPs reported in the literature. Our work suggests that nanomembranes such as pnc-Si provide an opportunity for ultralow on-chip pumping in microfluidic systems.

5.3 Results and Discussion

5.3.1 Electroosmosis Flow Rates

Pnc-Si membrane chips with different amounts of freestanding membrane (one, three, six, or nine $200 \times 200 \text{ }\mu\text{m}$ windows) were fabricated as described in Methods (Fig. 5.1a). Characterization by electron microscopy determined that membranes had an average pore size of 19.5 nm and a porosity of 5.7% (Fig. 5.1b). The chips were sealed between two polyethylene terephthalate (PET) chambers with o-rings, and the chambers were filled with 100 mM KCl (Fig. 5.1c). A Hewlett Packard (Palo Alto, CA) E3612A DC power supply was used to apply a constant voltage of 20 V, and the volume of KCl passed into the receiving chamber was measured on a balance at intervals. The supply chamber was continuously replenished, so that pressure gradients between the two chambers were

negligible. While bubbles were generated at the platinum electrodes via electrolysis, the chambers were open to the environment to allow the gases to leave and the electrode position was maintained away from the chamber walls to prevent trapping of bubbles at the membrane. Control experiments with solid silicon chips confirmed that the chambers were well sealed with no leak current. Control experiments using chips with freestanding membranes removed did not exhibit any flow (Fig. 5.2a), indicating that the pores in the material are crucial for electroosmosis.

Representative volume vs. time curves are plotted in Fig. 5.2a for the four different chips with active membrane area. Volumetric electroosmotic flow rates were determined from the slope of these curves. We observe in Fig. 5.2b that the relationship between volumetric flow rate and active area is linear. Because an increase in active area results in a proportional increase in the number of open pores, maximizing the active membrane area occupying a channel cross section will maximize flow rates. Since pnc-Si is manufactured using highly scalable photolithography techniques, the active area can be scaled to match channel dimensions in future applications.

5.3.2 Theoretical Comparison

We compare our experimental results to theory developed by Rice and Whitehead [22]. Volumetric electroosmotic flow, Q , through a narrow capillary in the absence of an external pressure gradient can be described by the following,

$$Q = -\frac{\epsilon\zeta\mathbb{E}A_c}{\mu} \left[1 - \frac{2I_1(\kappa r)}{\kappa r I_0(\kappa r)} \right] \quad (5.3.1)$$

where ϵ is the product of the dielectric constant of the solution and the permittivity of free space, ζ the zeta potential of the capillary walls, \mathbb{E} the electric field through the capillary, A_c the cross sectional area of the capillary, μ the viscosity, r the capillary radius, and I_0 and I_1 modified Bessel functions of the zeroth and first order respectively.

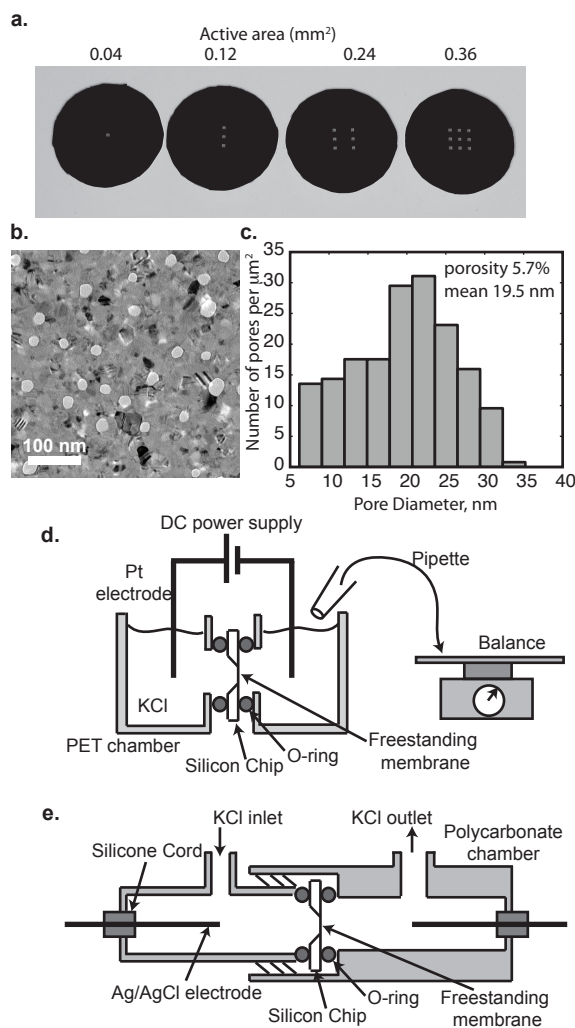


Figure 5.1: Pnc-Si membranes and testing devices. **a.** Pnc-Si chips with one, three, six, or nine $200 \times 200 \mu\text{m}$ windows of freestanding membrane. 15 nm thick pnc-Si membrane extends over each “window” on the silicon chips. **b.** Transmission electron micrograph of pnc-Si membrane. White spots are pores and black regions are diffracting nanocrystals. **c.** Pore diameters as determined by MATLAB image processing of a $1.7 \times 1.1 \mu\text{m}$ TEM image of the membrane depicted in panel b. **d.** Electroosmosis testing device. Pnc-Si chips are sealed between two polyethylene terephthalate (PET) chambers, and a DC power supply maintains a constant voltage across two Pt electrodes. KCl solution that flows into the receiving chamber was continuously removed and weighed at intervals to determine electroosmosis rate. **e.** Streaming potential testing device. Pnc-Si chips are sealed between two threaded polycarbonate chambers. Ag/AgCl electrodes measure voltage difference between cells as KCl is pressurized through chamber.

κ is the reciprocal of the Debye length and is found using

$$\kappa^{-1} = \sqrt{\frac{\epsilon k_b T}{2q^2 c}}. \quad (5.3.2)$$

where k_b is the Boltzmann constant, T the temperature, q the charge of an ion in a symmetrical salt, and c the concentration of the counterion. The multiplier on the right hand side of Eq. (5.3.1) takes into account the reduction in electroosmotic velocity of the region within the diffuse layer at the edge of the pore wall, though if $\kappa^{-1} \ll r$, this term vanishes and the equation reduces to the classical Helmholtz-Smoluchowski description of electroosmosis [23]. In our case, the nanopores within the membrane are similar in dimension to the Debye length and we must consider this scaling factor. As this theory is developed using the Debye-Huckle approximation, it is applicable for zeta potentials of up to 50 mV [22, 8] and EOPs with higher zeta potentials require alternate solutions [2]. As shown below, the magnitude of zeta potential for pnc-Si is less than 30 mV and so the Debye-Huckle approximation is valid.

Volumetric electroosmotic flow through a porous medium can be determined by expanding Eq. (5.3.1) to describe a bundle of capillaries in a manner similar to the use of Darcy's law for pressurized flow [23]. Since we can obtain pore distributions from TEM images of pnc-Si membranes, we can sum Eq. (5.3.11) over all the pores in the image and scale by the ratio of membrane area to image area, A_a/A_{Im} , to obtain the total volumetric flow through a pnc-Si membrane,

$$Q = -\frac{A_a}{A_{Im}} \frac{\epsilon \zeta \mathbb{E}}{\mu} \sum_{i=1}^{\# \text{ of pores}} \pi R_{p_i}^2 \left[1 - \frac{2I_1(\kappa R_{p_i})}{\kappa R_{p_i} I_0(\kappa R_{p_i})} \right], \quad (5.3.3)$$

where R_p is the radius of each particular pore. We calculated the electric field across the pores by assuming current within the short nanopores follows Ohm's law,

$$\mathbb{E} = \frac{I}{A_a \chi k} \quad (5.3.4)$$

where χ is the porosity and k is the conductivity of the solution. The current within the pores was approximated by the measured current across the device, I . Conductivity was measured with a CON6 conductivity meter (Oakton Instruments, Vernon Hills, IL). The results indicate an electric field of 8×10^5 V/m across the membranes. These high electric fields are obtained for relatively low applied voltages because pnc-Si is only 15 nm thick. Because electroosmotic flow rates increase in proportion to the electric field strength, Eq. (5.3.1), high electric fields across the membrane enhance pump performance. The benefit of using thin materials for electroosmosis is further examined in our comparison to other EOPs (below).

The zeta potential of the pore walls was determined from streaming potential measurements. In these experiments, pnc-Si chips were inserted into the polycarbonate streaming potential device in Fig. 5.1e and were sealed by threading the two chambers together and compressing two o-rings. Ag/AgCl electrodes were prepared using the method of Burns and Zydney [24] and sealed into the device with compressible silicone cord. The chamber was filled with 100 mM KCl and pressurized with N₂. For each measurement the pressure was allowed to stabilize for 30s, as displayed by a digital manometer (VWR, West Chester, PA), and the potential difference across the membrane was measured with a TEK DMM252 multimeter (Tektronix, Beaverton, OR).

Reciprocity relations can be used to rearrange Eq. (5.3.1) into an analogous equation for streaming potential that holds for narrow channels with low zeta potentials,

$$\frac{\Phi_s}{\Delta P} = \frac{\epsilon\zeta}{\mu\lambda} \left[1 - \frac{2I_1(\kappa R_p)}{\kappa R_p I_0(\kappa R_p)} \right] \quad (5.3.5)$$

where Φ_s is the streaming potential measured at zero current and ΔP is the applied pressure through the membrane [25]. In Eq. (5.3.5) the pore size, R_p , is taken to be the average pore size. The slope of a streaming potential versus pressure plot can be used to solve Eq. (5.3.5) for the zeta potential (see Methods). By this method we find that the zeta potential of untreated pnc-Si membranes is -13.9 mV.

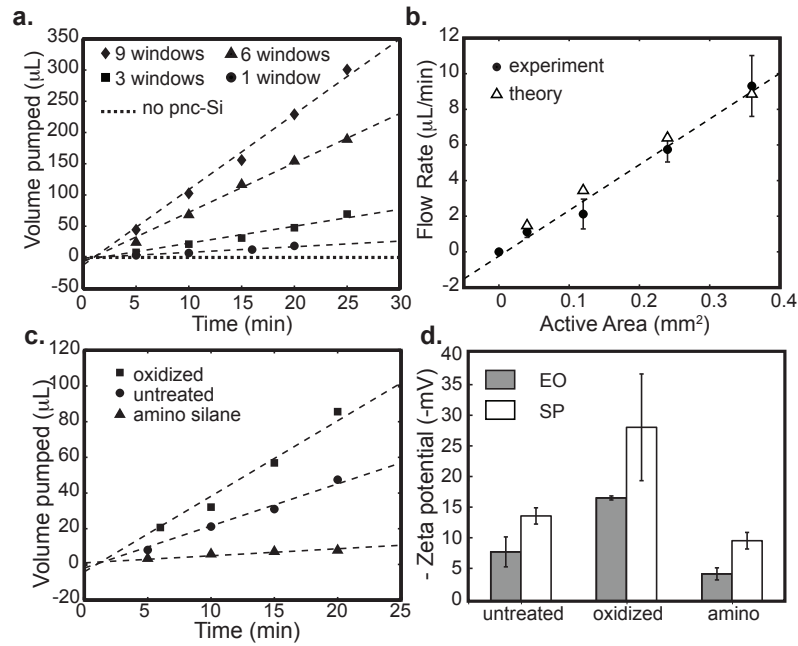


Figure 5.2: Electroosmotic flow. **a.** Electroosmotic transport of KCl measured over time for untreated pnc-Si chips with active areas shown in Fig. 5.1a. All measurements were performed at an applied voltage of 20 V. Dotted line indicates a 9 window chip without pnc-Si material. **b.** Electroosmotic flow rates of untreated pnc-Si membranes as a function of active area at an applied voltage of 20 V. Theoretical points are calculated using the pore characteristics, current, and zeta potential of the particular experimental point. **c.** Electroosmotic transport of modified pnc-Si membranes. Higher flow rates are observed for oxidized membrane. Amino silanization reduces the flow rate, but does not change the direction of the flow. **d.** Zeta potential measured through electroosmotic and streaming potential experiments. As expected, oxidation increases the zeta potential while amino silanization reduces the zeta potential.

Theoretical flow rates for each experiment were calculated using the electric field (Eq. (5.3.4)), average zeta potential (Eq. (5.3.5)), and pore characteristics as obtained from image processing of TEM micrographs. The theoretical flow rates are very similar to the experimental flow rates, indicating that theory developed for infinitely long pores [22, 23] also holds for pore radii that are on the same order as their length. Entrance and exit effects that can, in principle, play a larger part in the electroosmosis through short pores were not observable in our experiments.

5.3.3 Surface modifications

Modifying the surface of a material can change the zeta potential and alter the rate of electroosmotic flow, Eq. (5.3.1). To investigate the ability to affect electroosmosis through surface modifications of pnc-Si, we treated membranes with both plasma oxidation and aminosilanization (Fig. 5.2c). Oxidation increased flow rates by about 2x over the untreated samples, while aminosilanization reduced the flow rates almost to zero.

The effects of plasma oxidation can be understood as an enhancement of the intrinsic negative charge of pnc-Si. Pnc-Si is expected to grow a negatively charged native oxide as silicon surfaces typically do in the presence of oxygen [27]. This expectation is consistent with the negative zeta potential of untreated pnc-Si and the fact that electroosmotic flow is directed toward the negative electrode. Plasma oxidation, a treatment that is commonly used to clean carbonaceous substances off of surfaces [26], has been previously shown to slow the diffusion of negatively charged molecules through pnc-Si membranes [15], indicating a stronger negative charge than untreated membranes. Plasma oxidation also resulted in a higher measured zeta potential (Fig. 5.2d), suggesting that the oxide layer is denser than the native oxide layer on untreated membranes.

The reduction of flow with aminosilanization treatment can be understood as a reduction of the native negative surface charge on pnc-Si. Silanization, a chemical reaction that enables a silicon containing organic compound (or silane) to be covalently bonded to a silica surface, allows for a myriad of functionalization possibilities due to the abundance of silanes. In this study, we have grafted aminopropyltriethoxysilane (APTES) to the surface of the plasma oxidized pnc-Si membranes. This results in a terminal amino group on the surface, which carries a positive charge at neutral pH. The aminosilanization treatment greatly reduced the rate of electroosmosis, but did not change the direction of fluid flow or reverse the sign of the zeta potential measurements (Fig. 5.2c,d). This suggests that the positive amino groups reduced the net surface

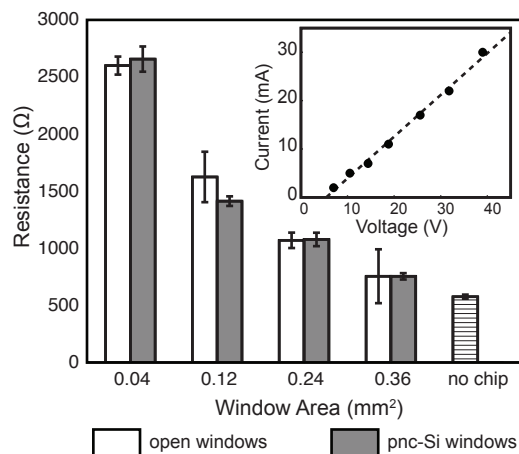


Figure 5.3: Pnc-Si electrical resistance. **a.** Pnc-Si chips with different amounts of active area were used in the experiments. **b.** Resistance of pnc-Si membranes is compared to identical form factor chips with windows lacking freestanding pnc-Si material. Pnc-Si membranes impart negligible resistance to the system. The "no chip" bar indicates the resistance of the system lacking a silicon chip. Inset shows a typical IV curve from a six window (0.24 mm² active area) pnc-Si chip. Error bars are standard deviations.

charge within the pores, but that the modification was not complete enough to neutralize the native negative charge.

Note that in this study we calculated zeta potential from streaming potential, Eq. (5.3.5), and electroosmosis measurements, Eq. (5.3.1). Streaming potential measurements are the most common form of zeta potential calculation, though we include electroosmotic calculations for comparison. pH changes induced by electrolysis at the electrodes and the effects of ion migration through the device can influence the zeta potential as calculated from electroosmosis [29]. We do see an agreement in the trend of the zeta potentials as calculated by the different methods for the treated membranes, though electroosmosis calculations lead to lower zeta potentials for all membrane types.

5.3.4 Comparison to other EOPs

To compare the intrinsic flow rate with those found in the literature, we normalized the electroosmotic flow rates by active area and transmembrane voltage. Note that only a

small portion of the applied voltage, V_{app} , falls across the membrane. One method to determine the transmembrane voltage, V_{TM} , is through a knowledge of the electrical resistances in the system [11, 14],

$$V_{app} = V_{dec} + (2R_b + R_c + R_m)I. \quad (5.3.6)$$

The resistance R_b occurs within the bulk fluid in the chambers, R_c is the resistance of the silicon chip, and R_m is the resistance of the membrane. V_{dec} is the decomposition potential, or the voltage required to initiate electrolysis at the Pt electrodes. The transmembrane voltage is the product of the membrane resistance and current: $V_{TM} = R_m I$. I-V curves (Fig. 5.3 inset) can be used to determine the parameters in Eq. (5.3.6); the slope of an I-V curve of a system with an intact membrane gives $(2R_b + R_c + R_m)$ and the slope of an I-V curve using an equivalent geometry chip in which the membrane was removed gives $(2R_b + R_c)$. Thus the difference in resistances calculated in these two cases is attributed to the membrane itself (R_m).

In Fig. 5.3 we report the resistances as calculated from I-V curves for the different active area chips both with and without membranes. In each case the difference is within the error of the measurement, indicating that the resistance added by the membranes is no greater than $\sim 70 \, \Omega$ and therefore the transmembrane voltage is no greater than 700 mV given experimental currents of 10 mA. However, the actual transmembrane voltage appears to be much smaller than this estimate as the electric field strength (8×10^5 V/m) and a 15 nm thick membrane suggests a transmembrane voltage of 12 mV. Low membrane resistance compared to all other resistances in the system has been seen before in diffusion studies [15, 18, 20, 16]. In these studies, the ultrathin dimension of the membrane results in a transmembrane resistance to diffusion that can be neglected in any practical setting unless the molecules of interest are similar in size to the pores. The low electrical resistance of pnc-Si in electroosmosis experiments also follows from the ultrathin quality of the membrane. The insertion of the 15 nm nanoporous layer

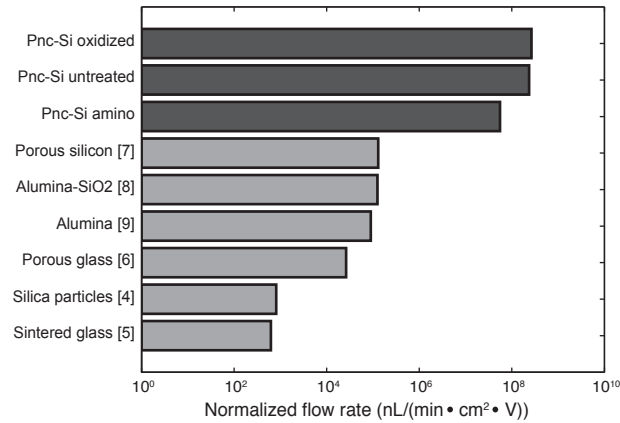


Figure 5.4: Flow rate comparison with other EOPs from the literature.

Flow rates normalized by active area and transmembrane voltage indicate that pnc-Si membranes have innate electroosmosis rates several orders of magnitude higher than other electroosmosis pumps. The other electroosmotic pumps shown here require higher voltages in order to produce flow rates that could reasonably drive microfluidic devices. Thinner materials in this chart exhibit higher flow rates for a given voltage, although the thinnest materials found in the literature are still at least two orders of magnitude thicker than pnc-Si membranes. Additionally, the transmembrane voltage for pnc-Si is lower than for all other EOPs.

is necessary to generate microscale flow, yet does not significantly alter the current or power consumed by the system.

Pnc-Si is more than 100 times thinner than any other membrane material used for electroosmotic pumping. In Fig. 5.4 we examine the efficiency of pumping with pnc-Si compared to other EOPs found in the literature. The efficiency is calculated as a normalized flow rate: the measured flow rate is divided by both the transmembrane voltage and the active membrane area. Pnc-Si membranes produce normalized flow rates several orders of magnitude higher than all other materials. Applied voltages were considered equivalent to the transmembrane voltages for porous silicon [10], alumina [12], porous glass [14], sintered glass [9], and silica particle [8] pumps, because in these EOPs the membrane resistance is the dominant electrical resistance in the system [11]. Even ‘thin’ EOPs exhibit resistances that are orders of magnitude higher than pnc-Si membranes. For example a 60 μm thick alumina membrane [11] has a membrane

resistance of $8000\ \Omega$ compared to $\sim 1.2\ \Omega$ for pnc-Si.

The remarkably high efficiency of pnc-Si as an EOP holds promise for ultralow voltage ($< 100\ \text{mV}$) pumps that can be integrated directly into channels to actuate and drive microfluidics. Our current experimental system, while useful for measuring electroosmosis properties of pnc-Si for the first time, operated at 20V and is far from optimized. To realize the full potential of pnc-Si based pumps, fluidic channel cross sections and active membrane areas will need to be of similar dimensions. Electrode designs also need to be improved. Specifically, the integration of electrodes directly onto membrane chips will significantly reduce the electrical resistance from fluidic channels. The use of Ag/AgCl electrodes allow experiments to be run under the decomposition potential and minimize gas generation [30]. Increasing the surface area of electrodes will also improve electron transfer and increase charge density.

5.4 Conclusions

Ultrathin pnc-Si membranes operate as electroosmotic pumps with a much greater efficiency than any prior membrane material. This is due to the small electrical resistance presented by the membrane and high electric fields across the molecularly thin membrane. The characteristics of electroosmosis through pnc-Si membranes agree with theory developed for membranes with infinitely long pores. Pnc-Si membranes can be readily modified through oxidation and silanization techniques, and we observed subsequent changes in zeta potential and electroosmotic flow rates. Pnc-Si EOPs must be optimized to reduced applied voltages to the estimated transmembrane voltages of $\sim 10\ \text{mV}$. Because of the ease of integration with microfluidic systems, these optimized pnc-Si membranes should enable low voltage, on-chip electroosmotic pumping in microfluidic devices.

5.5 Methods

5.5.1 Pnc-Si Fabrication

The pnc-Si membranes in this study were made on 200 μm $\langle 100 \rangle$ silicon thick wafers using the methods developed in Striemer *et al.* [15]. Photoresists were spin-coated on the surface of the wafers, and chrome masks were used to define the geometry of the 6.5 mm diameter experimental chips and 3 mm diameter imaging chips. The masks also defined the intended internal windows of freestanding pnc-Si membranes (1, 3, 6, or 9 windows of 200 x 200 μm for experimental chips and 4 windows of 100 x 100 μm for imaging chips). A three layer 20nm SiO_2 /15 nm amorphous Si/20 nm SiO_2 stack was sputtered onto patterned wafers via RF magnetron sputtering. The wafers were annealed at 1000°C at a rate of 100°C/s to induce crystallization of the amorphous silicon layer. The bulk patterned silicon was anisotropically etched with ethylene diamine pyrocatechol (EDP), and protective oxide layers were removed with buffered oxide etchant (BOE). Pore distributions were obtained from TEM micrographs using an open source MATLAB (The Mathworks, Natick, MA) image processing program (access: <http://nanomembranes.org/software.html>) (Fig. 5.1c).

5.5.2 Testing Devices

The electroosmosis testing device was built by drilling vertical wells into two pieces of polyethylene terephthalate (PET) (Fig. 5.1d) Access points to the vertical wells were drilled into the side of each PET block each with a recessed ledge to hold an o-ring. Pnc-Si membranes were fit between o-rings at the two access points and the devices was sealed using screws with wing nuts.

The streaming potential device was designed using two cylindrical pieces of polycarbonate. Wells were drilled into the polycarbonate pieces, and the ends were threaded for easy sealing of the pnc-Si membrane chips between two o-rings. The end of each well was terminated with a small opening for the Ag/AgCl electrodes. Each electrode

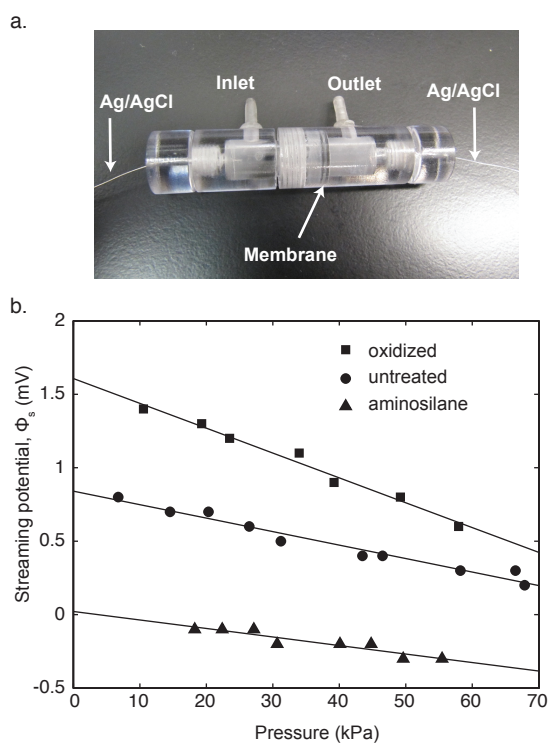


Figure 5.5: Streaming potential measurements. Streaming potential data for unmodified, oxidized, and amino-silanized membranes. The measured streaming potential, Φ_s is plotted against the pressure. The slope of each line can be used to calculate zeta potential using Eq. (5.2.5).

was encased in a small piece of silicone cord, which was sealed against the opening with a small polycarbonate screw. A small polycarbonate port was glued to the top of each well and allowed the attachment of Tygon tubing (3/32" ID). The Tygon tubing was attached to a nitrogen tank and manometer for pressurization of the chamber. In Fig. 5.5b we plot characteristic data of streaming potential vs. pressure for native and modified membranes. The offset in the y-intercept is caused by slight differences in Ag/AgCl wires and chamber assembly. The slope of these curves can be used to determine the zeta potential with Eq. (5.3.5). Note that in solving for the zeta potential we use an average pore radius for R_p . This is because the streaming potential relationship is not additive and cannot be easily determined for a pore distribution.

5.5.3 Plasma Oxidation and Aminosilanization

Pnc-Si chips were oxidized using a Yield Engineering Systems (Livermore, CA) chemical vapor deposition (CVD) system. Pnc-Si chips were placed in the 150°C chamber and a vacuum of 0.3 torr was drawn. A plasma of 190 kV was struck in the chamber with a 20 sccm flow of oxygen for 5 minutes. Finally the chamber was flushed with ultra high purity nitrogen.

Aminosilanization was performed in the CVD system after first cleaning the chips by plasma oxidation using the same procedure as above. One mL of deionized H₂O was injected into the chamber over 3 minutes while the chamber remained at vacuum. Finally, 1 mL of aminopropyltriethoxysilane (Sigma-Aldrich, St. Louis, MO) was injected into the oven over 3 minutes to functionalize the chips. Ellipsometry measurements indicated that the silane layer was 5 Å thick.

5.6 References

- [1] X. Wang, C. Cheng, S. Wang, S. Liu, Electroosmotic pumps and their applications in microfluidic systems, *Microfluid. Nanofluid.* **6** 145-162 (2009).

- [2] S. Yao, J.G. Santiago, Porous glass electroosmotic pumps: theory, *J. Colloid Interf. Sci.* **268** 133-142 (2003).
- [3] L. Jiang, J. Mikkelsen, J.-M. Koo, D. Huber, S. Yao, L. Zhang, P. Zhou, J.G. Maveety, R. Prasher, J.G. Santiago, T.W. Kenny, K.E. Goodson, Closed-loop electroosmotic microchannel cooling system for VLSI circuits, *IEEE T. Compon. Pack. T.* **25** 347-355 (2002).
- [4] N.-C. Tsai, C.-Y. Sue, Review of MEMS-based drug delivery and dosing systems, *Sensor. Actuat. A-Phys.* **134**, 555-564 (2007).
- [5] E.L.P. Uhlig, W.F. Graydon, The electro-osmotic actuation of implantable insulin micropumps, *J. Biomed. Mater. Res.* **17**, 931-943 (1983).
- [6] G. M. Whitesides, The origins and the future of microfluidics, *Nature* **442**, 368-373 (2006).
- [7] P. Yager, T. Edwards, E. Fu, K. Helton, K. Nelson, M.R. Tam, B.H. Weigl, Microfluidic diagnostic technologies for global public health, *Nature* **442**, 412-418 (2006).
- [8] S. Zeng, C.-H. Chen, J. C. Mikkelsen Jr., J.G. Santiago, Fabrication and characterization of electroosmotic pumps, *Sensor. Actuat. B-Chem.* **79**, 107-114 (2001).
- [9] W.-E. Gan, L. Yang, Y.-Z. He, R.-H. Zeng, M.L. Cervera, M. de la Guardia, Mechanism of porous core electroosmotic pump flow injection system and its application to determination of chromium(VI) in waste-water, *Talanta* **51**, 667-675 (2000).
- [10] S. Yao, A.M. Myers, J.D. Posner, K.A. Rose, J.G. Santiago, Electroosmotic pumps fabricated from porous silicon membranes, *J. Microelectromech. Sys.* **15**, 717-728 (2006).
- [11] S.K. Vajandar, D. Xu, D.A. Markov, J.P. Wikswo, W. Hofmeister, D. Li, SiO₂-coated porous anodic alumina membranes for high flow rate electroosmotic pumping, *Nanotechnology* **18**, 275705 (2007).

- [12] Y.-F. Chen, M.-C. Li, Y.-H. Hu, W.-J. Chang, C.-C. Wang, Low-voltage electroosmotic pumping using porous anodic alumina membranes, *Microfluid Nanofluid.* **5**, 235-244 (2008).
- [13] Y. Ai, S.E. Yalcin, D. Gu, O. Baysal, H. Baumgart, S. Qian, A. Beskok, A low-voltage nano-porous electroosmotic pump, *J. Colloid Interf. Sci.* **350**, 465-470 (2010).
- [14] S. Yao, D.E. Hertzog, S. Zeng, J.C. Mikkelsen Jr., J.G. Santiago, Porous glass electroosmotic pumps: design and experiments, *J. Colloid Interface Sci.* **268**, 143-153 (2003).
- [15] C.C. Striemer, T.R. Gaborski, J.L. McGrath, P.M. Fauchet, Charge- and size-based separation of macromolecules using ultrathin silicon membranes, *Nature* **445**, 749-753 (2007).
- [16] T.R. Gaborski, J.L. Snyder, C.C. Striemer, D.Z. Fang, M. Hoffman, P.M. Fauchet, J.L. McGrath, High performance separation of nanoparticles with ultrathin porous nanocrystalline silicon membranes, *ACS Nano* **4**, 6973-6981 (2010).
- [17] D.Z. Fang, C.C. Striemer, T.R. Gaborski, J.L. McGrath and P.M. Fauchet, Methods for controlling the pore properties of ultra-thin nanocrystalline silicon membranes, *J. Phys.: Condens. Matter* **22**, 454134 (2010).
- [18] E. Kim, H. Xiong, C.C. Striemer, D.Z. Fang, P.M. Fauchet, J.L. McGrath, S. Amemiya, A structure-permeability relationship of ultrathin nanoporous silicon membrane: a comparison with the nuclear envelope, *J. Am. Chem. Soc.* **130**, 4230-4231 (2008).
- [19] R. Ishimatsu, J. Kim, P. Jing, C.C. Striemer, D.Z. Fang, P.M. Fauchet, J.L. McGrath, S. Amemiya, Ion-selective permeability of an ultrathin nanopore silicon membrane as probed by scanning electrochemical microscopy using micropipet-supported ITIES tips, *Anal. Chem.* **82**, 7127-7134 (2010).

- [20] J.L. Snyder, A. Clark Jr, D.Z. Fang, T.R. Gaborski, C.C. Striemer, P.M. Fauchet, J.L. McGrath, An experimental and theoretical analysis of molecular separations by diffusion through ultrathin nanoporous membranes, *J. Mem. Sci.* **369**, 119-129 (2010).
- [21] M.N. Kavalenka, C.C. Striemer, D.Z. Fang, K. Shome, T.R. Gaborski, J.L. McGrath, P.M. Fauchet, Ballistic and non-ballistic gas flow through ultrathin nanopores, *Phys. Rev. Lett.* In Review.
- [22] C.L. Rice, R. Whitehead, Electrokinetic flow in a narrow cylindrical capillary, *J. phys. Chem.* **69**, 4017-4024 (1965).
- [23] R.F. Probstein, *Physicochemical Hydrodynamics* (Wiley, Hoboken, NJ, ed. 2, 2003) pp. 165-236.
- [24] D.B. Burns, A.L. Zydney, Buffer effects on the zeta potential of ultrafiltration membranes, *J. Mem. Sci.* **172**, 39-48 (2000).
- [25] A. Mansouri, C. Scheuerman, S. Bhattacharjee, D.Y. Kwok, L.W. Kostiuk, Transient streaming potential in a finite length microchannel, *J. Colloid Interf. Sci.* **292**, 567-580 (2005).
- [26] H. Seo, S.B. Kim, J. Song, Y. Kim, H. Soh, Y.C. Kim, H. Jeon, Low temperature remote plasma cleaning of the fluorocarbon and polymerized residues formed during contact hole dry etching, *J. Vac. Sci. Technol. B.* **20**, 1548-1555 (2002).
- [27] H. Ikeda, Y. Nakagawa, M. Toshima, S. Furuta, S. Zaima, Y. Yasuda, Initial oxidation of H-terminated Si(111) surfaces studied by HREELS, *Appl. Surf. Sci.* **117/118**, 109-113 (1997).
- [28] B.J. Kirby, E.F. Hasselbrink Jr, Zeta potential of microfluidic substrates: 1. Theory, experimental techniques, and effects on separations, *Electrophoresis* **25**, 187-202 (2004).

-
- [29] K.J. Kim, A.G. Fane, M. Nystrom, A. Pihlajamaki, W.R. Bowen, H. Mukhtar, Evaluation of electroosmosis and streaming potential for measurement of electric charges of polymeric membranes, *J. Mem. Sci.* **116**, 149-159 (1996).
- [30] K.A. Dunphy Guzmán, R.N. Karnik, J.S. Newman, A. Majumdar, Spatially controlled microfluidics using low-voltage electrokinetics, *J. MEMS* **15**, 273-245 (2006).

Chapter 6

Concluding Remarks

Porous nanocrystalline silicon membranes are an enabling technology because of their unique nanometer scale thickness. Diffusion and pressurized separations occur quickly and with high resolution, and the electrostatic interactions between diffusing species and the negatively charged membranes can be readily assayed. Pnc-Si membranes have higher permeability and rates of electroosmosis than those achieved with conventional membranes. As direct visualization of pore distributions is possible using transmission electron microscopy, experiments and theory can be easily coupled for the 15 nm thick membrane. This work on the characterization of pnc-Si membranes in several applications will allow further device development and the study of pnc-Si membranes for more advanced applications, including hemodialysis, cell culture, and membrane chromatography.

6.1 Diffusion separations and sieving model

6.1.1 Summary of findings

The 1-D and 3-D sieving models were developed to analyze the diffusion of differently sized molecules through ultrathin membranes. The resistance to diffusion imparted by the membrane is calculated directly from pnc-Si pore distributions and can be attributed

to two processes: the parallel diffusion across the membrane surface to find a pore (pore discovery) and the transmembrane diffusion through the pores. It was found that the pore discovery component of the resistance is negligible for conventional thick membranes compared to the transmembrane resistance, but that it is an important factor in the diffusion of small molecules through an ultrathin membrane.

The 1-D analytic model was used to examine the contributions of thickness, porosity, pore size, experimental duration, and size of fluid wells to the quality of the separations. In micron thick membranes, the calculated resistance occurs over a longer distance and thus slows diffusion to a greater extent compared to ultrathin membranes. Lower porosity decreases the diffusion permeability and increases the hindrance for all molecule sizes. The largest pores in the distribution were found to define the cutoff, and the addition of small pores did not significantly alter separation characteristics. Shorter experimental durations led to a magnification of small hindrance differences between similarly sized molecules, while at long time scales these differences were blurred by diffusion within the bulk fluid wells. Systems with small fluid wells were found to reach equilibrium faster; however, the separations were more sensitive to the membrane resistance as the membrane represented a larger fraction of the entire system.

The 3-D computational model allowed for direct comparison with experimental results. The ease of measuring pnc-Si pore distributions from TEM micrographs aided in the development of these comparisons. The simulations matched experimental results for molecules smaller than the physical pore cutoff, and these small molecules appeared to diffuse by free diffusion as if no barrier existed. Larger molecules deviated from the predictions, which may have been a result of protein adsorption to the pore walls. A simulated reduction of pore sizes by 5 nm reduced the cutoff to smaller molecule sizes and better matched the 24 and 48 hour experiments.

6.1.2 Future direction

The research on diffusion modeling is far from complete, and there are a few particularly important experimental and theoretical avenues to be tested. While the effect of thick membranes was discussed in the 1-D analytical model, no comparisons between experimental and theoretical separations for thick membranes were performed. An ideal membrane for such a study would be a polycarbonate track etched membrane, which is several microns thick and has well defined cylindrical pores. Certain membrane modifications, such as PEGylation, can reduce the contribution of adsorption, and may provide for a better comparison between experimental and theoretical results as long as alterations to pore size can be quantified. Carbonization is a method used to reduce the size of pnc-Si pores that can be visualized in TEM and may provide an experimental series of membranes with decreasing pore distribution to compare with 3-D diffusion models [1]. The contribution of parallel diffusion can be assayed by performing experiments with low pore densities. The validity of the resistance calculations can be tested by using scanning electrochemical microscopy to determine the diffusion of large molecules [2, 3]. Finally, theoretical treatments for non-spherical species can be developed by using experimental separations of rigid cylindrical DNA oligomers [4].

6.2 Charge-based separations and electrostatics model

6.2.1 Summary of findings

Diffusion separations with pnc-Si membranes do not function solely based on size selection, as electrostatic interactions between the membrane and the diffusing species can allow for charge-based separations. When salt concentrations are reduced, the ionic shielding of the electric potential is also reduced, increasing the electrostatic interactions between the membrane and diffusing species. If both membrane and diffusing species are of like charge, the membrane will impart additional hindrance due to repulsive interactions in low salt concentration separations.

In this work, negatively charged proteins and DNA oligomers were shown to have substantially different separations at high and low ionic concentrations for membranes with the same pore distributions. The rigid DNA oligomers were also able to pass through pores with diameters less than their long dimension at high ionic concentrations, indicating that the sieving of DNA is based on a combination of short and long dimensions. Negatively charged nanoparticles exhibited different degrees of separation at high and low salt concentrations. Neutral nanoparticles had similar separations at high and low salt concentrations, which indicated that the membrane did not offer additional electrostatic hindrance in this case. Electrostatic contributions were added to the previously discussed sieving model, and agreement was found between model and nanoparticle separations.

6.2.2 Future direction

Both experimental separations and the electrostatic sieving model can be improved by further work. Positively charged proteins and nanoparticles were not assayed in this study, though adsorption mediated by electrostatic interactions must be considered in this case. The charge of pnc-Si membranes can be altered by surface modification techniques [1, 5], and the charge on a particular protein can be reduced through selective acetylation of lysine groups [6]. Peptide nucleic acid (PNA) is similar in structure to DNA but is uncharged and may provide an interesting comparison. Finally, the question of entrance and exit effects is unanswered by this research, and probing the pore openings using electrostatic force microscopy may provide some information[7].

6.3 Water permeability and pressurized separations

6.3.1 Summary of findings

The low fluid resistance imparted by ultrathin pnc-Si membranes has allowed for high water permeability compared to other nanoporous membranes. The permeability sur-

passes that of carbon nanotube membranes, whose hydrophobic physical characteristics allow for slipping flow rather than traditional parabolic flow. Fluid flow through pnc-Si membranes has been compared to the Dagan equation, which considers entrance and exit effects in a short pore and reduces to the parabolic Hagan-Poiseuille equation for long pores. Pnc-Si membranes were also shown to be capable of sharp separations with nanoparticles and proteins when pressurized. Gold nanoparticles were separated to within 5 nm precision, and different pore distributions provided different cutoffs. A complex mixture of proteins was separated with a cutoff between two proteins that differed by ~ 2 nm in diameter.

6.3.2 Future direction

The future direction of this project encompasses materials testing and further separation experimentation. The effects of the carbonization of pnc-Si and permeability enhancement has been looked at by Fang *et al.* [1]. However, the impact on permeability by additional surface modifications such as aminosilanization and PEGylation remains to be tested. The effects of pore cutoff on protein separations has not yet been fully studied for pressurized separations, and the testing of adsorption and formation of cake layers is especially important to protein separations. Alternative separation modalities have been studied by the membrane community in the interest of reducing fouling, and modes such as tangential filtration, where the fluid flows parallel to the membrane surface [8], should be assayed pnc-Si. Charge effects were not noticeable in the pressurized separations of gold in diH_2O ; however, residual charge effects may be observable for low pressures and flow rates.

The development of a pressurized sieving model, while difficult, may be of interest for comparisons with experiments and the prediction of separation characteristics. Hindrance equations equivalent to those used in the diffusion sieving model exist for pressurized separations and can be implemented in a 3-D model [9]. While there are many difficulties in describing a pressurized system, including the formation of cake

layers, concentration polarization, adsorption, and charge effects, information may be able to be gleaned from a simple pressurized hindrance model.

6.4 Pnc-Si membranes as electroosmotic pumps

6.4.1 Summary of findings

Electroosmosis pumps are considered an attractive alternative to mechanical pumps for microfluidic devices and electronic cooling circuits because of their simple electronic actuation, pulse free flows, and lack of moving parts. In this research, pnc-Si membranes exhibited higher intrinsic rates of electroosmotic flow than any of the electroosmotic pumps (EOPs) being developed in the literature. The thinning of conventional EOP materials has allowed for electroosmosis at lower voltages due to the higher electric fields obtained over smaller thicknesses; however, 15 nm thick pnc-Si membranes have normalized electroosmosis rates at least 2 orders of magnitude higher for similar applied voltages. The electric resistance of pnc-Si membranes is negligible compared to the rest of the device, and while 20 V is applied to the device, calculations indicate that only ~ 10 mV across the membrane is driving the electroosmosis. The low voltage electroosmosis of pnc-Si membranes may allow for enhanced portability and ease of use of microfluidic devices.

6.4.2 Future direction

While this work has shown the potential of pnc-Si membranes as a low voltage EOP, much work remains before pnc-Si membranes serve as on-chip EOPs. The running voltage is calculated to be as low as ~ 10 mV; however, this lower limit must be tested. The current experimental system can not be run below the decomposition potential of water, or approximately 4.5 V in our system. This is because of the use of platinum electrodes and the necessity of electrolysis for the establishment of a current in the device. Ag/AgCl electrodes have a lower overpotential, and preliminary experiments

not reported in this thesis have resulted in electroosmosis flow at 1 V and indicate that voltages as low as ~ 80 mV can be obtained with this system. The bulk resistance in the system can be further reduced by placing the electrodes closer to the pnc-Si membrane by using metal deposition or painting of metallic inks, which may allow the lower voltage limit to be achieved.

Several additional tests will help with the validation of pnc-Si EOPs. While pnc-Si membranes exhibit high electroosmotic flow rates in open systems, the use of pnc-Si in a microfluidic device will require pumping against a back pressure. A quantitative study of back pressures and pumping efficiency is necessary before the implementation of pnc-Si as an EOP. In certain cases, fluid flow in a chamber may need to be stirred or moved back and forth, therefore reversible actuation is another needed test. Flow rates in various buffers (i.e. phosphate buffered saline) and salt solutions should be tested to define optimal solutions for biological samples. While only aminosilanization was tested in this work, there exists a plethora of silane ligands that could be used to modify the membrane, and the use of a negatively charged silane ligand would complement our oxidation and aminosilanization results. There exists evidence of Joule heating in our system, although the degree of temperature increase has not yet been rigorously tested. Finally the development of an on-chip pnc-Si EOP may result in several engineering challenges, including determining optimal pump placement within the device, designing a strategy for filling the device with fluid, and the avoidance of air bubbles.

There is still room for theoretical analysis of electroosmosis through pnc-Si membranes. In this work, it was mentioned that theory had been developed for long pore materials [10]. While theory does match experimental results well, entrance and exit effects may exist for ultrathin pnc-Si membranes. Testing these effects may be possible with the use of scanning electrochemical microscopy, in which the profile of ions moving through the pores may be visualized [2, 3]. Pnc-Si membranes with different thicknesses may also aid in this study. Finally, the effects of Debye length may be better observed with smaller pore distributions and lower ionic concentrations [11].

6.5 References

- [1] D.Z. Fang, C.C. Striemer, T.R. Gaborski, J.L. McGrath, P.M. Fauchet, Pore size control of ultrathin silicon membranes by rapid thermal carbonization, *Nano Lett.* **10**, 3904-3908 (2010).
- [2] E. Kim, H. Xiong, C.C. Striemer, D.Z. Fang, P.M. Fauchet, J.L. McGrath, S. Amemiya, A structure-permeability relationship of ultrathin nanoporous silicon membrane: a comparison with the nuclear envelope, *J. Am. Chem. Soc.* **130**, 4230-4231 (2008).
- [3] R. Ishimatsu, J. Kim, P. Jing, C.C. Striemer, D.Z. Fang, P.M. Fauchet, J.L. McGrath, S. Amemiya, Ion-selective permeability of an ultrathin nanopore silicon membrane as probed by scanning electrochemical microscopy using micropipet-supported ITIES tips, *Anal. Chem.* **82**, 7127-7134 (2010).
- [4] J. Happel, H. Brenner, *Low Reynolds Number Hydrodynamics* (Prentice-Hall, Englewood Cliffs, NJ, 1965) pp. 331-346.
- [5] C.C. Striemer, T.R. Gaborski, J.L. McGrath, P.M. Fauchet, Charge- and size-based separation of macromolecules using ultrathin silicon membranes, *Nature* **445**, 749-753 (2007).
- [6] M.K. Menon, A.L. Zydney, Protein charge ladders: a new technique for studying electrostatic interactions in ultrafiltration systems, *J. Mem. Sci.* **181**, 179-184 (2001).
- [7] Y. Sugawara, T. Uchihashi, M. Abe, S. Morita, True atomic resolution imaging of surface structure and surface charge on the GaAs(110), *Appl. Surf. Sci.* **140**, 371-375 (1999).
- [8] R. van Reis, S. Gadam, L.N. Frautschy, S. Orlando, E.M. Goodrich, S. Saksena, R. Kuriyel, C.M. Simpson, S. Pearl, A.L. Zydney, High performance tangential flow filtration, *Biotech. Bioeng.* **56**, 71-82 (1997).

-
- [9] P. Dechadilok, W. Deen, Hindrance factors for diffusion and convection in pores, *Ind. Eng. Chem. Res.* **45**, 6953-6959 (2006).
- [10] R.F. Probstein, *Physicochemical Hydrodynamics* (Wiley, Hoboken, NJ, ed. 2, 2003) pp. 165-236.
- [11] C.L. Rice, R. Whitehead, Electrokinetic flow in a narrow cylindrical capillary, *J. phys. Chem.* **69**, 4017-4024 (1965).